D0 Note 3418

Centro de Investigación y de Estudios Avanzados
del I.P.N.

Measurement of the longitudinal momentum distribution of $p\bar{p} \to Z \to e^+e^-$ events with the DØ Detector

DISSERTATION

Submitted to the Physics Department
in partial fulfillment of the requirements
for the Degree of

Doctor of Philosophy

in

Physics

by

Leonel Magaña Mendoza

Mexico City, MEXICO
October 1997

Centro de Investigación y de Estudios Avanzados
del I.P.N.

Medición de la distribución de momento longitudinal en eventos $p\bar{p} \to Z \to e^+e^-$ con el Detector DØ

TESIS

que presenta

Leonel Magaña Mendoza

para la obtención del grado de

DOCTOR EN CIENCIAS

en la especialidad de

Física

México D.F., México
Octubre de 1997

Esta tesis fue realizada con el apoyo económico del Consejo Nacional de Ciencia y Tecnología (CONACyT), del Centro de Investigación y de Estudios Avanzados del I.P.N. (CINVESTAV) y del Fermi National Accelerator Laboratory (FERMILAB).

Tus manos son mi caricia
mis acordes cotidianos
te quiero por que tus manos
trabajan por la justicia

> *si te quiero es por que sos*
> *mi amor mi cómplice y todo*
> *y en la calle codo a codo*
> *somos mucho mas que dos*

Mario Benedetti, *Inventario*

To Eréndira.

Resumen

La medición de la distribución de momento longitudinal en eventos $p\bar{p} \to Z \to e^+e^-$ constituye una prueba para las parametrizaciones de las funciones de distribución partónica, al mismo tiempo que proporciona un nuevo conjunto de datos que pueden ser empleados como parametros de entrada en los ajustes globales encaminados a mejorar dichas parametrizaciones.

En la presente tesis se describe la medición de la distribución de momento longitudinal en eventos $p\bar{p} \to Z \to e^+e^-$ con el Detector DØ.

La muestra de datos, con una luminosidad integrada de 97.18 ($\pm$ 5.3%) pb^{-1}, fue colectada durante la corrida 1b del Tevatron, después de aplicar cortes de selección estándar de calidad para electrones, la muestra final contiene 6635 eventos $Z \to e^+e^-$.

Para poder estimar la magnitud de las correcciones que habrán de aplicarse a los datos, es necesario contar con una simulación confiable, tanto de los procesos físicos involucrados en el estudio, còmo de los efectos del detector sobre los observables a medir. En la tesis se incluye una descripción detallada de la simulación Monte Carlo empleada en el análisis.

En la tesis también se describe el método empleado para medir el ruido (*background*) que contamina la muestra de datos, para dicha medición se emplean tres muestras de eventos con características similares a las de los eventos de background y se estima la forma de la distribución de dichos eventos en función de los observables x_Z, x_1 y x_2. La principal fuente de background son eventos de uno o dos jets (hadrónicos) que debido a fluctuaciones son vistos por el detector como objetos con características electromagnéticas. La muestra contiene 3.78 ± 0.19 % de background para eventos en que ambos electrones están en la región central del detector, 7.44 ± 0.39 % cuando un electrón está en la región central y el otro en un extremo del detector y 5.47 ± 0.37 % cuando ambos electrones están en los extremos del detector. La forma del background en función de los observables se calcula como el promedio de la forma de la distribución para las tres muestras empleadas en el cálculo del background. Existen otras fuentes de background como la producción de eventos por el mecanismo de Drell Yan y el decaimiento $Z \to \tau\tau$ en el que ambos taus decaen posteriormente a electrones, el primero es medido y tomado en cuenta para las correcciones, aunque su efecto es muy pequeño y el segunto no es considerado.

A continuación se estudian los efectos que la resolución del detector tiene sobre la

medición. La resolución es calculada analiticamente y comparada con la resolución medida directamente de la muestra de datos y con muestras de Monte Carlo. Las resoluciones obtenidas por los tres métodos concuerdan dentro de los errores. Para estudiar posibles sesgos introducidos por la resolución del detector, se compararon muestras de Monte Carlo antes y después de la simulación del detector. Ajustando una recta a la diferencia normalizada de las dos distribuciones se evaluó la magnitud del sesgo resultando ser despreciable. Para estimar el efecto de la resolución de energía del calorímetro se generaron varias muestras de Monte Carlo con diferentes resoluciones de energía encontrándose que el efecto de estas variaciones no es apreciable en las distribuciones de los observables x_Z, x_1 y x_2.

La eficiencia del proceso de selección de la muestra es un parámetro importante para introducir en las correcciones a los datos, dado que la eficiencia es diferente en las distintas partes del detector. Las eficiencias son definidas como el cociente entre el número de eventos que pasan un corte estricto y el número de eventos que no pasaron ese corte. La eficiencia total medida para eventos $Z \rightarrow e^+e^-$ fue de 77.71 $\pm$ 1.41 % para eventos en los que ambos electrones están en la parte central del detector, 73.23 $\pm$ 1.18 % para eventos en los que un electrón está en la parte central y el otro en el extremo del detector 68.05 $\pm$ 1.37 % y 68 $\pm$ 1.37 % cuando ambos electrones están en el extremo del detector.

Además de las correcciones ya mencionadas, se estudiaron otras fuentes de error sistemático en la medición como son la posición del centro de la distribución del vértice de interacción y la eficiencia del detector de trazas. Ambos errores sistemáticos son incluidos en la corrección final a las distribuciones de x.

Finalmente, se presentan las distribuciones de x medidas con las correcciones incluidas y las distribuciones son comparadas con predicciones teóricas.

Acknowledgements

Many people deserve recognition for guiding me through the long, and not always easy or pleasant journey of graduate school. I am grateful to all the people who took time to listen to my questions, correct my misconceptions and provide me with suggestions during these years. An apology to those who are not named in these paragraphs.

Thanks go to all the people who keep Fermilab working and to the members of the DØ Collaboration: designing, and running a particle physics experiment requires the effort of hundreds of talented people. I am very grateful to H. Eugene Fisk for his support.

I thank my advisor Heriberto Castilla from CINVESTAV for accepting me as his graduate student. I am very much indebted to Marcel Demarteau and Sandor Feher, their expertise and patience taught me more than what I was able to learn at a time.

It has been a pleasure to work with the people of the Electroweak Physics Group at DØ; special thanks to Harry Melanson and Darien Wood for their valuable criticism to my work, Joey Thompson for his friendly advice along these years and Jamal Tarazi for kindly helping me even when he was busy finishing his own thesis. Thanks also to the Mexican crew from CINVESTAV at DØ: José Luis González, Raul Hernández and Alberto Sánchez.

I am very grateful to Miguel Angel Pérez who has been a protective patron keeping funding from CINVESTAV reaching graduate students at Fermilab, helping us to shape the future of our careers and encouraging and supporting us to present our results in several meetings during these years.

I can not finish without a word of acknowledgement to the friends who made my life more enjoyable and with whom I shared really good times. Rubén Flores for his friendship and valuable help with the unavoidable bureaucracy. It was always a pleasure to put aside the work and bike along the prairie path with Rafael Gómez while discussing the miseries of life. Gene Alvarez, being a Newyorker provided me with a closer look to the American Culture. Besides biking, I relaxed listening to Blues in several Chicago locations, Thomas Speer was good company during those sessions. Thanks to Ching-Yuk Paul Ngan with whom I had very interesting discussions. Also thanks to the latin crowd: Gervasio Gómez, Rocio Vilar, David Olaya and Rosa, and Miguel Mostafa and Clarisa; it was always interesting to discuss about who spoke the best Spanish amid other cultural issues.

Contents

List of tables

List of figures

Chapter 1

Introduction

By convention there is color,
by convention sweetness,
by convention bitterness,
but in reality there are atoms and space.

Democritus (400 BC) [1]

1.1 Physics motivation

The study of the properties of the intermediate vector bosons allows for precision tests of the standard model of electroweak and strong interactions, for instance, a direct measurement of the mass of the W boson, together with a measurement of the top quark mass constrain the Higgs boson mass.

The longitudinal momentum distribution of the intermediate vector bosons are expected to directly reflect the structure functions of the incoming annihilating partons, since the intermediate vector bosons' fractional longitudinal momentum x_V is equal to the difference between the fractional momenta x_q and $x_{\bar{q}}$ of the two annihilating partons.

There has been only one previous attempt to measure the Z fractional longitudinal momentum by UA1 [1], but due to low energy and statistics they were not sensitive to differences among the various sets of parton distributions available at that time.

A precision measurement of the Z fractional longitudinal momentum x_Z, at higher energy and with larger statistics would make possible further discrimination between sets of modern parton distribution functions, (as it is the case with W asymmetry and Drell Yan production data [2]), as well as further improvement of the global fittings to adjust the parton distribution functions to make theory and experiment agree over a wider range of processes.

[1] Taken from `http://pdg.lbl.gov/cpep/intro_atom.html`

1.2 The theory behind the analysis

The last five decades have witnessed tremendous advances in elementary particle physics, both theoretically and experimentally. The publication of the papers by Glashow, Salam and Weinberg in the sixties [3, 4, 5] set the origin of the theoretical framework known as "Standard Model", which describes all known experimental facts in particle physics.

A comprehensive presentation of the Standard Model is beyond the scope of this thesis; there are many standard text books that present the material [6, 7] at a basic level. However, since this analysis concerns the hadronic production and decay of the Z boson a brief review of the mechanisms of production and decay of the Z boson are presented below, as well as a presentation of parton distribution functions.

1.2.1 Overview of the Standard Model

One of the most successful theories in physics is the Standard Model of strong and electroweak interactions. The Standard Model is a gauge theory based on the group $SU(3)_C \otimes SU(2)_L \otimes U(1)_Y$, which describes the strong, weak and electromagnetic interactions. $SU(3)_C$ is the symmetry group of the strong interactions, and $SU(2)_L \otimes U(1)_Y$ is the symmetry group describing the weak and electromagnetic interactions.

Quarks

	I		II		III
Up **u**	$2/3^a$ R G B[b] $2 \sim 8 \times 10^{-4}$[c]	Charm **c**	2/3 R G B $1 \sim 1.6$	Top **t**	2/3 R G B $173.3 \pm 5.6 \pm 6.2$[d]
Down **d**	-1/3 R G B $5 \sim 15 \times 10^{-3}$	Strange **d**	-1/3 R G B $1 \sim 3 \times 10^{-2}$	Bottom **b**	-1/3 R G B $4.1 \sim 4.5$

Table 1.1: Standard Model Quarks and their properties. The numbers in the right hand side inside the box are the electric charge, the color charge and the mass.

[a] Electric charge is given in terms of the proton charge.

[b] RGB stands for red, green and blue.

[c] Mass is given in GeV/c^2. Mass values from reference [8]. Refer to this article for explanation on the interpretation of the quoted masses.

[d] Measured by DØ [9]. The first error is statistical and the second is systematical.

Leptons

I	II	III
Electron -1 **e** 5.1×10^{-4}	Muon -1 μ 1.05×10^{-2}	Tau -1 τ 1.78
Electron Neutrino -1 ν_{e} $< 7 \times 10^{-6}$	Muon Neutrino -1 ν_{μ} $< 2.7 \times 10^{-4}$	Tau Neutrino -1 ν_{τ} $< 3.1 \times 10^{-2}$

Table 1.2: Standard Model leptons and their properties. The numbers in the right hand side inside the box for each lepton are the electric charge, the color charge and the mass.

The fermionic-matter content of the Standard Model is given by the known quarks and leptons, which are organized in a 3-fold family structure. These three fermionic families have the same properties (gauge interactions) and only differ in their masses. Tables 1.1 and 1.2 summarize the minimal spectrum of fermionic particles of the standard model and some of its basic properties.

Quarks and leptons interact by exchanging gauge bosons: eight massless gluons couple to the color $SU(3)_C$ charge of the quarks and mediate strong interactions, while the $W^{\pm}$, Z and γ of the $SU(2)_L \otimes U(1)_Y$ sector are responsible for weak and electromagnetic interactions. If $SU(2)_L \otimes U(1)_Y$ were an exact symmetry, all fermion and

Gauge Bosons

	Force	Mass	Electric Charge	Spin	Color Charge
Gluons	Strong	0	0	1	R G B
W^+	Weak	80.22	1	1	Color Neutral
W^-		80.22	-1	1	
Z		91.19	0	1	
Photon	Electro-magnetic	0	0	1	Color Neutral

Table 1.3: Gauge bosons of the Standard Model and their properties.

gauge boson masses would be zero. However, a Higgs isodoublet breaks the symmetry down to $U(1)_{\rm em}$ and provides particles with their masses. Fermion masses are essentially free parameters determined by experiments. The $W^\pm$ and Z masses are related to the gauge couplings and thereby interconnected. The precise measurements of m_Z and m_W at CERN and Fermilab constitute one of the most important confirmations of the standard model. Table 1.3 summarizes the gauge bosons of the standard model and some of its basic properties.

1.2.2 Z boson production and decay

The production mechanism for the weak gauge bosons in $p\bar{p}$ collisions is the weak Drell Yan process, where a quark and antiquark annihilate to form a Z boson which later decays. Due to the large transverse momentum transfer of the process, the partons within the colliding particles are essentially free, so the spectator model can be used, in which the partons not directly involved in the Z production are ignored.

1.2.2.1 Z boson production: $p\bar{p} \to Z + X$

The subprocess cross section for Z boson production is given by [7]:

$$\hat{\sigma}(q\bar{q} \to Z) = \frac{\pi G_F}{\sqrt{2}}(1 - 4|Q_q|\sin^2\theta_W + 8Q_q^2\sin^4\theta_W)M_Z^2\delta(\hat{s} - M_Z^2) \tag{1.1}$$

where $Q_q = 2/3$ for u-type quarks and $Q_q = -1/3$ for down-type quarks.

Particles can be considered as made up of two kinds of quarks: the valence quarks (uud in the case of the proton) and the sea quarks, which are $q\bar{q}$ pairs that are part of the color field holding the valence quarks together. The invariant mass of the subprocess is determined by the Z boson mass:

$$\hat{s} = (x_1p_1 + x_2p_2)^2 = x_1x_2s \equiv M_Z^2 \approx 91\text{GeV}^2 \tag{1.2}$$

where p_1, p_2 are the proton and antiproton momenta, respectively and x_1, x_2 are the corresponding momentum fractions. At the Tevatron's center of mass energy $\sqrt{s} =$ 1800 GeV, the typical momentum fraction of the partons involved in the Z production is $x = 0.05$.

Incorporating the parton distribution functions, the total production cross section can be written as:

$$\begin{aligned}\sigma(p\bar{p} \to Z + X) &= \frac{K_Z(\alpha_s)}{3}\int_0^1 dx_1 \int_0^1 dx_2 \\ &\quad \sum_q \left[q_1(x_1, M_Z^2)\bar{q}_2(x_2, M_Z^2) + (q \leftrightarrow \bar{q})\right]\hat{\sigma}(q\bar{q} \to Z)\end{aligned} \tag{1.3}$$

The production subprocesses are illustrated in Figure 1.1, which shows the lowest and next to leading order Feynman diagrams for the Z boson production. At the

Tevatron energies, approximately 80% of the Z bosons are produced from valence-sea interactions [10]. At the Tevatron energy $\sqrt{s} = 1.8$ TeV, the theoretical predicted value for the total cross section $\sigma(p\bar{p} \to Z + X)$ is 6.71 ± 0.3 nb [11, p. 142].

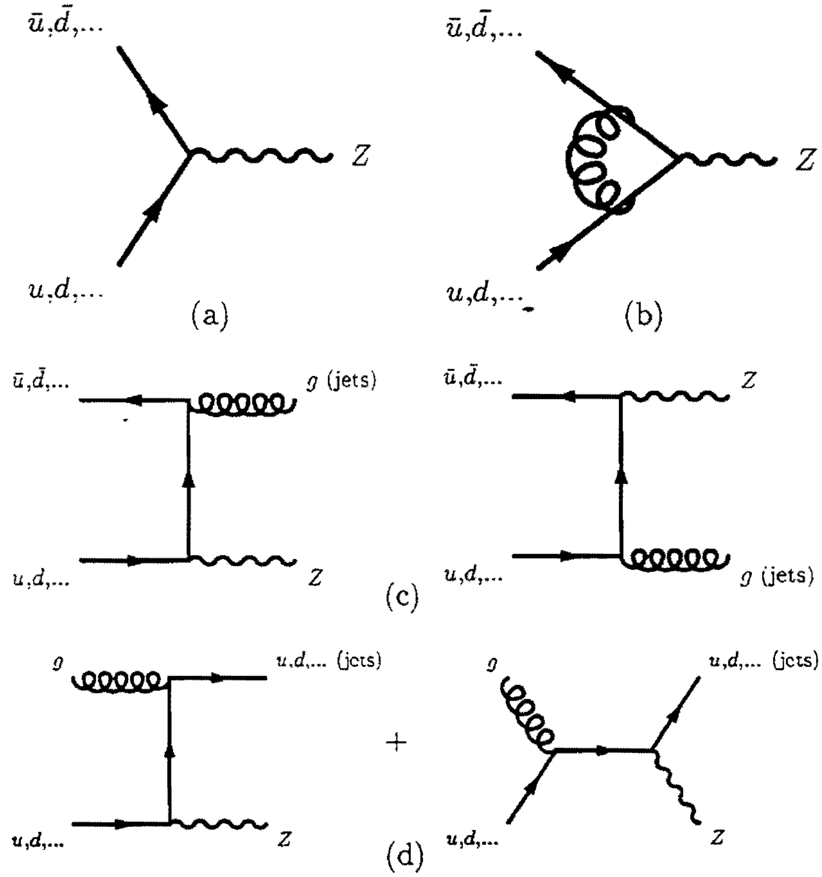

Figure 1.1: Z boson production Feynman diagrams at leading order and next to leading order: (a) Drell-Yan, (b) QCD virtual correction, (c) QCD annihilation process with gluon radiation and (d) QCD Compton process.

1.2.2.2 Z boson decay: $Z \to e^+e^-$

Although the Z boson decays 69.90 ± 0.15 % of the time to hadrons [8, p. 1357], the $Z \to e^+e^-$ decay will be used to identify the Z boson as it was done at the discovery of the Z boson by the UA1 Collaboration [12], the reason for using this decay is that there are several other processes that produced the same final state, which makes more difficult to extract the background from the sample. Besides, the signal from the leptonic decay has a very well defined signature from which the background is easily separated.

The Feynman diagrams of the $Z \rightarrow e^+e^-$ decay are shown in figure 1.2.

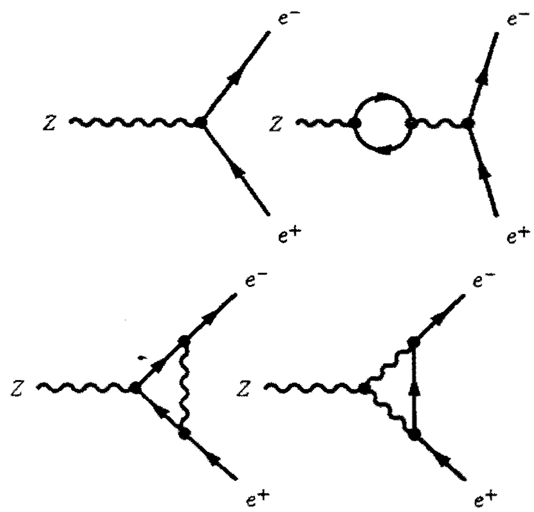

Figure 1.2: Z boson decay to e^+e^- Feynman diagram.

The electronic branching ratio of the Z boson is calculated as follows:

$$Br(Z \rightarrow e^+e^-) = \frac{\Gamma(Z \rightarrow e^+e^-)}{\Gamma(Z)} \tag{1.4}$$

the strength of the coupling to the Z boson (and therefore the decay width itself) depends on the nature of the decay particles. The first order partial decay widths into quarks and leptons are given by:

$$\Gamma(Z \rightarrow \ell\ell) = 8[(g_V^\ell)^2 + (g_A^\ell)^2]\Gamma_Z^0 \tag{1.5}$$
$$\Gamma(Z \rightarrow q\bar{q}) = 24[(g_V^q)^2 + (g_A^q)^2]\Gamma_Z^0 \tag{1.6}$$

where the decay products were taken to be massless and the extra factor of three in $\Gamma(Z \rightarrow q\bar{q})$ is a color factor,

$$\Gamma_Z^0 = \frac{G_F M_Z^3}{12\pi\sqrt{2}} \tag{1.7}$$

and g_V and g_A are the vector and axial coupling strengths, respectively.

1.2.3 Parton distribution functions

Figure 1.3 shows a schematic diagram of a $p\bar{p}$ collision leading to Z boson production and its subsequent decay into a pair e^+e^-. Intuitively, this figure suggests how the cross section for this process should be written. Let a parton of type a come from a hadron of type A, carrying a fraction x_a of the hadron's momentum. The probability to find this parton with momentum fraction x_a is $f_{a/A}(x_a)dx_a$. A second parton of type b, coming from a hadron of type B, carrying a fraction x_b with probability $f_{b/B}(x_b)dx_b$. The functions $f_{a/A}(x_a)$ and $f_{b/B}(x_b)$ are the parton distribution functions. Figure 1.4 shows the gluon and up quark distributions according to the CTEQ3M parton distribution set [13].

The factorization principle, which for this purpose can be taken as an established theorem of QCD [14], allows us to write the differential cross section for Z boson production as:

$$\frac{d^2\sigma}{dx_1dx_2} = \sum_{a,b}\int_{x_1}^{1} dt_p \int_{x_2}^{1} dt_{\bar{p}} \Phi_a(t_p,\mu_p^2)\Phi_b(t_{\bar{p}},\mu_{\bar{p}}^2)\frac{d^2\hat{\sigma}}{dx_1dx_2}(t_p,t_{\bar{p}},\mu^2) \tag{1.8}$$

where $t_p, t_{\bar{p}}$ are the fractions of momentum of the partons in p and $\bar{p}$, μ is the renormalization scale, $\Phi_{a,b}$ are the parton distribution functions, $\hat{\sigma}$ is the partonic cross section and a, b are the partonic flavors. In the infinite momentum frame, that is, assuming that the quark inside the proton do not carry any transverse momentum, a study of the longitudinal momentum distribution of the Z thus probes the x-distribution of the quark inside the proton.

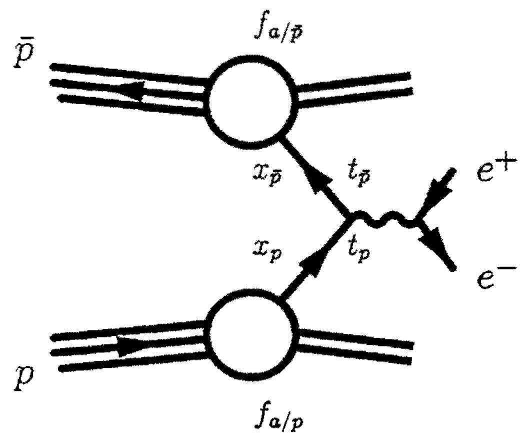

Figure 1.3: Schematic diagram of a $p\bar{p}$ collision.

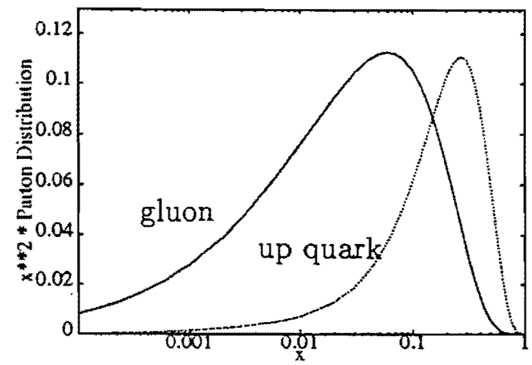

Figure 1.4: Gluon and up quark distributions in the proton according to the CTEQ3M parton distribution set [15].

The parton cross section can be calculated at the Born level in a straightforward manner, however, at the next to leading order and beyond, the calculation is not straightforward, but can be calculated using perturbative QCD. Parton distribution functions are calculated through "global fittings". Currently, there are several groups working on this task:

- Botts, Huston, Lai, *et al.* (CTEQ) [13].
- Martin, Roberts and Stirling (MRS) [16].
- Gluck, Reya and Vogt (GRV) [17].

The idea of a global fitting is to adjust the parton distribution functions to make theory and experiment agree for a wide range of processes. For example, recent CTEQ fits have used the following processes:

$$\begin{array}{ll}
e+p \to X & p+\bar{p} \to W \to \ell\bar{\ell}+X \\
\mu+p \to X & p+\bar{p} \to \gamma+X \\
\nu+\mathrm{Fe} \to X & \mu+{}^2H \to X \\
P+p \to \mu+\bar{\mu}+X & \bar{\nu}+\mathrm{Fe} \to \mu+\bar{\mu}+X \\
P+\mathrm{Cu} \to \mu+\bar{\mu}+X & p+{}^2H \to \mu+\bar{\mu}+X
\end{array}$$

The main features of a program of global fitting are as follows: one chooses a starting scale μ_0 (say 2 GeV), then one writes $f_{a/p}(x;\mu_0)$ in terms of several parameters for $a = g, u, \bar{u}, d, \bar{d}, s, \bar{s}$. Typically the heavy quark distributions, for $a = c, \bar{c}, b, \bar{b}, t, \bar{t}$ are generated from evolution, not from fits to data. For example, one may choose:

$$f_{a/p}(x;\mu_0) = Ax^B(1-x)^C(1+Ex^D) \tag{1.9}$$

The parton distributions obey certain flavor and momentum sum rules, such as:

$$\begin{aligned}\int_0^1 dx[f_{u/p}(x,\mu) - f_{\bar{u}/p}(x,\mu)] &= 2, \\ \sum_a \int_0^1 dx\, x f_{a/p}(x,\mu) &= 1 \end{aligned} \tag{1.10}$$

Then, one picks a trial set of parameters which determines $f(x;\mu_0)$ from which $f(x;\mu)$ is obtained for all μ by evolution. Next, given the $f(x;\mu)$, one generates theory curves for each type of experiment used, and the results are compared to the data. This sequence is iterated, adjusting the parameters to get the best fit.

1.3 Definition of variables and kinematics

The goal of this work is to obtain a measurement of the longitudinal momentum distribution of the intermediate vector boson Z:

$$\frac{d\sigma}{dx_Z} \quad \frac{d\sigma}{dx_1} \quad \frac{d\sigma}{dx_2}$$

where x_Z, x_1 and x_2 are defined as follows. Consider electron positron pair production by a proton-antiproton collision in a center of momentum frame defined such that the z-axis is along the $p\bar{p}$ beam direction and with a center of mass energy s; the four momenta of the p and $\bar{p}$ are:

$$\begin{aligned} p &= \left(\frac{\sqrt{s}}{2}, 0, 0, \frac{\sqrt{s}}{2}\right) \\ \bar{p} &= \left(\frac{\sqrt{s}}{2}, 0, 0, -\frac{\sqrt{s}}{2}\right) \end{aligned}$$

Let the initial state partons' momenta be k_1 and k_2 defined as:

$k_1 = x_1 p$ momentum of the parton carried by p

$k_2 = x_2 \bar{p}$ momentum of the parton carried by $\bar{p}$

then, the four momenta of the electron and positron will be:

$p_1^\mu = (E_1, \vec{E_{T_1}}, P_{L_1})$ (1) will be the index of the positron (electron)

$p_2^\mu = (E_2, \vec{E_{T_2}}, P_{L_2})$ (2) will be the index of the electron (positron)

where $\vec{E_{T_i}}$ are the transverse momenta and P_{L_i} are the longitudinal momenta. The rapidity is defined as:

$$y_i = \frac{1}{2} \ln \left(\frac{E_i + P_{L_i}}{E_i - P_{L_i}}\right) \tag{1.11}$$

Pseudorapidity η is the same as the rapidity if $(p_1)^2 = (p_2)^2 = 0$. η is defined as:

$$\eta = -\ln\tan\frac{\theta}{2} \tag{1.12}$$

where θ is the polar angle.

From now on we will neglect the mass of the electrons and positrons and make use of the pseudorapidity, then:

$$E_i = P_{L_i}\frac{\cosh\eta_i}{\sinh\eta_i} \tag{1.13}$$

$$(E_i)^2 = (E_{T_i})^2 + (P_{L_i})^2 \tag{1.14}$$

using the identity:

$$\sinh\eta = cot\ \theta \tag{1.15}$$

we obtain:

$$P_{L_i} = E_{T_i}\sinh\eta_i \tag{1.16}$$

In the case of leading order kinematics, where we consider only $2 \rightarrow 2$ processes $k_1 + k_2 = p_1 + \bar{p}_2$ and $E_{T_1} = E_{T_2}$ so:

$$x_1 - x_2 = \frac{2(P_{L_1} + P_{L_2})}{\sqrt{s}} \qquad (\equiv x_F) \tag{1.17}$$

$$x_1 x_2 = \frac{(p_1 + \bar{p}_2)^2}{s} \tag{1.18}$$

where x_F is the Feynman x. In $p\bar{p} \rightarrow Z \rightarrow e^+e^-$ reactions $(p_1 + \bar{p}_2)^2 = M_Z^2$ and Feynman x will be the fraction of momentum of the Z boson (x_Z). x_1 and x_2 can be obtained by solving equations (1.17) and (1.18):

$$x_1 x_2 = \frac{M_Z^2}{s} \quad \text{and} \quad x_1 - x_2 = x_Z \tag{1.19}$$

$$x_1 - \frac{M_Z^2}{s x_1} - x_Z = 0 \tag{1.20}$$

$$x_1^2 - x_Z x_1 - \frac{M_Z^2}{s} = 0 \tag{1.21}$$

$$(x_1)_{1,2} = \frac{x_Z \pm \sqrt{x_Z^2 + \frac{4M_Z^2}{s}}}{2} \tag{1.22}$$

Taking the positive solution for x_1 and choosing $x_1 > x_2$, we obtain:

$$x_{1,2} = \frac{1}{2}\left(\sqrt{x_Z^2 + \frac{4M_Z^2}{s}} \pm x_Z\right) \tag{1.23}$$

We could have also chosen variables η_1, η_2 and P_T to solve the system of equations (1.17) and (1.18) in which case the solution is not necessarily equal to the one we found here, for further discussion on this issue see reference [18].

Equations (1.17) and (1.23) are the definition of the observable to measure.

Chapter 2

The experimental equipment

Così ancor su per la strema testa
di quel settimo cerchio tutto solo
andai, dove sedea la gente mesta.[1]

Dante Alighieri. La Divina Commedia, INFERNO (Canto V)

In a hole in the ground, there lived a Hobbit.

J. R. R. Tolkien. The Hobbit

2.1 The accelerator complex at Fermilab

One of the most important elements in a high energy physics experiment is a particle accelerator machine capable to produce a beam with energy enough to create the particles of interest. Currently, Fermilab has the particle accelerator with the highest center-of-mass energy [19], figure 2.1 shows a diagram of the accelerator complex at Fermilab.

The Tevatron is the final stage of a series of accelerators operating at Fermilab. A Cockcroft-Walton, a linear accelerator (Linac) and a synchrotron (Booster) operate in series to produce 8 GeV protons to be injected in another synchrotron called Main Ring. The Main Ring has two tasks: it works as a final accelerator step to protons and antiprotons before being injected to the Tevatron and it is the source of energetic protons that are used to generate the antiprotons. The first colliding beams at Tevatron were delivered during accelerator tests in October 1985. DØ stored its first data from collisions in August 1992.

[1]So I went on alone and even further along the seventh circle's outer margin, to where the melancholy people sat.

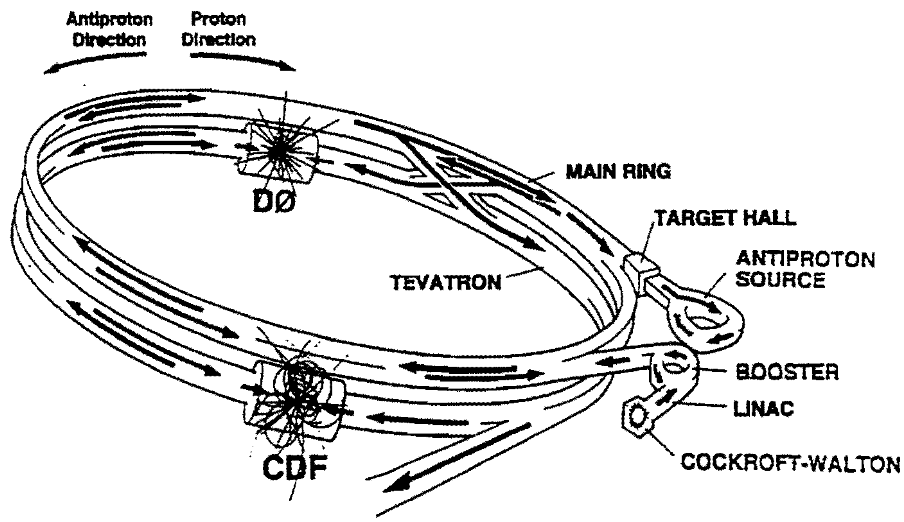

Figure 2.1: The Tevatron at Fermilab (collider mode).

The particles accelerating system at Fermilab consist of a negative hydrogen ion source, a Cockcroft-Walton generator, an electrostatic accelerating column and a transport line which injects the beam into the Linac.

The particle beam starts as a pulsated hydrogen ion beam (18 keV, 50mA) from a magnetron. A magnetron consists of an oval cathode surrounded by an anode with a magnetic field passing through the apparatus. The device is filled with hydrogen gas at a pressure of a few militorr. The combination of electric and magnetic fields generates a dense plasma confining the electrons to spiral in a space of about 1 mm between the cathode and the anode. The cathode is the active surface where the ^{-}H ions are generated. The positive ions and other energetic particles hit the cathode and disperse the hydrogen atoms that had been absorbed on the surface. After formation some of the ^{-}H ions are extracted through the anode aperture and are accelerated through the extraction plate. The fermilab source operates in a pulsed mode where the hydrogen gas input, the plasma discharge voltage and the extraction voltage are pulsed at a rate of 15 Hz which matches the Linac cycle and results in a longer source lifetime.

The voltage for the electrostatic accelerating column is produced by a commercial Cockcroft-Walton generator. This solid state device generates high voltage by charging capacitors in parallel from an AC voltage source and discharging them in series; this is possible due to the presence of several properly placed diodes. The Cockcroft-Walton has five stages resulting in a factor of ten in the increment of the maximum input voltage.

The Linac is approximately 150 m long and consists of nine independent tanks filled with drift tubes. Applying an alternating electric field, the particles travel trough the drift tubes hiding from the field outside when the field points in an opposite direction to the movement of the particles and traveling through the space between the tubes when the field points in the same direction accelerating the particles. Before entering the next acceleration stage, the ions are passed through a carbon film that removes the electrons leaving only the protons. The Linac increases the energy of the protons up to 400 GeV.

The next acceleration stage is done by a synchrotron, 151 m in diameter, with 96 magnets called Booster. A synchrotron is a circular accelerator using magnets to confine the particles to move in a circular orbit while experimenting the repeated action of an accelerating electric field in each revolution.

Protons travel roughly 20,000 times inside the Booster and its energy is incremented up to 8 GeV. The Booster repeats its cycle 12 times in rapid succesion, delivering twelve pulses (or bunches) of protons to the Main Ring. Currently the Booster delivers a beam with a total intensity of approximately 4.2×10^{12} protons [19].

The main ring is another proton synchrotron with a circumference of 6.3 km contained in a 3 m diameter tunnel, 6 m under the ground in the Illinois prairie. The Main Ring consists of 774 magnetic dipoles and 240 quadrupoles that bend and focus the trajectory of the protons besides accelerating them up to 150 GeV. A second task of the Main Ring is to generate 120 GeV protons that would be extracted to generate the antiprotons; this is the main duty of the Main Ring during collider runs.

To generate the antiprotons, protons are accelerated up to an energy of 120 GeV by the Main Ring, from where a pulse of 83 proton bunches are focused and directed to a nickel (or copper) target. As a result of the collision of the protons with the target a large quantity of secondary particles is generated –antiprotons included– and scattered in all directions. Antiprotons are focused by a lithium lens (a cylinder of liquid lithium which transforms a 500,000 A current pulse in a magnetic field that focuses the beam) [20] and directed to the first antiproton storage ring, called Debuncher which is 150 m in circumference.

The Debuncher was designed to increase the density of antiprotons using two cooling techniques; the first of them, called debunching is a Fermilab innovation: while an antiproton bunch travels through the ring a radiofrequency voltage accelerates the slowest particles and stops the fastest ones, reducing the energy distribution of the stored beam. The other technique, known as stochastic cooling, reduces the antiproton lateral movement . With this method, the particles whose orbits are far from an ideal orbit are identified by sensors which send correction signals to electrodes that adjust the trajectories of the erratic particles.

The antiprotons from the debuncher are sent to a concentric ring called Accumulator where several independent systems focus the antiproton beam even more increasing its density by a factor of 10^6; after about four hours the Accumulator contains enough antiprotons ($80 \sim 200 \times 10^{10}$) to be injected into the Main Ring and into the Tevatron. During collider run 1B the antiproton source was able to deliver up to 7.2×10^{10}

antiprotons per hour from 3.2×10^{12} protons per pulse incident in the production target every 2.4 seconds.

In the same tunnel where the Main Ring is installed –about 25 cm below it– there is another proton synchrotron called Tevatron, which consists of 1000 superconducting magnets operating at liquid helium temperature ($\simeq -270^o\ C$) and which allows to accelerate the protons up to almost 1 TeV.

Currently the Tevatron works in a "six times six" mode, i.e. with six proton bunches and six antiproton bunches traveling in opposite direction. Proton bunches contain approximately 150×10^9 particles while antiproton bunches contain 50×10^9 particles.

Once the Tevatron is loaded with the six proton bunches and the six antiproton bunches traveling in opposite directions, the energy of the bunches is increased up to 900 GeV and the beams are focused to a diameter of approximately 0.1 millimeter. At this energy, the bunches cross every 3.5 μs generating roughly 2.5 hard interactions per crossing with a luminosity of 45 mb.

Table 2.1 lists some of the Tevatron operation parameters during run 1B.

Parameter		Units
Protons per bunch	2.32×10^{11}	
Antiprotons per bunch	5.50×10^{10}	
Total antiprotons	3.30×10^{11}	
Proton emitancy	23π	mm-mr
Antiproton emitancy	13π	mm-mr
Beta interaction point	0.35	m
Energy	900	GeV
Number of bunches	6	
Bunch length (r.m.s.)	0.60	m
Peak luminosity	1.6×10^{31}	$m^{-2}\ sec^{-1}$
Integrated luminosity	3.2	pb^{-1}/w
Space between bunches	3500	nsec
Interactions per crossing (45 mb)	2.5	

Table 2.1: Tevatron operation parameters during collider run 1b.

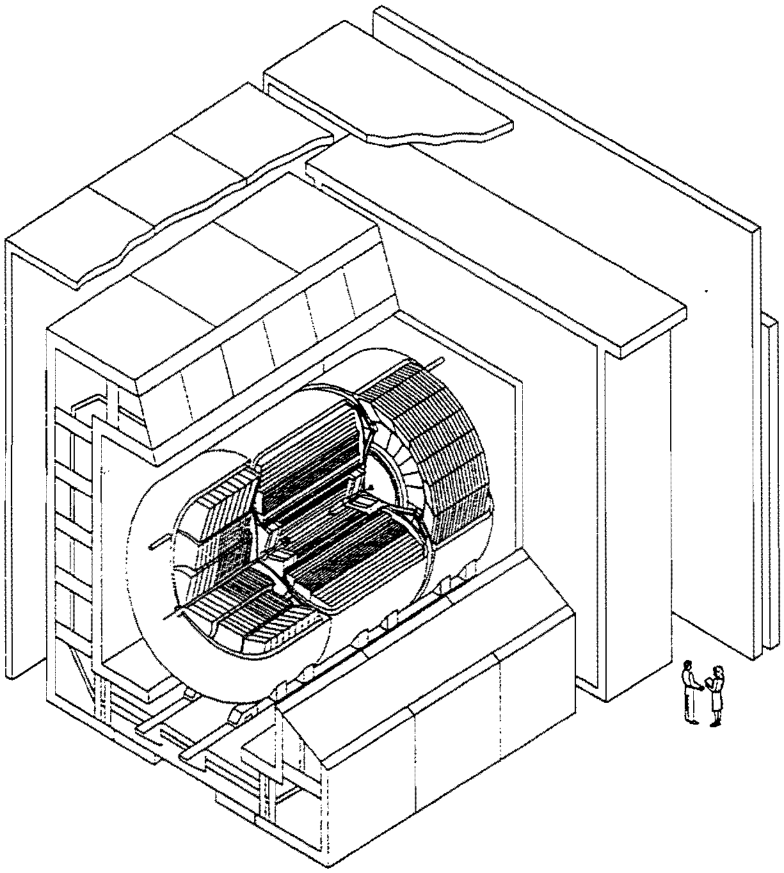

Figure 2.2: The DØ detector.

2.2 The DØ Detector

The DØ detector [21] was built with a prime physics focus of studying high mass states and large p_T phenomena among which are the search of the top quark (although DØ has published positive results from the search, studies are done to determine its mass with higher accuracy and some of its properties), precision studies of the W and Z bosons to give sensitive test of the standard electroweak model, several studies of perturbative QCD and the production of b-quark hadrons, and searches of new phenomena beyond the standard model. In this section it is given a description of the elements of the DØ detector and its data acquisition system. The DØ detector was optimized with the following three general goals in mind:

- Excellent identification and measurement of electrons and muons.
- Good measurement of parton jets at large p_T through highly segmented calorimetry with good energy resolution.

- A well-controlled measure of missing transverse energy ($\not\!\!E_T$) as an indication of the presence of neutrinos and other non-interacting particles.

The DØ detector consists of three major subdetection systems: the central detectors, the calorimeters and the muon system. Figure 2.2 shows an isometric view of the DØ detector.

2.2.1 Central detectors

The central detector (CD) consists of the tracking system and the transition radiation detectors. The individual systems are: (i) the vertex drift chamber (VTX), (ii) the transition radiation detector (TRD), (iii) the central drift chamber (CDC) and (iv) two forward drift chambers (FDC). The VTX, TRD and CDC cover the large angle region and are arranged in three cylinders concentric with the beams as it is shown in figure 2.3.

The CD set fits within a volume bounded by $r = 78$ cm and $z = \pm 135$ cm. The CD was designed to get a good spatial resolution of individual particles, a good separation between two tracks and a good determination of dE/dx to separate simple ionization tracks from double ionization tracks generated by photon conversions.

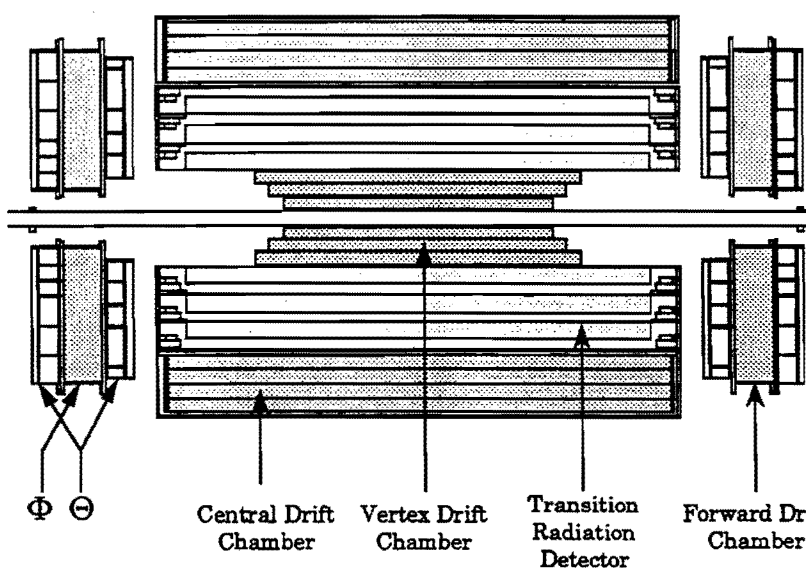

Figure 2.3: Array of the central detector showing the tracking system and the transition radiation detector at DØ.

2.2.1.1 Vertex chamber (VTX)

The vertex chamber is the innermost part of the tracking detector, it has an internal radius of 3.7 cm and an active radius of 16.2 cm. Inside the VTX chamber there are three concentric layers of mechanically independent cells.

The cells from the three layers are staggered in ϕ to increase the pattern recognition and facilitate calibration. The wires are 110 cm long and are placed parallel to the beam axis [22]. The cells are designed with a jet chamber geometry (the sense wires are arranged in planes which are parallel to the paths of particles emerging from the interaction region) with 8 sense wires and 9 guard wires in each of two planes, and additional cathode and field cage wires. Figure 2.4 shows the geometry of the cells in the (r, ϕ) plane transverse to the beam direction. The sense wires are staggered ± 100 μm to resolve left-right ambiguities. Some important parameters of the vertex chamber are shown in table 2.2.

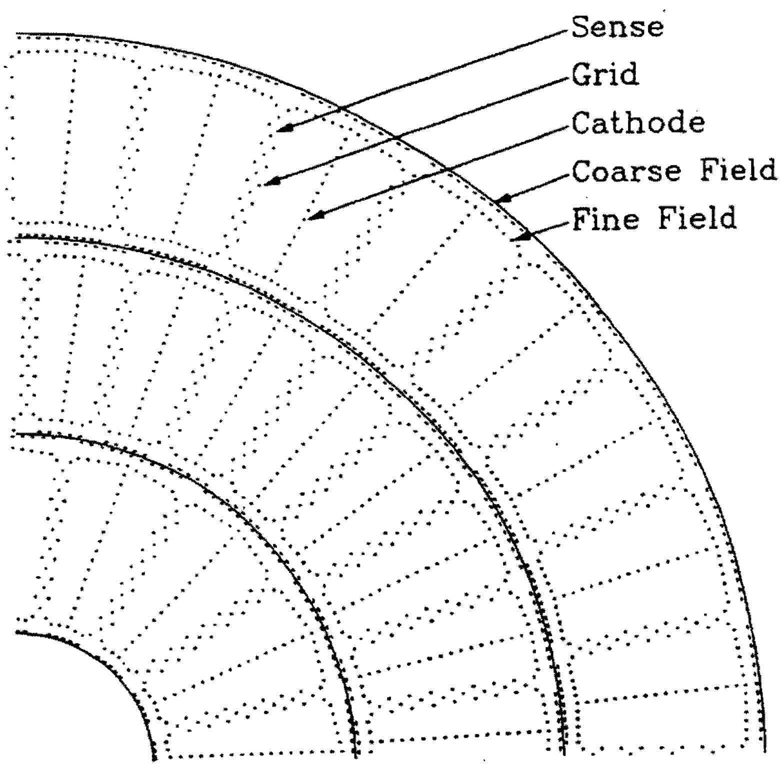

Figure 2.4: End view of one quarter of the wire plate for the vertex detector showing the three staggered layers.

Length of the active volume:	Layer 1	96.6 cm
	Layer 2	106.6 cm
	Layer 3	116.8 cm
Radial interval (active)		3.7 - 16.2 cm
Number of layers		3
Radial wire interval		4.57 mm
Number of sensor wires/cell		8
Number of sensor wires		640
Gas composition		CO_2(95%)-ethane(5%)-H_2O(0.5%)
Gas pressure		1 atm
Drift field		1.0-1.6 kV/cm
Average drift velocity		7.6-12.8 μm/ns
Gas gain at sense wires		4x10^4
Sense wire potential		+2.5 kV
Sense wire diameter		25 μm NiCoTin
Guard wire diameter		152 μm Au-plated Al

Table 2.2: Vertex chamber operation parameters.

2.2.1.2 Transition radiation detector (TRD)

The TRD detector is located in the space between the VTX and the CDC. It provides electron identification independently of the calorimeter. When a highly relativistic particle crosses the interface between two materials with different dielectric constant it generates transition radiation in the form of X rays. The TRD consists of three separate units, each of them with a radiator and an X ray detection chamber.

The X ray energy spectrum is determined by the thickness of the radiator layers and the gaps between the layers[2]. The radiators section in each TRD consists of 393 polypropylene foils, 18 μm thick and with a mean separation of 150μm between them; the gaps between them are filled with nitrogen gas.

X rays detection is performed by a two-step proportional wire chamber (PWC) mounted after the radiator. X rays are generally converted in the first stage of the chamber and the resulting charge is radially drifted to the sensor cells where the avalanche occurrs. Figure 2.5 shows the construction of the TRD with the conversion and amplification stages. The interaction length of X rays depends on the energy, but occurrs generally within the first millimeters of the conversion space. Besides the deposited charge by the transition X rays, ionization is produced by all the charged particles traversing the conversion and amplification regions. Conversions of X rays and δ rays produce charge clusters which arrive to the sensor wires within 0.6 μs of the drift time interval. Both, the magnitude and the time of arrival of the charge clusters

[2] In DØ the transition radiation spectrum for X rays peaks at8 GeV and it is, in general, below 30 GeV.

are useful to distinguish between electrons and hadrons.

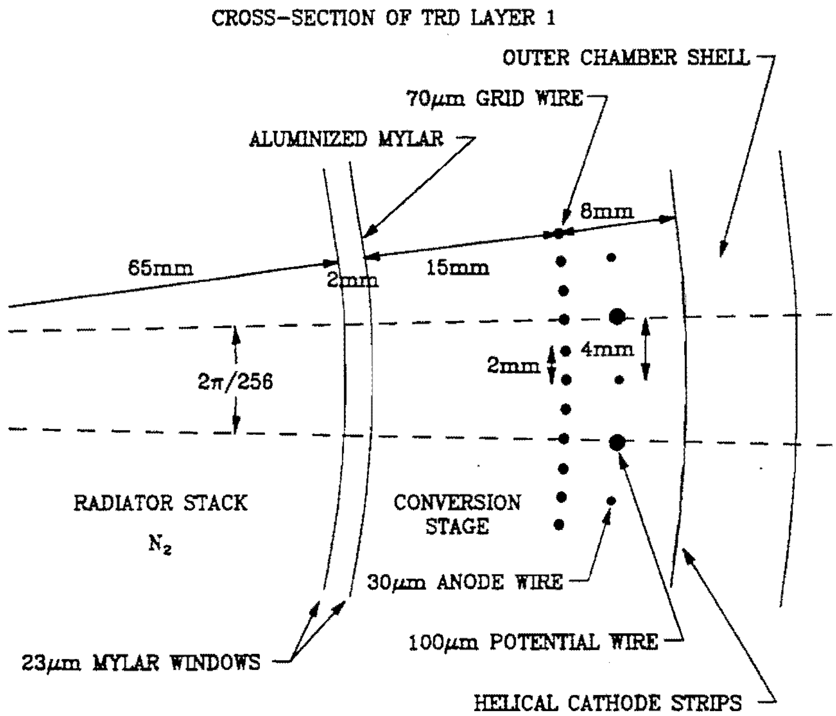

Figure 2.5: Different structures of the transition radiation detector.

2.2.1.3 Central drift chamber (CDC)

The central drift chamber allows to detect tracks at large angles after the TRD and before the central calorimeter. The CDC is a cylindrical layer, 184 cm long and with a radial coverture from 49.5 cm to 74.5 cm. Figure 2.6 shows a view of the CDC.

The CDC consists of 32 azimuthal cells per ring, each cell contains 7 tungsten sensor wires, 30 μm in diameter, output readout in one end and two delay lines located just before (after) the first (last) sensor wire; each one is readout in both ends. Adjacent wires inside cells are staggered in ϕ by $\pm$ 200 μm to avoid left-right ambiguities at the cell level. Besides, cells in alternate radii are displaced by half-cell to increase pattern recognition. The maximum drift distance is $\sim$ 7 cm. The CDC chamber operates with a gas mixture composed of Ar(92.5%), CH_4(4%), CO_2(3%) and 0.5% H_2O.

Some important parameters of the central drift chamber are summarized in table 2.3.

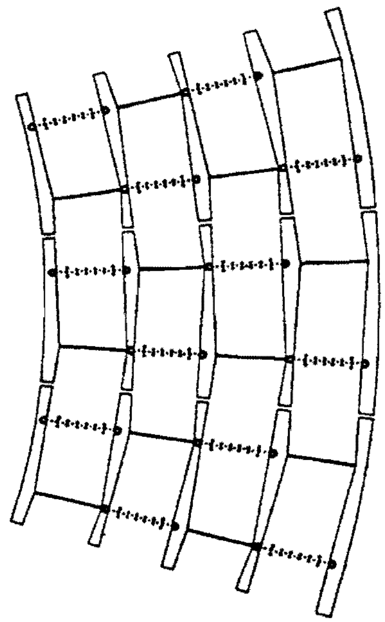

Figure 2.6: A view of three out of the 32 sectors of the CDC.

Active volume length	179.4 cm
Active radial interval	51.8 - 71.9 cm
Number of layers	4
Radial interval between wires	6.0 mm
Number of sensor wires/cell	7
Number of sensor wires	896
Number of delay lines	256
Gas composition	Ar(93%)-CH_4(4%)-CO_2(3%)-H_2O
Gas pressure	1 atm
Drift field	620 V/cm
Average drift velocity	34 μm/ns
Gas gain in the sensor wires	$2,6 \times 10^4$
Sensor wire potential	+1.5 kV
Sensor wire diameter	30 μm Au-plated W
Guard wire diameter	125 μm Au-plated CuBe

Table 2.3: Central drift chamber operation parameters.

2.2.1.4 Forward drift chambers (FDC)

Forward drift chambers increase track detection coverture of charged particles up to an angle $\theta \approx 5°$ with respect to the beam axis. As shown in figure 2.3, these chambers are located on each side of the concentric cylinders of the VTX, TRD and CDC and just before the walls of the end calorimeters. These chambers have a radius slightly smaller than the large angle chambers' radius ($r \leq 61$ cm) to allow passage of the cables from the inner chambers.

Each FDC consists of three separate chambers: a Φ module which sensor wires are radial and which measures the ϕ coordinate, and two Θ modules which sensor wires measure the θ coordinate. Figure 2.7 shows the layout of the Φ and Θ modules in a FDC. Table 2.4 summarizes the operation parameters of a FDC.

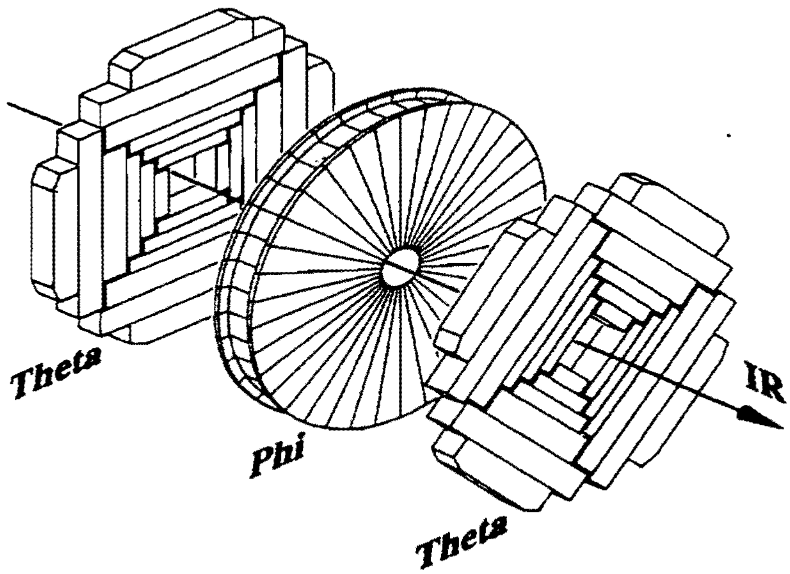

Figure 2.7: View of the three modules of a FDC.

2.2.1.5 Central detector electronics

The electronics for reading out the signal from the central detectors is practically the same for all the devices in the central detector. There are three stages in the signal processing: the preamplifiers are directly mounted in the chambers, the shapers are located on the platform of the detector and the ADC digitizers are located on the MCH. Overall, the tracking detector and the TRD use 6080 channels.

2.2.1.6 Performance of the central detector

All the tracking detectors at DØ have been operated with test beams and cosmic rays to test the performance and measure the efficiencies of its operation parameters in order to compare them with the design parameters.

The measured resolutions for the vertex chambers are 50μm for the CDC and for the FDC the resolutions varied between 150 and 200 μm. Another important parameter

	Θ *modules*	Φ *modules*
z interval	104.8-111.2 cm 128.8-135.2 cm	113.0-127.0
Radial interval	11-62 cm	11-61.3 cm
Number of cells per radius	6	
Maximum drift distance	5.3 cm	5.3 cm
Stagger of sense wires	0.2 mm	0.2 mm
Sensor wire separation	8 mm	8 mm
Angular interval/cell		10°
Number of sensor wires per cell	8	16
Number of delay lines per cell	1	0
Number of sense wires/end	384	576
Number of delay lines read out/end	96	
Gas mixture	Ar(93%)-CH_4(4%)-CO_2(3%)-H_2O	
Gas pressure	1 atm	1 atm
Drift field	1.0 kV/cm	1.0 kV/cm
Average drift velocity	37 μm/ns	40 μm/ns
Gas gain at sense wire	$2.3, 5.3 \times 10^4$	3.6×10^4
Sense wire potential	+1.5 kV	+1.5 kV
Sense wire diameter	30 μmAu-plated W	
Guard wire diameter	163 μm Au-plated Al(5056)	

Table 2.4: Forward drift chamber design parameters.

in the non-magnetic environment of the DØ detector is the pulse pair resolution. The VTX reaches an efficiency of 90 % for two hits with a separation of 0.63 mm, while at the FDC and CDC, the 90 % efficiency is reached for separations in the order of 2 mm.

It is also important to know the resolution power between two overlapped tracks (i.e. in the case of photon conversions) and one track. The studies performed using the FDC showed a resolution of energy loss of 13.3 % for simple tracks. The studies performed using the CDC and the VTX showed rejection factors in the range of 75–100 for a 98 % efficiency keeping single tracks.

The ability of the TRD to discriminate electrons from hadrons has been studied in some detail in test beams and the results compared to Monte Carlo calculations. Measures of the difference between electrons and hadrons include the total collected charge on anode wires, the number of charge clusters and the position of clusters determined through the time of arrival at the anodes. The studies showed pion rejection of approximately 50 for 90 % efficiency for electrons.

2.2.2 The DØ calorimeters

2.2.2.1 Calorimeter design issues

The design of the calorimeter is crucial for the optimization of the DØ detector; since there is no central magnetic field, the calorimeter must provide the energy measurement for electrons, photons and jets. In addition, the calorimeter plays an important role in the identification of electrons, photons, jets and muons as well as in the determination of the transverse energy balance in the event.

The final design of the calorimeter included the use of liquid argon as the active medium to sample the ionization produced in electromagnetic or hadronic showers. Among the advantages of this design stand out the unit gain of the liquid argon, the simplicity of calibration, the flexibility to segment the calorimeter in longitudinal and transversal cells, the radiation hardness and the relatively low unit cost for readout electronics. Some of the negative factors of this design are the complicated cryogenic system, the need for massive containing vessels as cryostats which leave regions of uninstrumented material and the inaccessibility of the calorimeter modules during operation.

Given the need of access to the central detector the design shown in figure 2.8 was chosen, a central calorimeter (CC) covers the region $|\Delta\eta| \leq 1$ and a pair of end calorimeters ECN (north) y ECS (south) extends the coverage up to $|\eta| \approx 4$.

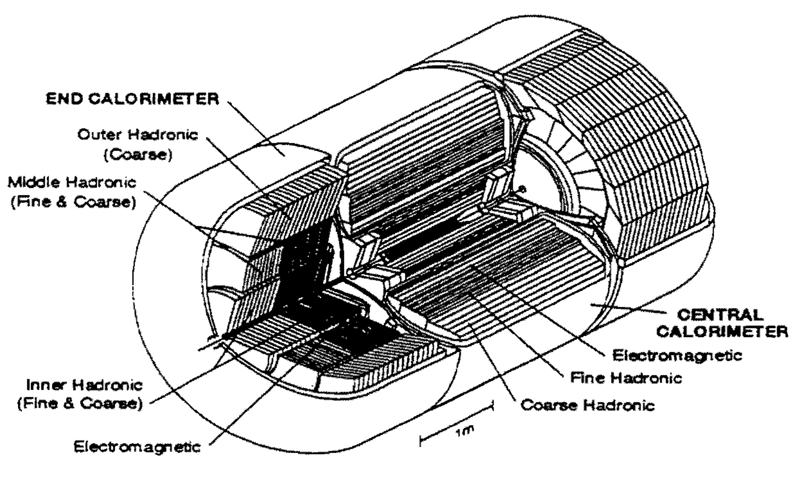

Figure 2.8: Isometric view showing the central calorimeter and the two end calorimeters.

The calorimeter dimensions were bounded by the size of the experimental hall, the need of an adequate depth to ensure a complete containment of showers and the need for sufficient tracking coverage in front of the calorimeter. In the final design there are three types of modules in both the CC and the EC: an electromagnetic section (EM) with thin uranium plates, a fine hadronic section with thicker uranium plates and a coarse hadronic section with thick copper or stainless steel plates.

The coarse sections allow sampling of the hadronic showers while keeping the density high (and hence the outer radius small). Except at the small angles in the EC 16 or 32 modules of each type are arranged in a ring. At $\eta = 0$ the CC has 7.2 nuclear absorption lengths (λ_A) and at the smallest angle of the EC there are 10.3 λ_A.

Figure 2.9 shows a unitary cell of the calorimeter. The electric field is established by grounding the metal absorber plate and connecting the resistive surfaces of the signal boards to a positive high voltage (typically 2.0–2.5 kV). The electron drift time across the 2.3 mm gap is $\approx$ 450 ns. The gap thickness was chosen to be large enough to observe minimum ionizing particle signals. The absorber plates are made of different materials in different regions, the EM modules both in the CC and in the EC have plates of depleted uranium 3 and 4 mm thick, respectively. The fine hadronic module sections have 6 mm thick uranium-niobium (2%) alloy. The coarse hadronic module sections have 46.5 mm thick plates of either copper (CC) or stainless steel (EC).

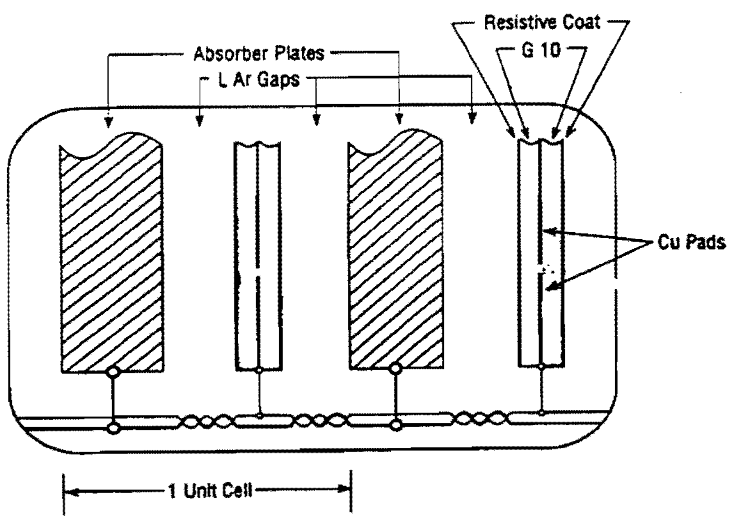

Figure 2.9: Schematic view of a unitary cell of the calorimeter showing the liquid argon gap and the signal board.

The size and shape of the readout cells were determined from several considerations. The transverse sizes were chosen to be comparable to the size of the showers: $\sim$ 1–2 cm for the electromagnetic showers and $\sim$ 10 cm for the hadronic showers. In the η–ϕ plane the scale was fixed by the size of parton jets, $\Delta r = \sqrt{\Delta\eta^2 + \Delta\phi^2} \sim 0.5$. Longitudinal subdivision within the EM, fine hadronic and coarse hadronic sections is useful since the longitudinal shower profiles help to distinguish electrons and hadrons.

The final design presents a "pseudo-projective" set of readout towers, with each tower subdivided in depth. The term pseudo-projective refers to the fact that the centers of cells of increasing shower depth lie on rays projecting from the center of the interaction region, but the cell boundaries are aligned perpendicular to the absorber plates. Figure 2.10 shows the segmentation pattern of the DØ calorimeter.

There are four depth layers for the EM modules in CC and EC, the first two layers are 2 radiation lengths (X_0) thick and are included to measure the longitudinal shower development near the beginning of the showers where photons and π^0s differ statistically. The third layer spans the region of maximum EM shower energy deposits and the fourth completes the EM coverage up to approximately 20 X_0.

The fine hadronic modules are segmented into three or four layers while the coarse hadronic are segmented into one or three layers. The transverse size of the towers, in both the EM and hadronic modules are $\Delta\eta = 0.1$ and $\Delta\phi = 2\pi/64 \simeq 0.1$. The third section of the EM modules is doubly segmented both in η and ϕ to allow a more precise localization of the electromagnetic shower centroids.

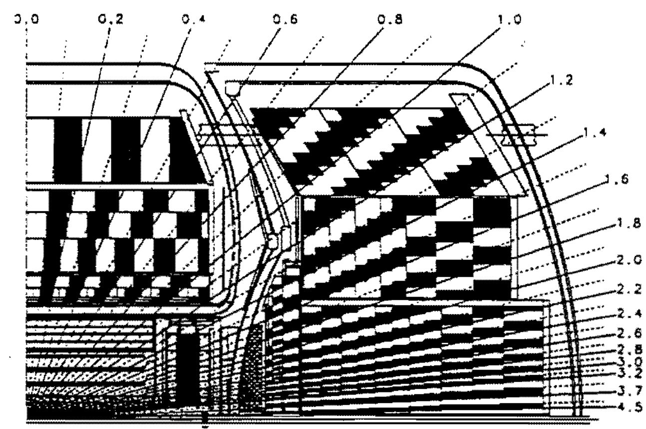

Figure 2.10: Schematic view of a portion of the DØ calorimeter showing the longitudinal and transverse segmentation patterns.

2.2.2.2 Central calorimeter

The central calorimeter consists of three concentric cylindrical shells that have a radial coverage of $75 < r < 222$ cm from the beam center and a longitudinal coverage of 226 cm; there are 32 EM modules in the inner ring, 16 fine hadronic (FH) modules in the surrounding ring and 16 coarse hadronic (CH) in the outer ring. The module boundaries are rotated so that no projective ray encounters more than one intermodule gap. Table 2.5 shows some of the design specifications for the central calorimeter.

	EM	FH	CH
Rapidity coverage	± 1.2	± 1.0	± 0.6
Number of modules	32	16	16
Absorber material[a]	Uranium	Uranium	Copper
Absorber material thickness (cm)	0.3	0.6	4.65
Argón gap (cm)	0.23	0.23	0.23
Number of cells/module	21	50	9
Longitudinal depth	20.5 X_0	3.24 λ_0	2.93 λ_0
Number of readout layers	4	3	1
Cells/readout layer	2, 2, 7, 10	21, 16, 13	9
Total radiation lengths	20.5	96.0	32.9
Radiation length/cell	0.975	1.92	3.29
Total absorption lengths (Λ)	0.76	3.2	3.2
Absorption lengths/cell	0.036	0.0645	0.317
Sampling fraction (%)	11.79	6.79	1.45
Segmentation ($\eta \times \phi$)[b]	0.1 × 0.1	0.1 × 0.1	0.1 × 0.1
Total number of readout cells	10,368	3,456	768

Table 2.5: Central calorimeter operation parameters.

[a]The uranium is depleted and the FH absorbers contain a 1.7% niobium alloy.
[b]The third EM layer has 0.05 × 0.05.

2.2.2.3 End calorimeters

The two end calorimeters (ECN y ECS) contain four module types as shown in figures 2.8 and 2.10. To avoid the dead spaces in a multi-module design, there is just one EM module and one inner hadronic (IH) module as shown in figure 2.11. Outside the EM and IH modules there are concentric rings of 16 middle and outer (MH and OH) modules, the azimuthal boundaries of the MH and OH modules are offset to prevent cracks through which particles could penetrate the calorimeter. Table 2.6 shows the design specifications of the end calorimeters.

2.2.2.4 Intercryostat detectors and massless gaps

As shown in figure 2.10, the region $0.8 \leq |\eta| \leq 1.4$ contains a large amount of uninstrumented material in the form of cryostat walls, stiffening rings and module endplates. To correct for energy deposited in the uninstrumented walls there are two scintillation counter arrays called intercryostat detectors (ICD) that are mounted on

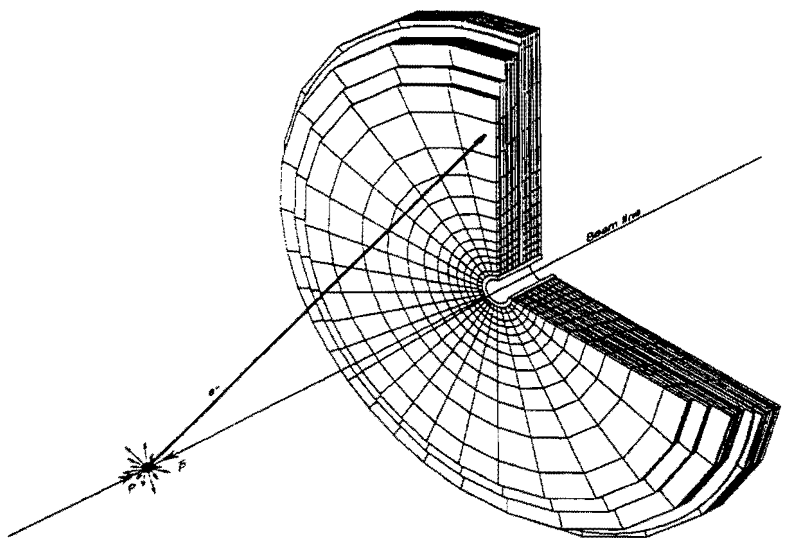

Figure 2.11: View of an ECEM module.

	EM	IFH	ICH	MFH	MCH	OH
Rapidity coverage	1.3-4.1	1.6-4.5	2.0-4.5	1.0-1.7	1.3-2.0	0.7-1.4
Number of modules/End calorimeter	1	1	1	16	16	16
Absorbing material[a]	U	U	SS[b]	U	SS	SS
Absorbent thickness (cm)	0.4	0.6	4.6	0.6	4.6	4.6
Argon gap (cm)	0.23	0.21	0.21	0.22	0.22	0.22
Number off cells/Module	18	64	12	60	12	24
Longitudinal depth	$20.5X_o$	$4.4\lambda_o$	$4.1\lambda_o$	$3.6\lambda_o$	$4.4\lambda_o$	$4.4\lambda_o$
Number of readout cells	4	4	1	4	1	3
Cells/readout layer	2, 2, 6, 8	16	12	15	12	8
Total radiation lengths	20.5	121.8	32.8	115.5	37.9	65.1
Total absorption lengths (Λ)	0.95	4.9	3.6	4.0	4.1	7.0
Sampling fraction (%)	11.9	5.7	1.5	6.7	1.6	1.6
Segmentation $\Delta\phi$[c]	0.1	0.1	0.1	0.1	0.1	0.1
Segmentation $\Delta\eta$[d]	0.1	0.1	0.1	0.1	0.1	0.1
Total number of readout channels[e]	14976	8576	1856	2944	768	1784

Table 2.6: Design parameters of the end calorimeters.

[a]Depleted uranium. The absorbing material in modules FH (IFH and MFH) contains a 1.7% niobium alloy.
[b]Stainless steel
[c]The third layer of EM $\Delta\phi \times \Delta\eta = 0.05 \times 0.05$ for $|\eta| < 2.6$
[d]For $|\eta| > 3.2, \Delta\phi = 0.2\ \Delta\eta \approx 0.2$
[e]MCH y OH are added together in $|\eta| = 1.4$

the surface of the ECs (see figure 2.10). Each ICD consists of 384 scintillator tiles of size $\Delta\eta = \Delta\phi = 0.1$ exactly matching the liquid argon calorimeter cells. In addition, separate single cell structures called massless gaps are installed in both CC and EC calorimeters. Together, the ICD and massless gaps provide a good approximation to the standard DØ sampling of EM showers.

2.2.2.5 Calorimeter readout

The signals from the calorimeter modules are brought to the four cryostat feed-through ports by specially fabricated cables, these cables are connected to multi-layer printed circuit feedthrough boards. Short cables connect the output from the feedthrough boards to charge sensitive preamplifiers mounted in four enclosures on the surface of each cryostat, near the ports.

The preamplifiers were made with two different gains (equivalent full scale gains of about 100 and 200 GeV) to provide a full dynamic range response. Output signals from the preamplifiers are transported some 30 m to the baseline subtractor (BLS) shaping and sampling circuits. Depending on the signal size the BLS outputs can be amplified by 1 or by 8 so as to reduce the dynamic range requirements of subsequent digitization. The BLS outputs are sent from the detector platform to the moving counting house (MCH).

2.2.2.6 Calorimeter performance

The DØ calorimeters have been tested in a variety of ways. Prototype studies in test beams have verified performance goals and led to the optimization of the design.

Extensive studies of the performance of modules were made using pions and electrons with energies between 10 and 150 GeV. The response to both electrons and pions is linear to beam energy within 0.5%.

The relative resolution as a function of energy of the ECEM and ECMH modules can be parametrized as:

$$\left(\frac{\sigma_E}{E}\right)^2 = C^2 + \frac{S^2}{E} + \frac{N^2}{E^2} \tag{2.1}$$

where the constants C, S and N represent the calibration errors, sampling fluctuations and noise contributions respectively. The results obtained for these constants are:

$$\begin{array}{lll} C = 0.003 \pm 0.002 & S = 0.157 \pm 0.005\sqrt{\mathrm{GeV}} & \text{for electrons in ECEM} \\ C = 0.032 \pm 0.004 & S = 0.41 \pm 0.04\sqrt{\mathrm{GeV}} & \text{for pions in ECMH} \end{array}$$

The calorimeter position resolution varies between 0.8 and 1.2 mm over the full range of impact positions: the position resolution varies approximately as $\sqrt{E}$.

The resolution and linearity obtainable in the calorimeter are closely related to the ratio of response of electrons and pions. The e/π response ratio falls from about 1.11 at 10 GeV to about 1.04 at 150 GeV.

2.2.3 The muon system

The DØ muon detection system consists of five separate solid-iron toroidal magnets surrounded by proportional drift chambers (see figure 2.12). These measure charged particle track trajectories down to approximately 3 degrees from the beam pipe. This system enables DØ to identify muons and measure their trajectories and momenta. Muon momenta are measured using the bend angle determined between the trajectories before and after the magnets. The strength of the field is approximately 2 Tesla.

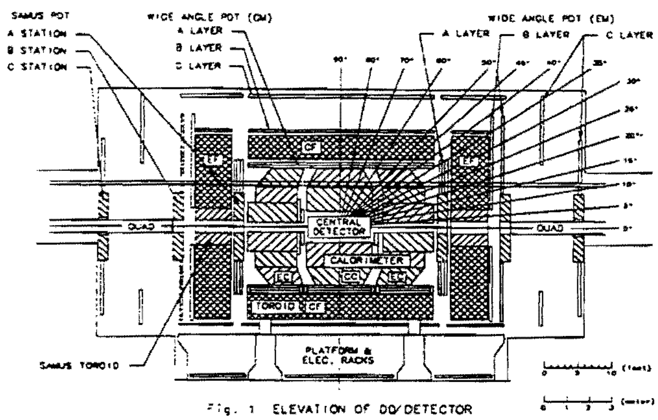

Figure 2.12: Cross section view of the DØ muon system.

Magnetic field strength	2 T
Magnetic kick (90°)	0.61 GeV/c
System precision goal in bend plane	500 μm (Diffusion limit, 200 μm)
System precision goal in non-bend plane	2-3 mm (charge ratio, $\pm$1.0%)
$\delta p/p$ (multiple scattering limit)[a]	18%
3σ sign determination (θ, ϕ 90°,0°)	$P_t \leq$350 GeV/c
Interaction lengths (90°)	13.4
Interaction lengths (5°)	18.7
Drift-coordinate resolution	$\pm$0.45 mm

Table 2.7: Design parameters of the DØ muon system.

[a] Absolute theoretical limit assuming 100% chamber efficiency.

The incident trajectory is determined from the primary interaction point, central tracking, and the first layer of muon chamber. Multiple Coulomb scattering in the calorimeters and iron toroids limits the relative momentum resolution to $\geq 18\%$. The precision of defining position and angle is ± 0.3 mm and ± 0.6 mrad, respectively, for the first muon chamber. The expected precision in determining the angle and position of the outgoing particle from the iron measured in the subsequent two layers of the PDT's are ± 0.2 mrad and ± 0.17 mm respectively. Table 2.7 summarizes the design parameters of the muon system. Since the current analysis does not involve the use of muons, we are not further discussing the muon system of the DØ detector.

2.2.4 Trigger and data acquisition

The DØ trigger and data acquisition system are used to select and record interesting physics and calibration events. The trigger has three levels: the Level 0 scintillator based trigger indicates the occurrence of an inelastic collision. At a luminosity of $\mathcal{L} = 10^{30}\ \mathrm{cm}^{-2}\mathrm{s}^{-1}$ the Level-0 rate is about 150 kHz. Level 1 is a collection of hardware trigger elements, many Level 1 trigger operate within the 3.5 μs time interval between beam crossings contributing no deadtime. Others require several bunch crossing times to complete and are referred as Level 1.5 triggers. The rate of successful Level 1 triggers is about 200 Hz, and after the action of Level 1.5 triggers the rate is reduced to under 100 Hz. Figure 2.13 shows a flux diagram of the DØ trigger system indicating the decreasing rates at each level.

Candidates from Level 1 are passed on the standard DØ data acquisition pathways to a farm of microprocessors which serve as event builders as well as the Level 2 trigger systems. Level 2 reduces the rate to about 2 Hz before passing the events on to the host computer for event monitoring and recording on permanent storage media. A block diagram of the trigger and data acquisition system is shown in figure 2.14.

2.2.4.1 Level 0 trigger

The Level 0 trigger registers the presence of inelastic collisions and serves as the luminosity monitor for the experiment. It uses two hodoscopes of scintillation counters mounted on the front surfaces of the end calorimeters with a coverage for the rapidity range $1.9 < \eta < 4.3$, and nearly full coverage for $2.3 < \eta < 3.9$. The Level 0 efficiency for detecting single inelastic collisions was measured to be 90.7 ± 1.65 % [23], while the measured overall Level 0 efficiency for W and Z events is 98.55 % [23].

Besides identifying inelastic collisions, the Level 0 provides information on the z-coordinate of the primary collision vertex. The z-coordinate is calculated using the difference in arrival time for particles hitting the two Level 0 detectors. The time resolution of each Level 0 counter was measured using cosmic rays. The time resolution turned out to be of the order of 100-150 ps, which is well matched to the required vertex position accuracy.

2.2.4.2 Level 1 framework

The Level 1 (L1) framework is a hardware device used to select physics events of interest. Its purpose is to provide a fast decision to keep or discard an event based on the results of individual L1 components (triggers), as well as interfacing with Level 2. Part of L1 can accomplish its task within the 3.5 μs between crossings and that is properly referred as L1, while the rest of the framework that takes a larger time to complete its work is referred to as Level 1.5.

The primary input to the framework consists of 256 trigger terms indicating that some requirement is met for the current event. These inputs come either from detector specific L1 processors or directly from sources such as scintillators or accelerator timing signals. The 256 trigger terms are reduced to a set of 32 L1 trigger bits by an AND/OR network. Each trigger bit has also a programmable prescale which allows a balanced recording of events with low or high frequency of occurrence.

In addition L1 coordinates various vetos which can inhibit triggers, correlates the trigger and readout functions, manages the communication tasks with the front-end electronics and with the trigger control computer, and provides a large number of scalers which allow accounting of trigger rates and deadtimes.

If Level 1.5 confirmation of a specific trigger is required, the framework forms the

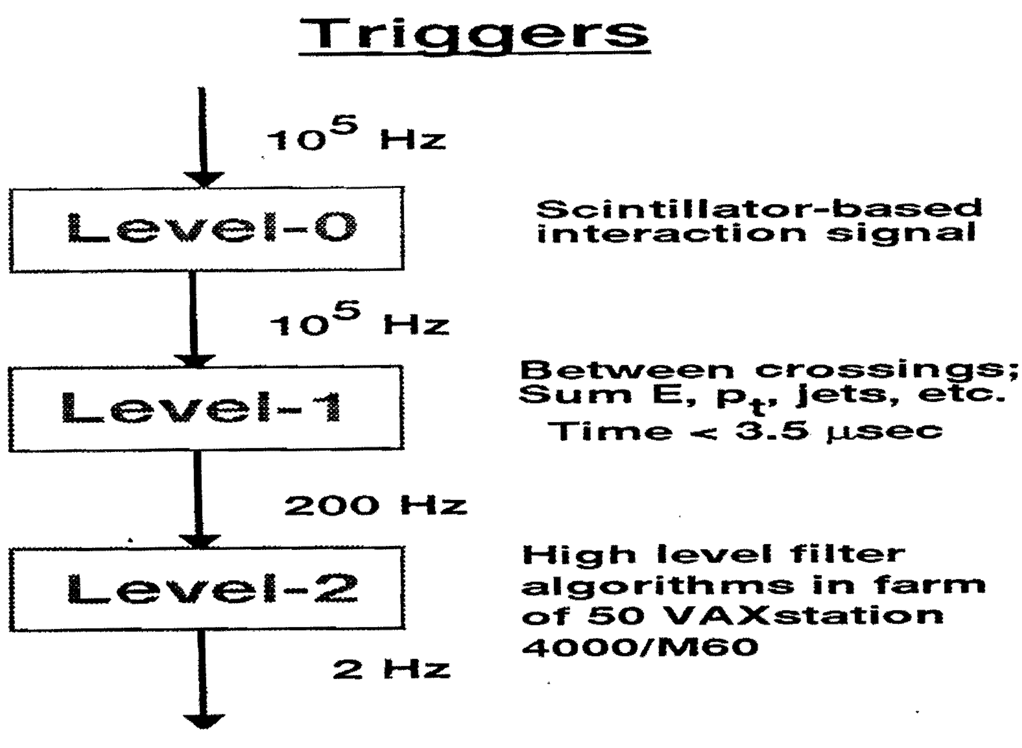

Figure 2.13: Flux diagram of the DØ trigger.

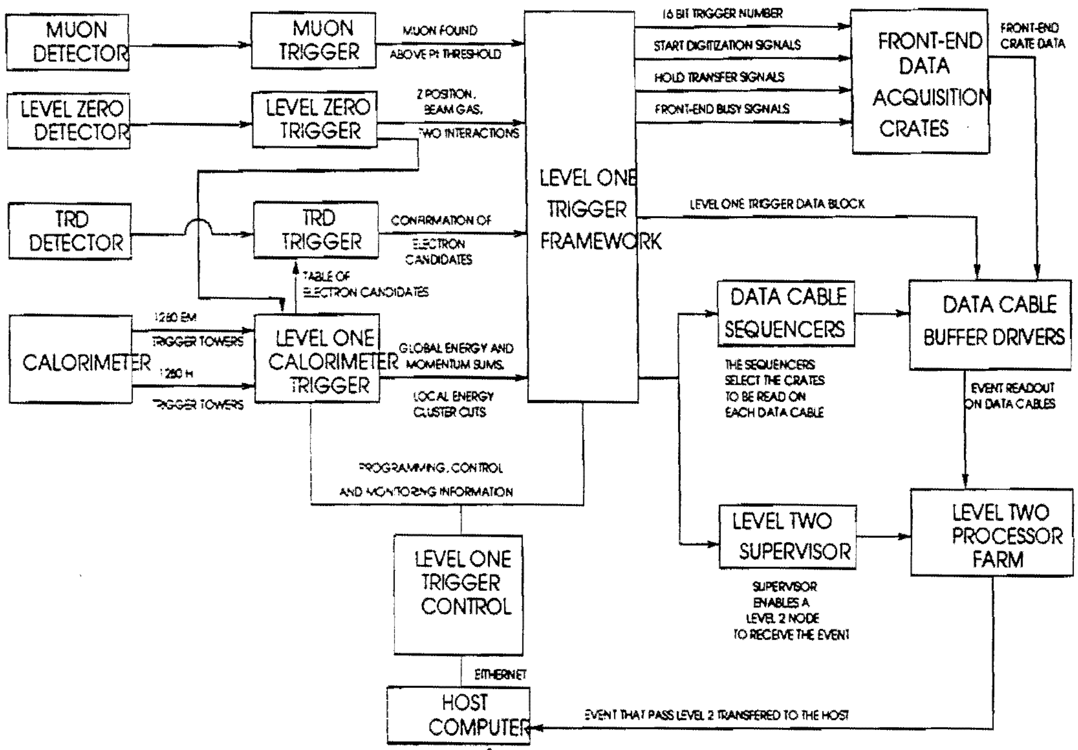

Figure 2.14: Diagram of the DØ trigger showing individual trigger components and their interconnections.

Level 1.5 decision and communicates the results to the data acquisition hardware. L1 assembles a block of information summarizing all the conditions leading to a positive Level 1 decision (and Level 1.5 confirmation if required) for transmission to the succeeding levels of analysis.

Main Ring vetos

Since the Main Ring passes through the DØ detector, losses from the Main Ring will show up in the detector and must be rejected. These losses are dealt with by vetoing on the `MRBS_LOSS` trigger term, which results in a dead time of about 17 %.

It is also possible to have small losses whenever the Main Ring bunch passes through the detector, these can be eliminated by vetoing on the microblank trigger term, which is asserted whenever the Main Ring bunch is present in the detector during the livetime of the muon system. This veto adds an additional 8% deadtime.

Level 1 TRD trigger

The information collected in the transition radiation detector is zero-suppresses after being digitized. The zero-suppression circuit also sums the signal and makes them available for a refined Level 1.5 TRD trigger. The purpose of the TRD trigger is to certify electron candidates found in the Level 1 calorimeter trigger.

Level 1 calorimeter trigger

The L1 calorimeter trigger is responsible for making trigger decisions based on calorimeter information. This is a pure L1 trigger. Its inputs derive from the trigger pickoffs in the calorimeter BLS cards, which sums cells into towers of size 0.2×0.2 in $\eta - \phi$ out to a pseudorapidity of 4. At the input of the calorimeter trigger all inputs are simultaneously flash digitized and all subsequent calculations are entirely digital. The trigger calculates several global sums of calorimeter inputs. These sums are:

- The total electromagnetic energy: $E(\text{em}) = \sum_i E_i(\text{em})$.
- The total hadronic energy: $E(\text{had}) = \sum_i E_i(\text{had})$.
- The total scalar sum of electromagnetic transverse energy: $E_T(\text{em}) = \sum_i E_i(\text{em}) \sin\theta_i$.
- The total scalar sum of hadronic transverse energy: $E_T(\text{had}) = \sum_i E_i(\text{had}) \sin\theta_i$.
- The total transverse energy: $E_T(\text{tot}) = E_T(\text{em}) + E_T(\text{had})$
- The missing transverse energy: $\not{E}_T = \sqrt{E_x^2 + E_y^2}$, where:

$$E_x = \sum_i (E_i(\text{em}) + E_i(\text{had})) \sin\theta_i \cos\phi_i$$

and

$$E_y = \sum_i (E_i(\text{em}) + E_i(\text{had})) \sin\theta_i \sin\phi_i$$

These quantities are then compared with a set of programmable thresholds, from this comparison a trigger term is obtained which is later input to the trigger framework.

2.2.4.3 Level 2 filter

The Level 2 filter is primarily a very large farm of general purpose processors which run software filters using the complete data set for an event. The filtering process is built around a series of filter tools, and each tool has a specific function related to a identification of a type of particle or event characteristic. Among the tools are those for jets, muons, calorimeter EM clusters, track association with calorimeter clusters, $\sum E_T$ and missing E_T. Other tools recognize specific noise or background conditions. The tools are associated in particular combinations and orders into "scripts"; a specific script is associated with each of the 32 L1 trigger bits. The script can spawn several Level 2 filters from a given L1 trigger bit. There are 128 Level 2 filter bits available in all.

The Level 2 nodes are coordinated through the host computer, provision is made for run-time distributions of parameters to the nodes, for collecting statistics on the processing history of the nodes and collection of error statistics and alarms.

2.2.4.4 Data acquisition system

The DØ data acquisition system is closely intertwined with the Level 2 trigger hardware. The system is based upon a farm of 50 parallel nodes connected to the detector electronics and triggered by a set of eight 32-bit wide high speed data cables. All the data for a specific event is sent over parallel paths to memory modules in a specific, selected node (one of the 50). The event data is collected and formatted in final form in the node, and the Level 2 filters are executed. The events are logged to a staging disk and a sample is dispatched to the various workstations for on-line monitoring purposes. Recording occurrs at rates up to approximately three 500 kbyte events per second. Figure 2.15 shows a schematic diagram of the DØ data logger.

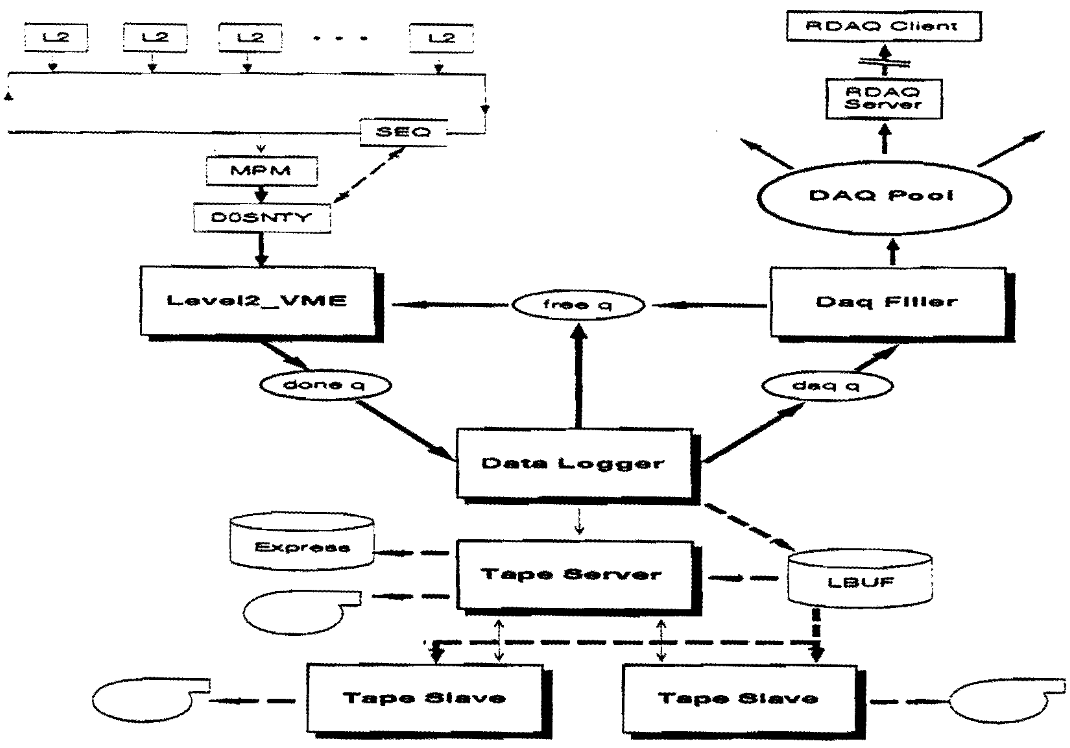

Figure 2.15: Schematic diagram of the DØ data logger.

Chapter 3

Event reconstruction and data selection

It is a capital mistake to theorize before one has data.

Arthur Conan Doyle.

The best way to do it is with scissors.

Alfred Hitchcok.

Electrons and photons, as well as hadrons are seen by the DØ detector as clusters of energy deposited in the layers of the calorimeter. It is important to establish a set of characteristics of these clusters that allow identification of the different particles. In this chapter we will discuss the reconstruction algorithms as well as the standard cuts employed in the selection of the reconstructed electrons.

3.1 Electron reconstruction

The DØ detector was designed so that electromagnetic particles would deposit most of their energy in the electromagnetic layers of the calorimeter.

The reconstruction of electrons and photons uses a nearest neighbor (NN) algorithm [24] based on the energy of the electromagnetic towers; an electromagnetic tower consists of the four EM and the first hadronic (FH1) layers of the calorimeter. The towers are grouped together by connecting every tower in the calorimeter with the tower in its local neighborhood with the highest energy if the energy is above a threshold. These connections define clusters of mutually connected towers in the calorimeter.

For each calorimeter cluster found its kinematic properties are calculated. After all possible clusters have been identified, the ones which pass the following cuts are considered as electron or photon candidates:

- Total energy of the cluster > 1.5 GeV
- Total transverse energy of the cluster > 1.5 GeV
- Electromagnetic energy fraction $E_{\text{had}}/E_{\text{total}} > 0.9$
- The tower containing the largest energy (hottest tower) of the cluster must have more than 40% of the cluster energy, i.e. $E_{\text{trans}}/E_{\text{total}} < 0.6$

For each electron or photon candidate.the centroid of the cluster is calculated as a weighted mean of the coordinates of the cluster cells in the third layer of the EM calorimeter:

$$\vec{x}_{\text{clus}} = \frac{\sum_i w_i \vec{x}_i}{w_i \vec{x}_i} \tag{3.1}$$

the weights w_i are defined as:

$$w_i = \max\left(0, w_0 + \ln\left(\frac{E_i}{E}\right)\right) \tag{3.2}$$

where E_i is the energy in the i^{th} cell, E the energy of the cluster and w_0 a parameter chosen to optimize the position resolution. This logarithmic weighing is motivated by the exponential lateral profile of an electromagnetic shower. The weights were found to be η and ϕ dependent and were tuned using test beam data, also, corrections for bias in theta are applied.

To distinguish among electrons and photons, central detector tracks are defined by the cluster centroid and the primary interaction vertex. The road in which tracks are defined covers in azimuth ± 0.1 radians around the cluster position. The road limits in θ are computed as:

$$\tan\theta_{\pm} = \min(\rho_{\text{clus}}/(z_{\text{clus}} - z_{\text{vertex}} \pm 5\delta z), 0.1) \tag{3.3}$$

where $\rho_{\text{clus}} = \sqrt{x^2_{\text{clus}} + y^2_{\text{clus}}}$, x, y, z_{clus} are the coordinates of the cluster centroid, z_{vertex} is the interaction vertex position along the beam direction and δz its error.

A search for a track is performed on this road, if one or more tracks are found the candidate cluster is considered as an electron (PELC bank); otherwise it is taken as a photon (PPHO bank). If the vertex position is not correctly determined the tracking roads are miscalculated and the distinction among electrons and photons can be misleading.

3.2 Standard electron identification

After the reconstruction of electrons and photons there remains a considerable amount of background that contaminates the reconstructed sample. Standard techniques have been developed to identify electrons by introducing additional criteria which allow to reduce the background in the sample while retaining most of the real electrons for further analysis. Following there is a description of each of the standard quantities employed for electron identification.

3.2.1 Electromagnetic energy fraction

By definition, an electromagnetic object is stored in the database if it has a large electromagnetic fraction, that is, that 90% of the total energy of the particle is deposited in the EM layers of the calorimeter. This is a loose requirement for electrons originating in Z decays. Figure 3.1 shows the electromagnetic energy fraction f_{EM} distribution for electrons from $Z \to e^+e^-$ decays and electrons from multijet events, both in the central calorimeter. Further background rejection can be obtained by raising the cut to $f_{\mathrm{EM}} > 0.95$.

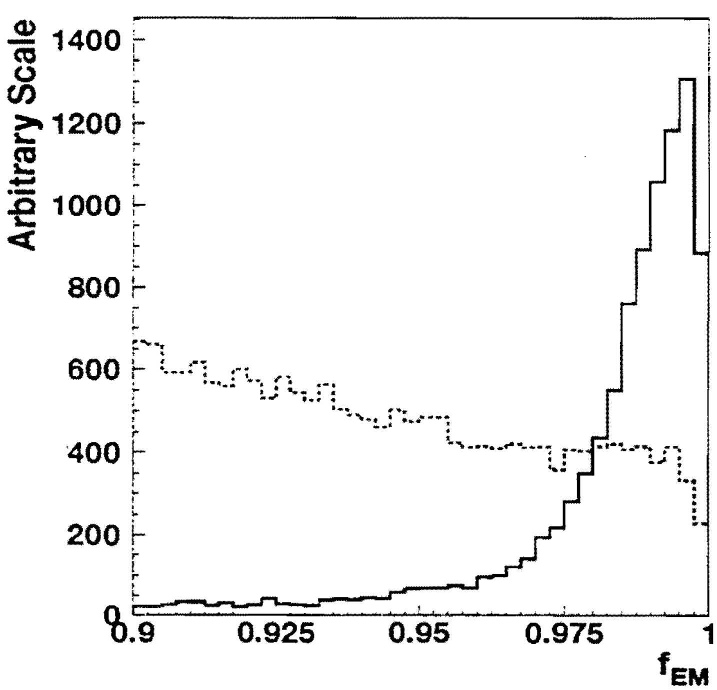

Figure 3.1: EM fraction f_{EM} distribution for electrons from $Z \to e^+e^-$ decays (solid line) compared with the f_{EM} distribution for electrons in multijet triggered data (dashed line) in the central calorimeter.

3.2.2 H-Matrix χ^2

The shower shape may be characterized by the fraction of cluster energy that is deposited in each layer of the calorimeter. These fractions are dependent on the energy of the incident particle and have the inconvenience of being correlated, i.e. a shower which fluctuates and deposits a large fraction of its energy in the first layer of the calorimeter will deposit a smaller fraction in the subsequent layers and viceversa.

To take into account the energy deposited by an electron in a given layer as well as its correlations with the energy deposited in the other layers, we use a covariance matrix (M) of 41 variables x_i to characterize the "*electron-ness*" of the shower. The matrix elements are computed from a reference sample of N Monte Carlo electrons with energies ranging between 10 and 150 GeV. These elements are defined as:

$$M_{ij} = \frac{1}{N}\sum_{i,j=1}^{41}(x_i' - \bar{x}_i)(x_j^n - \bar{x}_j) \tag{3.4}$$

where x_i^n is the value of the i^{th} observable for the n^{th} electron and $\bar{x}_i$ is the mean of the i^{th} observable. The observables are the fractional energies in layers 1, 2, and 4 of the EM calorimeter, and the fractional energy in each cell of a 6×6 array of cells in layer 3 centered on the most energetic tower in the EM cluster. The logarithm of the cluster energy is included as an observable to take into account the dependence of the fractional energy deposits on the cluster energy. Finally, the position of the event vertex along the beam direction is included to take into account the dependence of the electron shower shape on the point from which the electron is originated. There is a total of 37 matrices, one for each of the 37 towers into which half the calorimeter is subdivided in pseudo-rapidity. The other half of the calorimeter with negative z-coordinate is handled using reflexion symmetry.

For a shower, characterized by the observables x_i', the covariance parameter

$$\chi^2 = \sum_{i,j=1}^{41}(x_i' - \bar{x}_i)H_{ij}(x_j^n - \bar{x}_j) \tag{3.5}$$

where $H = M^{-1}$, measures how consistent its shape is with that expected from an EM shower. In general, the values of the observables x_i' are not normally distributed and therefore the covariance parameter χ^2 does not follow a χ^2 distribution.

Since H is a symmetric matrix, it can be diagonalized using an appropriate unitary matrix U, then, χ^2 is given by

$$\chi^2 = yH'y^T \tag{3.6}$$

so that the transformed matrix $H' = U^T HU$ is diagonalized and the components of the vector y are uncorrelated variables. The matrices, as mentioned above, are calculated using Monte Carlo events. Slight differences in shower shapes between Monte Carlo and data can cause large contributions to χ^2 if the eigenvalues of the matrices are unusually large. In order to prevent any component from dominating the value of the covariance variable χ^2, the magnitude of the diagonal elements of H' are limited to a maximum value, which optimizes the electron finding efficiency and rejection power. Figure 3.2 shows the χ^2 distribution for test beam electrons (unshaded), test beam pions (shaded) and electrons from $W \to e\nu$ events (dots).

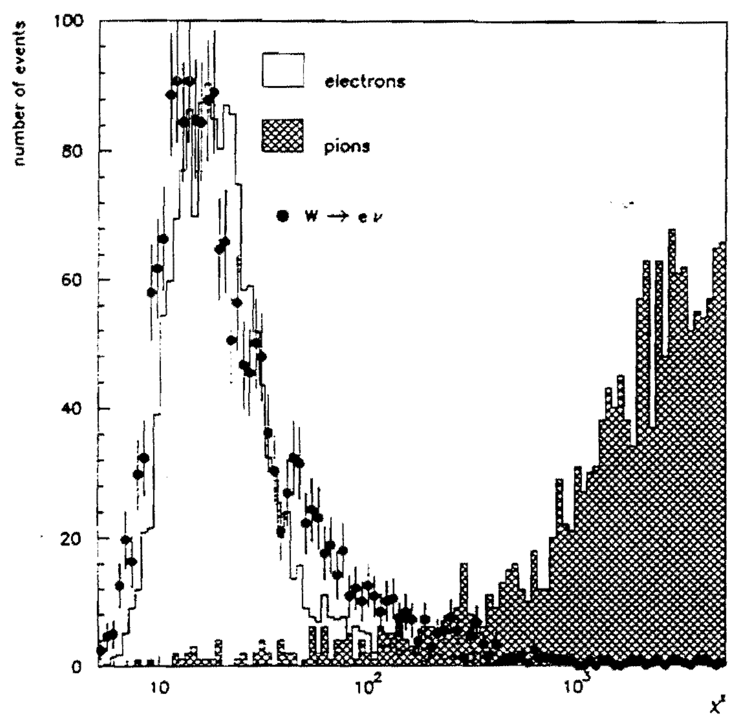

Figure 3.2: χ^2 distribution for test beam electrons (unshaded), test beam pions (shaded) and electrons from $W \to e\nu$ events (dots).

In the present analysis, electron candidates are required to have $\chi^2 < 100$. The effect of this selection cut can be seen in figure 3.3.

3.2.3 Shower isolation

Since the electrons produced by the decay of a Z boson are not produced in association with other particles the calorimeter clusters corresponding to these electrons should appear isolated. Electromagnetic clusters are narrow compared with the clusters produced by hadronic particles, they are usually contained in a cone of radius $\mathcal{R} = 0.2$ in the $\eta - \phi$ space. The variable which allows to quantify the degree of isolation of an

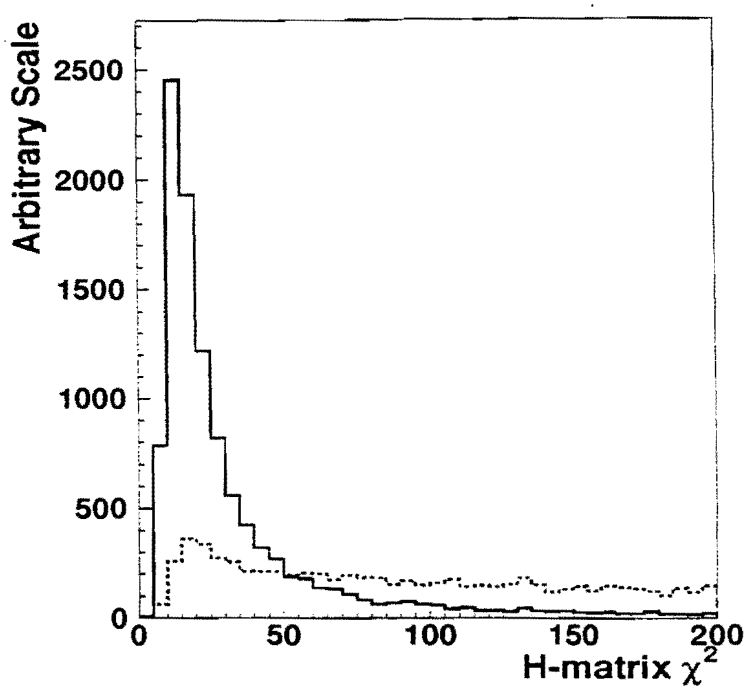

Figure 3.3: χ^2 distribution for electrons from $Z \rightarrow e^+e^-$ decays (solid line) compared with the χ^2 distribution for electrons in multijet triggered data (dashed line) in the central calorimeter.

electromagnetic cluster is defined as:

$$f_{\text{iso}} = \frac{E_{\text{total}}(0.4) - E_{\text{EM}}(0.2)}{E_{\text{EM}}(0.2)} \tag{3.7}$$

where $E_{\text{total}}(0.4)$ is the total energy contained in an isolation cone of radius $\mathcal{R} = 0.4$, and $E_{\text{EM}}(0.2)$ is the electromagnetic energy in a core cone of radius $\mathcal{R} = 0.2$. In the present analysis a requirement of $f_{\text{iso}} < 0.15$ is imposed to the electron candidates. Figure 3.4 shows the distribution of f_{iso} for electrons from $Z \rightarrow e^+e^-$ decays.

3.2.4 Track matching

The ionization trail in the drift chamber from real electrons is expected to be aligned with the respective shower in the calorimeter, hence, the use of more stringent track-cluster matching criteria than the employed by the reconstruction package can further reduce background from the candidate sample, as well as further discriminate between electrons and photons.

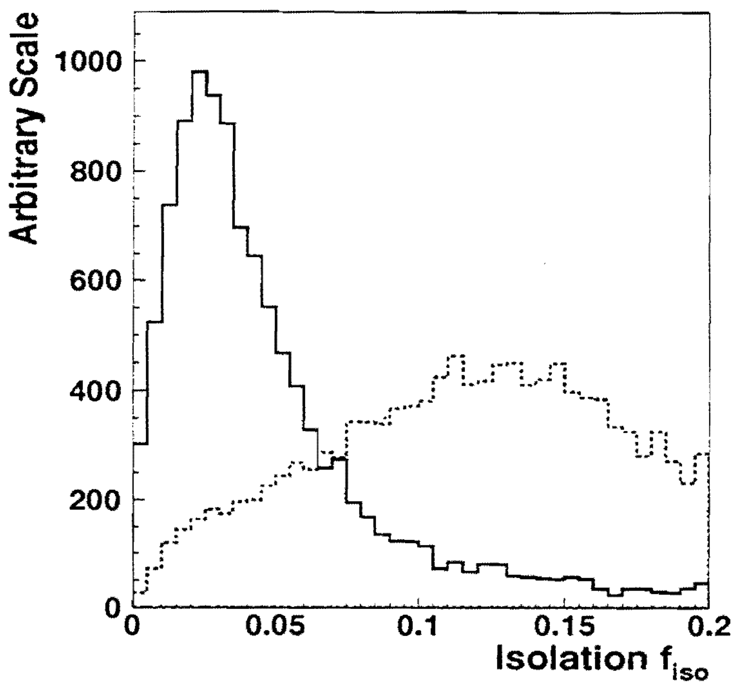

Figure 3.4: Isolation fraction f_{iso} distribution for electrons from $Z \to e^+e^-$ decays (solid line) compared with the f_{iso} distribution for electrons in multijet triggered data (dashed line) in the central calorimeter.

In order to quantify the matching between a track and its corresponding calorimeter cluster, the track is extrapolated into the EM3 layer of the calorimeter and the distance between the resulting projection and the cluster centroid position is calculated. The resolutions achieved in matching the track projection and the cluster centroid are shown in figure 3.5 [25]. For central electrons, the track cluster difference distribution has a longitudinal width of approximately 1.7 cm, and a transverse width of 0.3 cm. For electrons in the forward region, the resolutions are 0.7 cm and 0.3 cm respectively. Using these resolution it is possible to construct a discriminant similar to the H-Matrix χ^2 discussed above. This variable, called "track match significance" is defined for the central calorimeter as:

$$S_{\text{trk}}^{CC} = \sqrt{\left(\frac{\rho\Delta\phi}{\sigma_{\rho\phi}}\right)^2 + \left(\frac{\Delta z}{\sigma_z}\right)^2} \tag{3.8}$$

where $\rho\Delta\phi$ is the transverse spatial mismatch, Δz is the longitudinal spatial mismatch and $\sigma_{\rho\phi}$ and σ_z are the corresponding resolutions. Similarly for the forward region, the track match significance is defined as:

$$S_{\mathrm{trk}}^{EC} = \sqrt{\left(\frac{\rho\Delta\phi}{\sigma_{\rho\phi}}\right)^2 + \left(\frac{\Delta\rho}{\sigma_\rho}\right)^2} \tag{3.9}$$

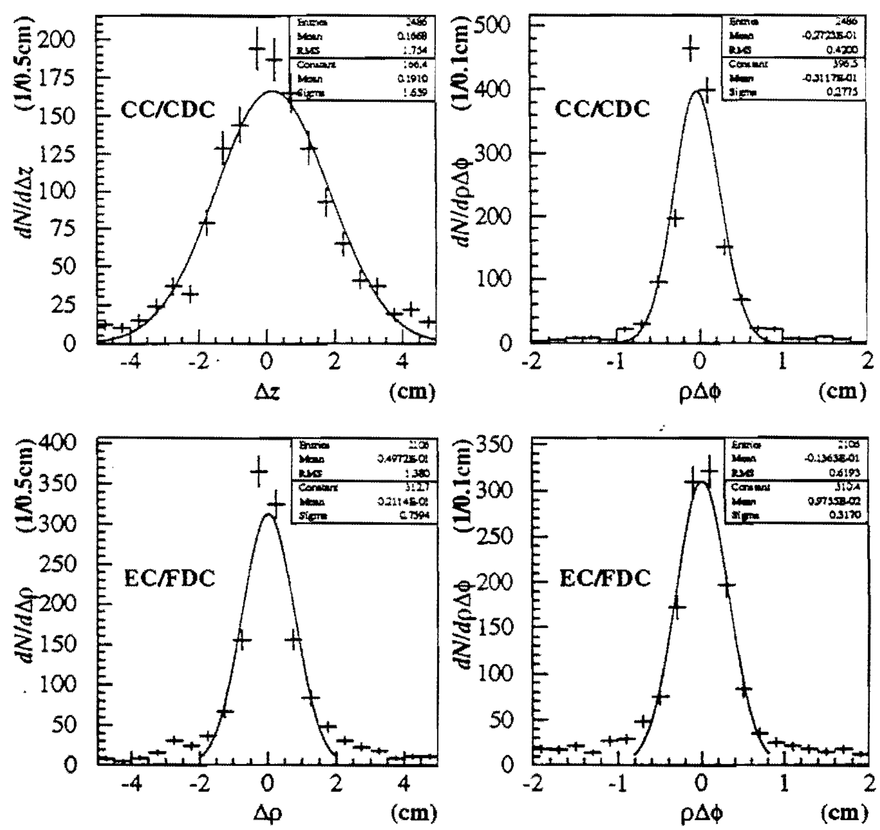

Figure 3.5: Differences in cluster and projected track positions for $Z \to e^+e^-$ candidates. Only events with $S_{\mathrm{trk}} < 30$ are shown [25, p. 80].

To clarify the definition of the track match significance we can see in figure 3.6 that track projections which fall within the indicated significance ellipse projected onto the surface of the EM3 layer are considered as good matches.

Figure 3.7 shows the distribution of the S_{trk} variable for electrons from $Z \to e^+e^-$ decays (solid line) and for electrons in multijet triggered data (dashed line) in the central calorimeter. In this analysis a track match significance requirement of $S_{\mathrm{trk}} < 5$ was imposed to electrons in the central region, while a requirement of $S_{\mathrm{trk}} < 10$ was imposed to electrons in the forward region

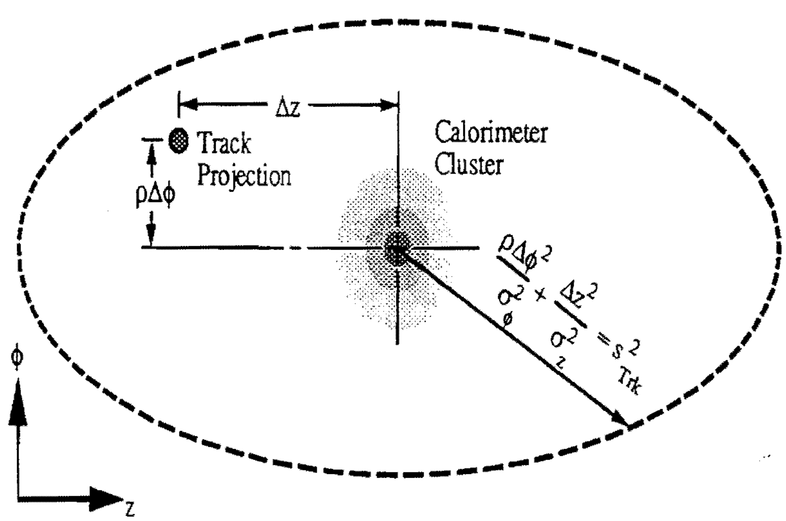

Figure 3.6: Definition of the track match significance in terms of the cluster centroid an EM3 and the projection of the track to this radius [25, p. 81].

3.3 Improvements to the standard electron identification

In the previous section, the standard DØ electron identification criteria were described, however, in order to increase the selection efficiency, it is necessary to introduce some improvements to these selection criteria.

A major improvement was the introduction of a new electron vertex finding method by Steven Glenn [25, sec. 4.8.1]; since a mismeasurement of the vertex position leads to an incorrect definition of the tracking road, which can lead to an incorrect tagging of electrons and photons. In addition, several kinematic quantities, and a correct determination of the angular position of the particles rely on a good identification of the primary vertex.

The method described in the following section attempts to improve the identification of the primary vertex by using electron information.

3.3.1 Electron vertex finding method

As explained in section 3.1, the distinction between electrons and photons is based on whether or not there is a track contained in the tracking road. Any mismeasurement of the vertex position can lead to an incorrect definition of the road and thus, to misidentification of electrons and photons.

The method described below, uses the track that best matches the cluster, regardless if the track is or not on the road previously described. This track can be used to

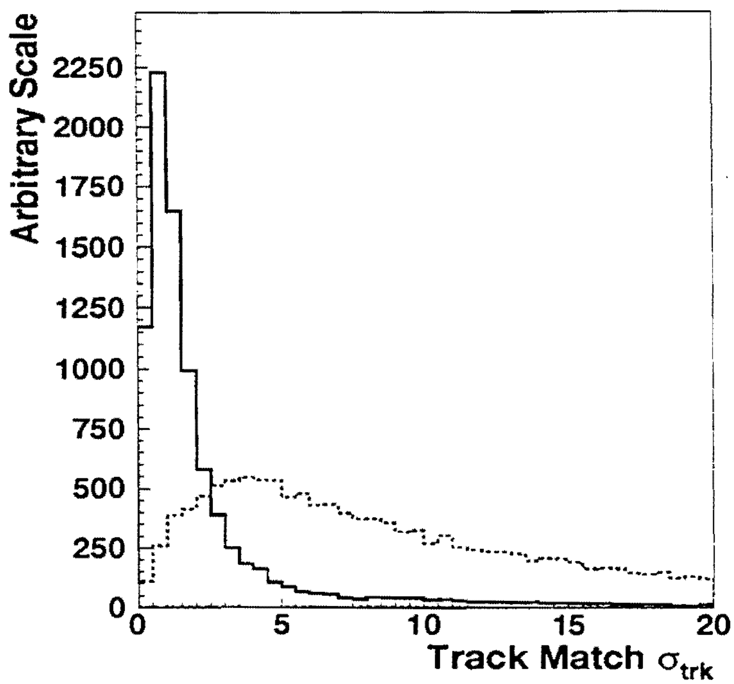

Figure 3.7: EM fraction S_{trk} distribution for electrons from $Z \to e^+e^-$ decays (solid line) compared with the S_{trk} distribution for electrons in multijet triggered data (dashed line) in the central calorimeter.

unambiguously determine where the electron originated by extrapolating the line connecting the calorimeter cluster centroid and the drift chamber[1] hits center of gravity, to the beamline.

The z vertex position, denoted z_v is given by:

$$z_v = z_0^{\mathrm{trk}} - \left(\frac{z_0^{\mathrm{cal}} - z_0^{\mathrm{trk}}}{\rho_0^{\mathrm{cal}} - \rho_0^{\mathrm{trk}}} \right) \rho_0^{\mathrm{trk}} \tag{3.10}$$

where $(z_0^{\mathrm{trk}}, \rho_0^{\mathrm{trk}})$ and $(z_0^{\mathrm{cal}}, \rho_0^{\mathrm{cal}})$ are the centroid positions of the drift chamber and calorimeter hits, respectively.[2] The extrapolation is shown schematically in figure 3.8.

The vertex resolution achieved by this technique can be measured from $Z \to e^+e^-$ events, since it is proportional to the difference between the z-intercepts of the two

[1]Only tracks from the CDC and FDC are considered, since the tracks from the vertex chamber were fit using the vertex position found by the standard reconstruction program.

[2]For FDC tracks, z_0 and ρ_0 are more properly regarded as track parameters than hit centroids since the z_0 position is fixed at $\pm$105.3 cm for the FDC track reconstruction.

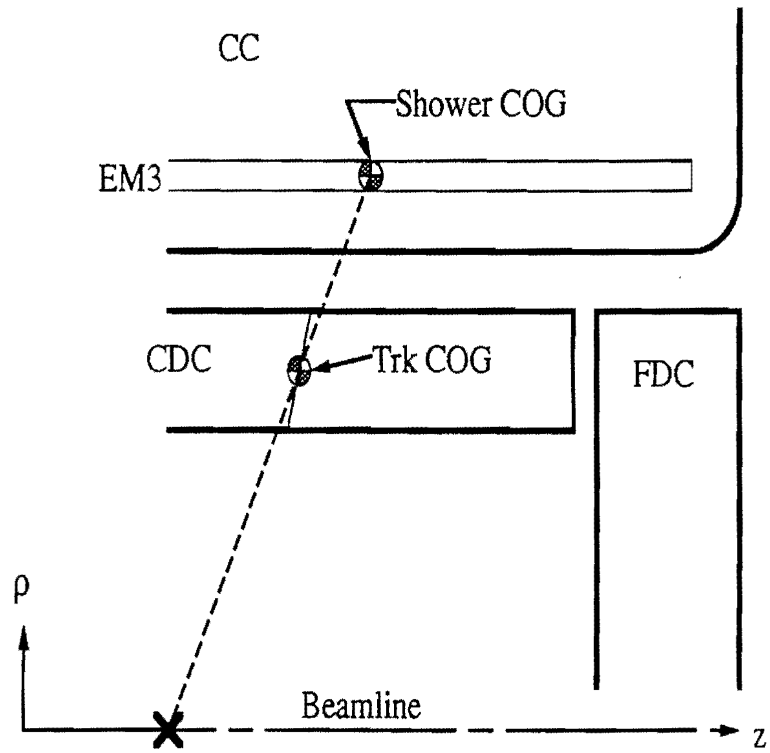

Figure 3.8: Vertex determination by cluster-track projection method [25, p. 84].

electrons; the single vertex resolution, σ_z is given by:

$$\sigma_z = \frac{1}{\sqrt{2}}\sigma(z_1 - z_2) \tag{3.11}$$

if the z-intercepts of the two electrons are uncorrelated. σ_z was found to be $\sigma_z = 2.0$ cm [25] for either central or forward electrons.

3.3.2 Performance of the electron vertex finding method

Given the single vertex resolution, it is possible to quantify the frequency at which DØRECO mismeasures the primary vertex position. The standard vertex is considered mismeasured if it is at least 5 standard deviations from the single electron vertex (approximately a distance of 10 cm). Figure 3.9 (a) shows the rate at which standard vertex is mismeasured in $Z \to e^+e^-$ events, where the event vertex was calculated only from the electron with the centralmost electron. For the inclusive Z sample, about 13% of the events have mismeasured primary vertices [25]. In contrast, the rate at which $(z_1 - z_2) > 10$ cm is relatively flat as a function of the instantaneous luminosity, indicating that the algorithm is quite robust.

The invariant mass spectrum in figure 3.9 (b) shows that the electron vertex algorithm increases the number of events in the central peak region. The broader mass distribution of the standard vertexing algorithm is caused by misreconstructed vertices which lead to a misdetermination of the invariant mass.

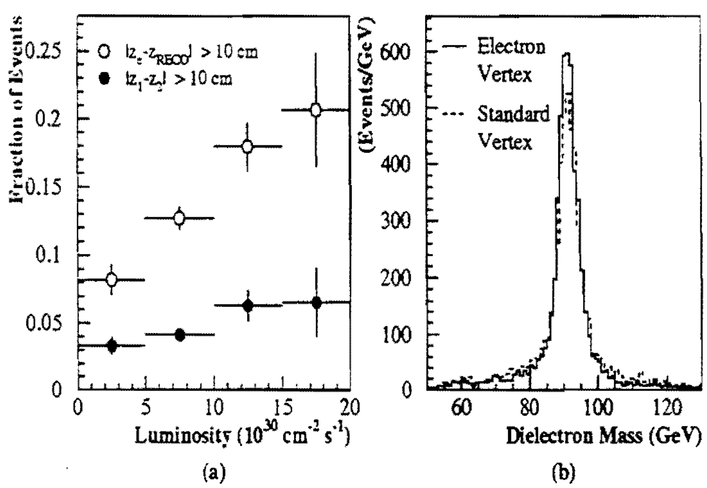

Figure 3.9: (a) Frequency at which the electron vertex is found more than 10 cm from the standard (DØRECO) vertex. Also shown is the rate at which the electron track z intercepts differ by more than 10 cm. (b) Invariant mass distribution for $Z \to e^+e^-$ candidate events using the two vertexing schemes [25, p. 86].

3.4 Z event sample

The data sample used in this analysis was selected from the 1994-1995 Tevatron collider Run 1b, corresponding to 97.18 ($\pm$ 5.3%) pb^{-1} total integrated luminosity ($\mathcal{L}$). The final data set corresponds to the streamed μDST [27] sample from the WZ group. The stream was done with events reconstructed using DØRECO versions 12.13 through 12.21; each event of the stream was required to pass at least on of a set of relevant Level 2 filters and have at least two electromagnetic objects with $E_T > 10$ GeV. The stream was then made into ntuples for the QCDWZ group[3][28]. At the ntuple making stage further processing occurred: standard DØ packages were used and events which belong to runs with known detector problems were rejected[4].

[3]For this analysis we used version 10 of the QCDWZ ntuples
[4]Only problems with tracking or calorimetry were considered.

The final Z sample was selected using the EM2_EIS2_HI Level 2 filter. This filter has the following conditions:

- Level 0 trigger
  - The Level 0 minimum bias requirement was imposed during the data taking period.
- Level 1 trigger
  - 2 electromagnetic objects with $E_T > 7.0$ GeV;
  - MAXLIVE beam veto: events occurring in the MRBS_LOSS and MICRO_BLANK periods simultaneously were rejected.
- Level 1.5 trigger
  - 2 electromagnetic objects with $E_T > 12.0$ GeV;
  - 2 electromagnetic objects with EM fraction > 0.85
- Level 2 filter
  - 2 electromagnetic objects with $E_T > 20$ GeV;
  - Loose shower shape and isolation fraction cut on both objects.

The offline selection of the final sample imposed in addition the following requirements:

- Both electrons should be within the good fiducial region, i.e.:
  - Central calorimeter (CC):
    $|\eta_{\rm det}| < 1.1$ and $0.05 < \mathrm{MOD}\,(32\phi_e/2\pi, 1.) < 0.95$
  - End calorimeter (EC):
    $1.5 < |\eta_{\rm det}| < 2.5$
- EM fraction ≥ 0.95,
- H matrix $\chi^2 \leq 100$,
- Isolation fraction ≤ 0.15

all these cuts define what is called a "loose electron", a loose electron with the additional requirement of:

- $S_{\rm trk} < 5$ (10) in the CC (EC)

becomes a "tight electron". The final Z sample was selected requiring a pair of electrons, at least one of which must be tight.

The z-coordinate of the vertex of the event must have $|z| < 96.875$. The vertex of the event is defined by the vertex of the tight electron, or if both electrons are tight, the vertex of the centralmost electron, defines the vertex of the event.

Finally, the invariant mass of the pair of electrons must be within the range $75 < M_{ee} < 105$ GeV/c^2. Table 3.1 shows a summary of the final number of events we accepted in each different combination of cryostats. Figure 3.10 shows the invariant mass distributions for the different contributions from the cryostats.

	CC-CC	CC-EC	EC-EC	Total
Number of events	3200	2534	601	6635

Table 3.1: Number of candidate events in the invariant mass region $75 \leq M(ee) \leq 105$ GeV/c^2.

Figure 3.11 shows the raw longitudinal momentum distributions x_Z, x_1 and x_2 calculated using formulas (1.17) and(1.23). The following chapters are dedicated to calculate the necessary corrections that shall be applied to these distributions in order to compare them with the theoretical predictions.

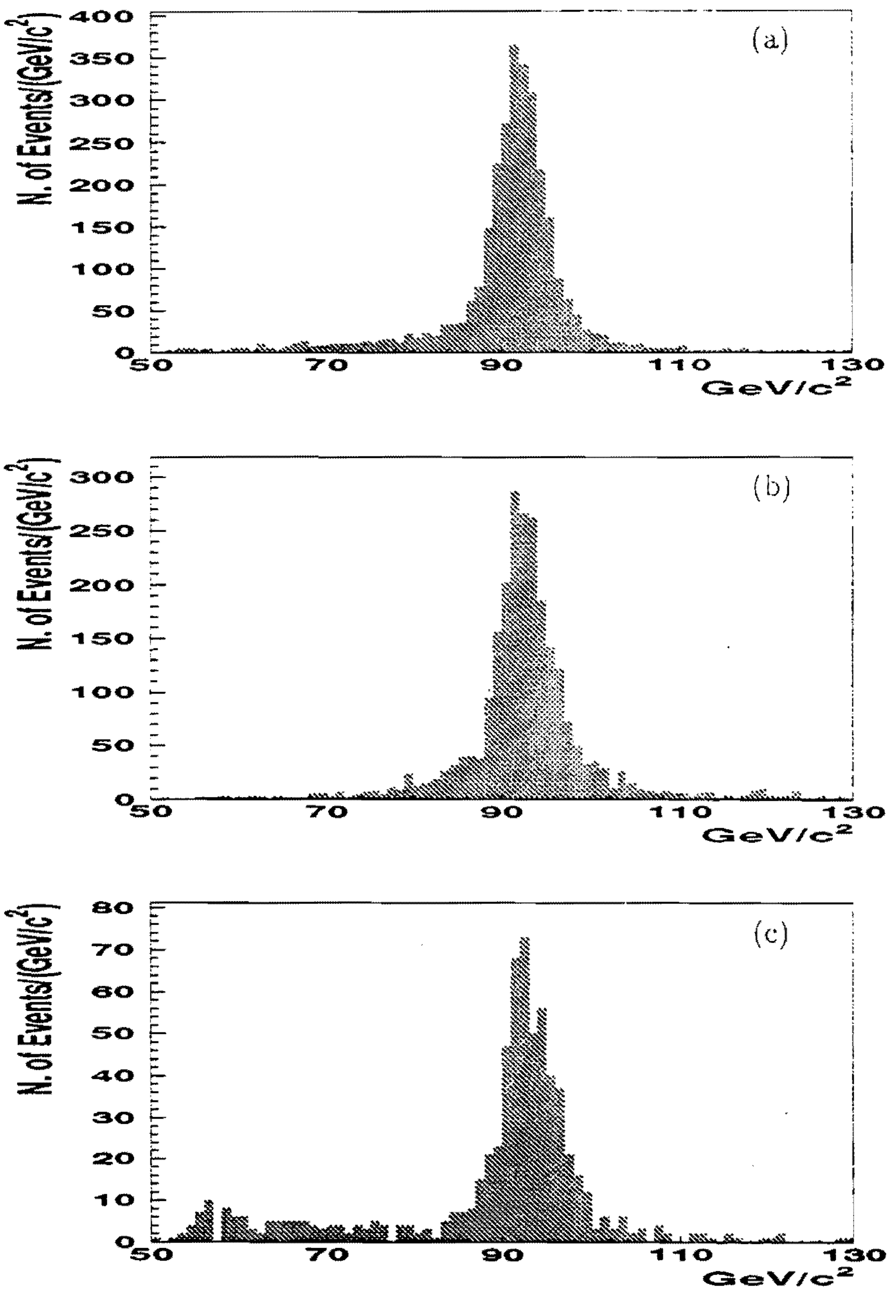

Figure 3.10: e^+e^- data invariant mass distributions. a) For CC-CC electrons, b) for CC-EC electrons and c) for EC-EC electrons.

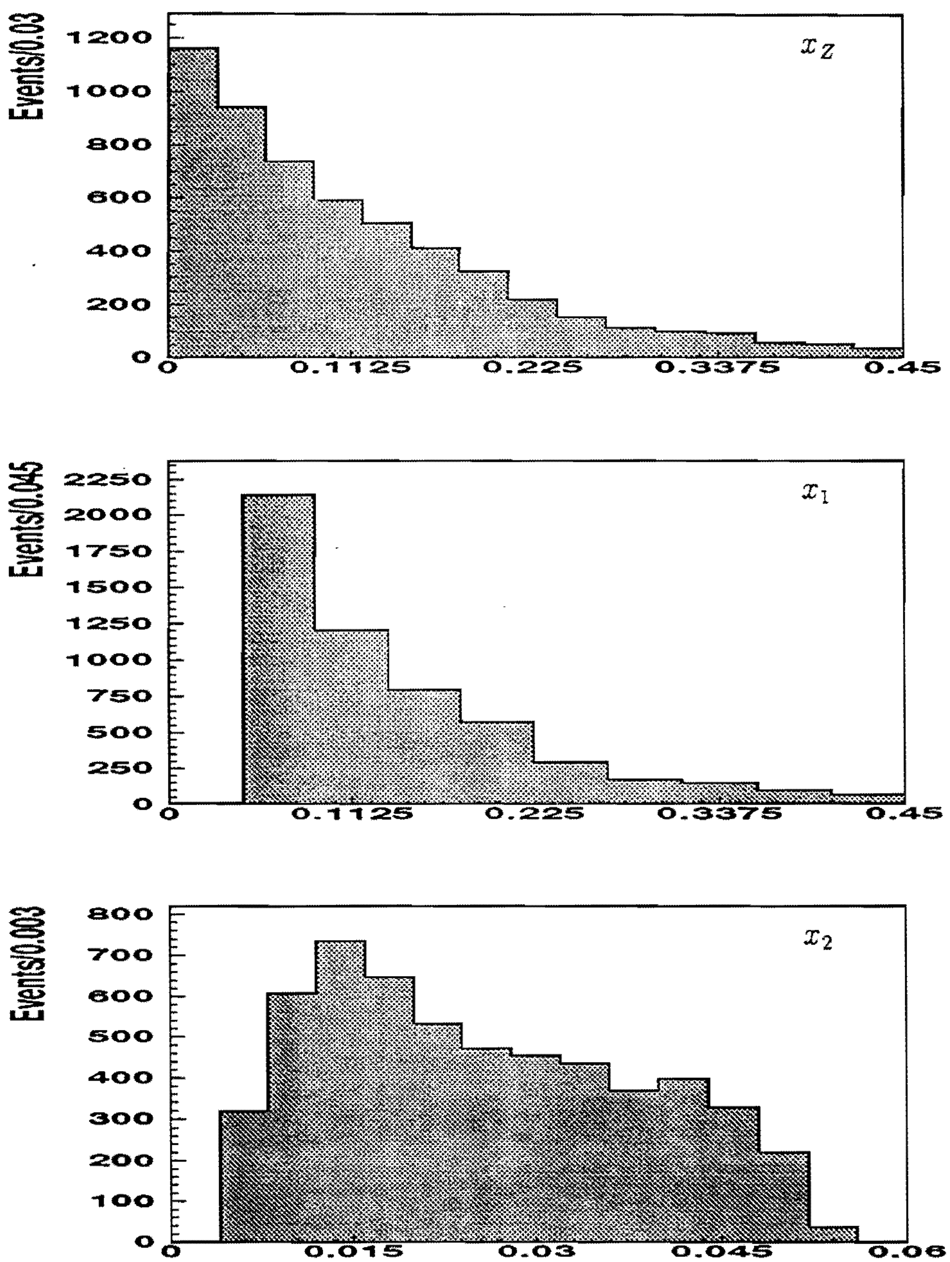

Figure 3.11: x_Z, x_1 and x_2 raw distributions.

Chapter 4

Event generators and detector simulation

True, I talk of dreams
which are the children of an idle brain
begot of nothing but vain fantasy

Shakespeare (Romeo and Juliet Sc. 4).

In order to estimate the amount of background that contaminates the data sample, the systematic errors introduced by the measuring process, the accepatnce of the detector and the effciency of the data selection, one has to rely on computer simulations of the physics processess under study as well as the detector effects.

There are several accurate event generators which simulate the physics processess ina reasonable ammount of time, however, a detailed detector simulation (like GEANT [47]) requires a big amount of computing resources. For this reason, high energy physics experimentalists rely in the use of fast, less detailed simulations of the experimental equipment called Fast Monte Carlos. In this chapter it is presented a description of the features of the MC simulations used in the analysis.

4.1 ISAJET MC sample

ISAJET [30] is a MC program which simulates $p\bar{p}$ interactions at high energies based on perturbative QCD and phenomenological models for parton and beam jet fragmentation.

The ISAJET sample used in this study was generated with ISAJET version 6.49. The parameters used to generate the events are summarized in table 4.1

The simulation of the detector was based on the GEANT program, which is a program that describes the passage of elementary particles through matter allowing

Event type	$Z \to ee$
W mass	80.14
Z mass	91.175
$\sin^2 \theta_W$	0.2274
Λ_{QCD}	0.2
IVB P_t	0.1, 200
t-quark mass	140
Higgs mass	0
η range	$\lvert\eta\rvert < 3.5$
Decay	e, e
Structure function	EHLQ

Table 4.1: Parameters used to generate the ISAJET MC events in the analysis.

for a detailed tracking description, as well as shower development for a given geometry of the detector system.

The events were reconstructed using the same reconstruction package as the data, (DØreco version 11.19). The files used in this study have the generic name:

WZX_ZEEX*_IS649_G314SS0A_*.X_DST01REU1119_ALL00_NONEX00_*

The MC sample was selected using the same selection criteria used to select the data.

4.2 NYU Fast MC

Several samples of Fast MC generated events, generated with the NYU Fast Monte Carlo [29], were used in the present analysis. The NYU Fast MC is a fast executing program which generates final state particles of a physics process (W and Z boson production and electronic decay) and smears the measurable quantities according to the resolution of the DØ detector. The NLO double differential cross section $d^2\sigma/(dp_T dy)$ of the vector boson is introduced as an input to the program. The mass of the intermediate vector boson is generated with a relativistic Breit-Wigner line shape. The decays of the polarized Z bosons are generated in the rest frame of the boson, and the decay products are then boosted to the laboratory frame and traced to the detector simulation with the appropriate resolution smearing. For a more detailed description of this MC see [10].

The program allows the user to select the *Physics* parameters such as the structure function, the Z-width, the Z-mass, etc; and the *detector* parameters, such as the EM and HAD energy resolutions, position and angular resolutions, the position of the vertex etc.

Physics parameters	
Z width	2.4974
Z mass	87.0
Parton distribution function	MRSD-'
Detector parameters	
Constant term of CC EM resolution	0.015
Sampling term of CC EM resolution	0.13
Shift of the vertex position w/r to nominal	0.0

Table 4.2: Default values of the input parameters of the NYU Fast MC.

Several sets of samples were generated varying one physics parameter or one detector parameter at a time. The input parameters used to generate each Fast MC sample will be described in the particular section where the sample is used. Table 4.2 shows the default values of these parameters.

4.3 CMS Fast MC

The CMS (Columbia-Michigan State) Monte Carlo had its origin in the NYU Monte Carlo, but it was designed to be fast and easily modifiable and it presents significant modifications due to the luminosity dependences found in Run 1b as well as general improvements in the algorithm. Although it is possible to generate W and Z events with CMS, the following description is focused on the detailes involved in the generation of Z events. For a more detailed description of CMS see [31, 32].

4.3.1 Vector boson production

The model implemented for the production of vector bosons assumes that the differential cross section can be factorized as:

$$\frac{d^3\sigma}{dydp_Tdm} = \frac{d^2\sigma}{dydp_T} \cdot \frac{d\sigma}{dm} \tag{4.1}$$

The rapidity and transverse momentum of the vector boson are selected from the $d^2\sigma(p\bar{p} \to Z)/dydp_T$ calculated by Ladinsky and Yuan [48], for a fraction f_{ss} of events, it is used a $d^2\sigma(p\bar{p} \to Z)/dydp_T$ calculated for two sea quarks.

The mass spectrum of the boson is then selected from a relativistic Breit-Wigner line shape, modified by a function called parton luminosity, in the following way:

$$\frac{d\sigma}{dm} = \frac{e^{-\beta m}}{m} \cdot \frac{m^2}{(m^2 - M_Z^2)^2 + \frac{m^4\Gamma_Z^2}{M_Z^2}} \tag{4.2}$$

The parton luminosity term ocurs because the momentum distribution of the quarks makes it more probable that a particule with mass of 60 GeV/c^2 will be produced than a particle with a mass of 90 GeV/c^2 [31].

pdf	β (GeV^{-1})	f_{ss}
MRSA$'$	3.6×10^{-3}	0.207
CTEQ3M	3.3×10^{-3}	0.203
CTEQ2M	—	0.203
MRSD$-'$	3.8×10^{-3}	0.201

Table 4.3: Parton luminosity slope β and fraction of sea-sea interactions f_{ss} in the Z production model. The β value is given for $Z \to ee$ decays with both electrons in CC.

To evaluate the slope β of the parton luminosity a sample of Z events is generated using the HERWIG Monte Carlo event generator [33] interfaced with PDFLIB [34], the events are selected with the same kinematic and fiducial ccuts as the Z data sample with all the electrons in the CC. The spectrum is divided by the intrinsic lineshape of the boson and the result is proportional to the parton luminosity. Table 4.3 shows the values of β and f_{ss} used in the Z production model for several parton distribution functions.

The vertex of the event is generated according to a gaussian with mean at $z = 0$ cm and RMS = 25 cm as observed in the data. The luminosity of the event is picked from the histogram in figure 4.1. At this stage, the kinematics of the vector boson are completly defined.

The boson is then decayed into leptons in its rest frame, the azimuthal angular distribution of the leptons is generated taking into account the kind of quark (see-valence) that produced the boson, according to the relation [10]:

$$\frac{d\sigma}{d\cos\theta^*} \propto (1+\cos\theta^*)^2 \tag{4.3}$$

where θ^* is the angle between the charged lepton and the proton beam direction in the boson rest frame. The polar distribution is uniformly generated from 0 to 2π. The leptons are then boosted into the lab frame using the four vector of the generated boson.

The radiative process $Z \to e^+e^-e\gamma$ is simulated according to the calculation by Berends and Kleis [49], which gives the fraction of events in which a photon with energy $E(\gamma) > E_0$ is radiated, the angular distribution and energy spectrum of the photons. The minimum energy used is $E_0 = 50$ MeV, so there is a 66% probability that any one of the electrons from $Z \to ee$ radiates a photon with $E(\gamma) > E_0$.

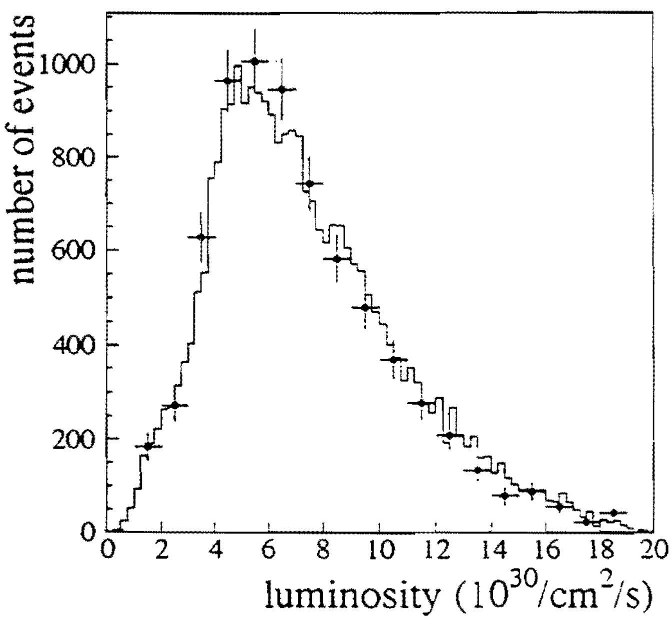

Figure 4.1: The luminosity distribution of the W (−) and the Z (•) data samples.

4.3.2 Detector simulation

A useful feature of CMS is that the user can simulate the detector effects on events generated with other MC programs (such as PYTHIA [44]) getting rid of the CMS own event generator described above.

CMS detector simulation uses a parametrized model for the response and resolution to obtain a prediction of the observed spectra. The detector effects simulated by CMS are: the electromagnetic energy and angular resolutions, hadronic momentum resolution, the efficiencies, the acceptance and small corrections to the electron and recoil momentum vectors. Resolutions and efficiencies used in the MC are measured from data. In the following sections only the effects simulated by CMS directly related related with the present analysis will be discused. For a discussion of the corrections related with the hadronic response and resolution see reference [31].

4.3.2.1 Angular resolution

Since the polar angle of an electron is reconstructed from the center of gravity of the electron cluster in the calorimeter and the center of gravity of the tracks in the CDC (FDC), the resolution associated with these points is translated into the resolution of the polar angle.

From a Monte Carlo study it was found that the resolution of the shower centroid in the calorimeter can be parametrized as [31]:

$$\sigma(\theta', z) = (a + b \cdot \theta') + (c + d \cdot \theta') \cdot |z| \tag{4.4}$$

where z is the position of the shower centroid in the calorimeter and θ' is the angle of incidence with respect to the normal.

In the central calorimeter the resolution varies from 0.4 to 1.1 cm and in the forward calorimeter the radial position resolution is 0.2 cm. The resolution on the azimuthal angle of the cluster in the calorimeter is approximately 3×10^{-3} rad.

The resolution of the center of gravity of the track in the CDC was found to be well modeled by a double gaussian distribution. The resolution of the gaussians are 0.31 cm and 1.56 cm.

Both electrons from the Z decay originate from the same interaction vertex, therefore, the difference between the reconstructed vertexes from the two electrons separately constitutes a measurement of the resolution with which both electrons point to same vertex. Figure 4.2 shows the $z_{vtx}(e_1) - z_{vtx}(e_2)$ distribution observed in the data compared with the CMS simulated distribution.

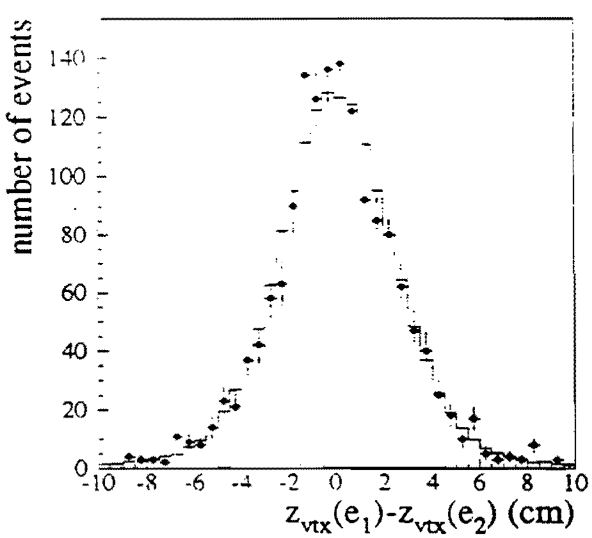

Figure 4.2: The distribution of $z_{vtx}(e_1) - z_{vtx}(e_2)$ for the $Z \to ee$ sample ($\bullet$) and the fast Monte Carlo simulation (-).

4.3.2.2 Electromagnetic energy resolution

The electromagnetic energy resolution in the calorimeter is parametrized as follows:

$$\frac{\sigma_E}{E} = C \cdot E + S \cdot \sqrt{E_T} \tag{4.5}$$

Transverse energy E_T rather than E is used in the sampling term of the central calorimeter because the energy resolution should worsen as the thickness of the sampling unit increases at large angles. Replacing the usual E with E_T compensates for this and allows the coefficient S to remain constant over the entire central calorimeter.

The intrinsic resolution of the calorimeter is given by the sampling term S, which was measured using test beam data [35], and are assumed to be exact. Table 4.4 summarizes the values of the resolution parameters.

Parameter	Central calorimeter	Forward calorimeter
C	0.014 ± 0.002	$0.00^{+0.01}_{-0.00}$
S	$13.5\ \%\ \sqrt{\text{GeV}}$	$15.7\ \%\ \sqrt{\text{GeV}}$

Table 4.4: Parameters used to simulate the electromagnetic energy resolution in the calorimeter with the CMS Monte Carlo.

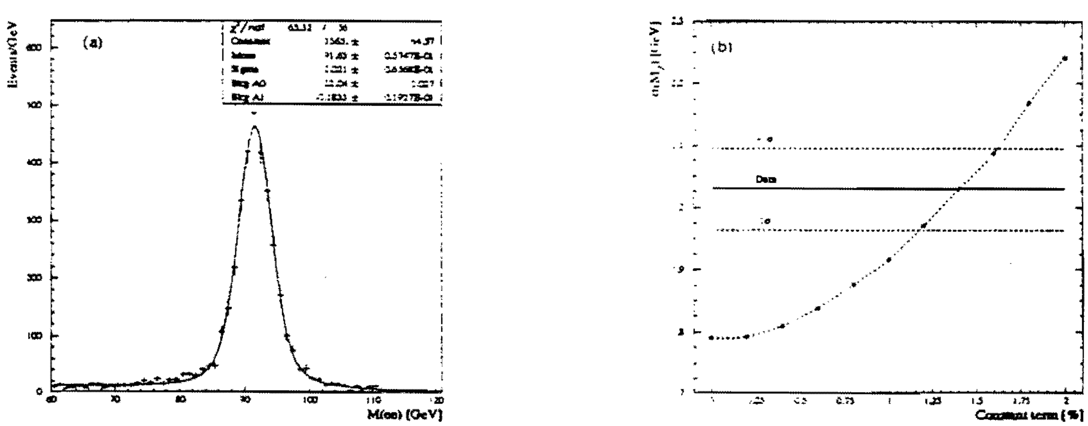

Figure 4.3: (a) Simple Breit-Wigner convoluted with a gaussian resolution fit to the central $Z \to ee$ invariant mass spectrum. (b) Predicted $\sigma(M_{ee})$ vs C for data (line) and Monte Carlo (points) for central electrons. [26, p. 123.]

The constant term C is determined from the width of the invariant mass distribution, $\sigma(M_{ee})$) from $Z \to ee$ events as shown in figure 4.3(a). The constant term is varied in the Monte Carlo until the best fit to the invariant mass distribution in the data is obtained (see figure 4.3(b)).

4.3.2.3 Electron energy response

The reconstructed electron energy and the recorded calorimeter signal are related by:

$$E = A\sum_{i=1}^{5} s_i a_i - \delta_{EM} \tag{4.6}$$

where a_i are the signals observed in each EM layer of the calorimeter (i=1,...4) and the first FH layer (i=5) of a calorimeter tower, s_i is a layer dependent weight, and A and δ_{EM} are two calibration constants to minimize the difference between the reconstructed energy and the measured momentum. By arbitrarily normalizing $s_3 = 1$ the other constants are obtained by minimizing:

$$\chi^2 = \sum_E \sum_{i=1}^{5} \left(\frac{p_i - E_i}{\sigma_E}\right) \tag{4.7}$$

where p_i is the electron momentum, E_i is the energy calculated from equation 4.6 and σ_E is the resolution for energy point E. The parameters for the best fit are summarized in table 4.5.

Parameter	Value
s_1	1.31
s_2	0.85
s_3	1.0
s_4	0.98
s_5	1.84
A	2.96 MeV/ADC count
δ_{EM}	-347 MeV

Table 4.5: Sampling fractions of the calorimeter determined from test beam data. [35]

Figure 4.4 shows the fractional deviation of E as a function of p_{beam}. Above 10 GeV they deviate by less than 0.3% from each other.

The CMS Monte Carlo predicts a reconstructed electron energy:

$$E(e) = \alpha_{\mathrm{EM}} E_0 = A\sum_{i=1}^{5} s_i a_i - \delta_{EM} \tag{4.8}$$

where the constants α_{EM} and δ_{EM} must be determined, since the test beam setup was different from the actual collider running conditions. For that purpose, data from

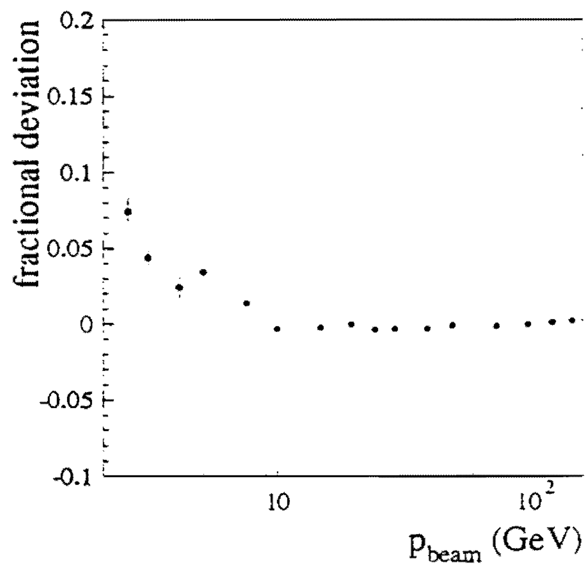

Figure 4.4: The fractional deviation of the reconstructed electron energy from the beam momentum from beam tests of a CC-EM module.

$\pi^0 \rightarrow \gamma\gamma$, $J/\psi \rightarrow e^+e^-$ and $Z \rightarrow e^+e^-$ decays are compared with the Monte Carlo predictions as a function of α_{EM} and δ_{EM}. By minimizing

$$\chi^2 = \sum_i \left(\frac{m_i^{obs} - m_i^{MC}}{\delta m_i^{obs}} \right) \tag{4.9}$$

the best α_{EM} and δ_{EM} is obtained for each data set.

$\pi^0 \rightarrow \gamma\gamma$

The photons from the π^0 decay can not be separated in the calorimeter if the π^0 had a $p_T > 1$ GeV, however. there is a 10% probability for each photon to convert into an e^+e^- pair in the material in front of the CDC. If both photons convert, the tracks from the $\pi^0 \rightarrow e^+e^-e^+e^-$ can be used to determine the opening angle between the two photons. The energy of the π^0 ($E(\pi^0)$) is defined by the energy of the cluster with four tracks pointing towards it. The symmetric mass[1] is defined as:

$$m_{\rm sym} = \sqrt{\frac{1}{2}E(\pi^0)(1 - \cos\gamma)} \quad (4.10)$$

where γ is the opening angle between the converted photons. A Monte Carlo was written to determine the mass of the π^0 from the symmetric mass as a function of α_{EM} and δ_{EM} [31]. Figure 4.5 shows the background subtracted symmetric mass distribution and the Monte Carlo fit. Since the mass is a function of α_{EM} and δ_{EM} these two quantities are correlated.

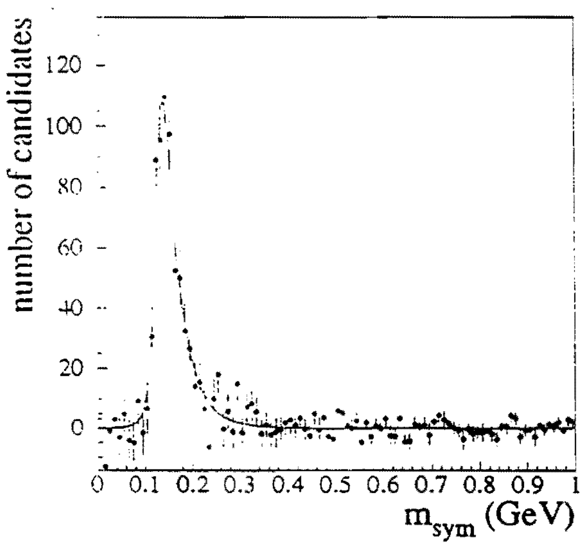

Figure 4.5: The background subtracted m_{sym} distribution. The superimposed curve shows the Monte Carlo simulation.

[1]The symmetric mass is equal to the invariant mass if the decay was symmetric and larger for asymmetric decays.

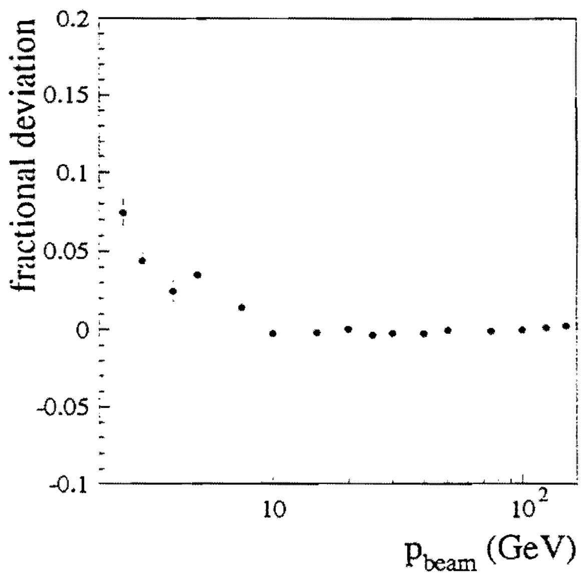

Figure 4.4: The fractional deviation of the reconstructed electron energy from the beam momentum from beam tests of a CC-EM module.

The CMS Monte Carlo predicts a reconstructed electron energy:

$$E(e) = \alpha_{\rm EM} E_0 = A \sum_{i=1}^{5} s_i a_i - \delta_{EM} \tag{4.8}$$

where the constants α_{EM} and δ_{EM} must be determined, since the test beam setup was different from the actual collider running conditions. For that purpose, data from $\pi^0 \to \gamma\gamma$, $J/\psi \to e^+e^-$ and $Z \to e^+e^-$ decays are compared with the Monte Carlo predictions as a function of α_{EM} and δ_{EM}. By minimizing

$$\chi^2 = \sum_i \left(\frac{m_i^{\rm obs} - m_i^{\rm MC}}{\delta m_i^{\rm obs}} \right) \tag{4.9}$$

the best α_{EM} and δ_{EM} is obtained for each data set.

$\pi^0 \to \gamma\gamma$

The photons from the π^0 decay can not be separated in the calorimeter if the π^0 had a $p_T > 1$ GeV, however, there is a 10% probability for each photon to convert into an e^+e^- pair in the material in front of the CDC. If both photons convert, the tracks from the $\pi^0 \to e^+e^-e^+e^-$ can be used to determine the opening angle between the two photons. The energy of the π^0 ($E(\pi^0)$) is defined by the energy of the cluster with four tracks pointing towards it. The symmetric mass[1] is defined as:

$$m_{\text{sym}} = \sqrt{\frac{1}{2}E(\pi^0)(1 - \cos\gamma)} \tag{4.10}$$

where γ is the opening angle between the converted photons. A Monte Carlo was written to determine the mass of the π^0 from the symmetric mass as a function of α_{EM} and δ_{EM} [31]. Figure 4.5 shows the background subtracted symmetric mass distribution and the Monte Carlo fit. Since the mass is a function of α_{EM} and δ_{EM} these two quantities are correlated.

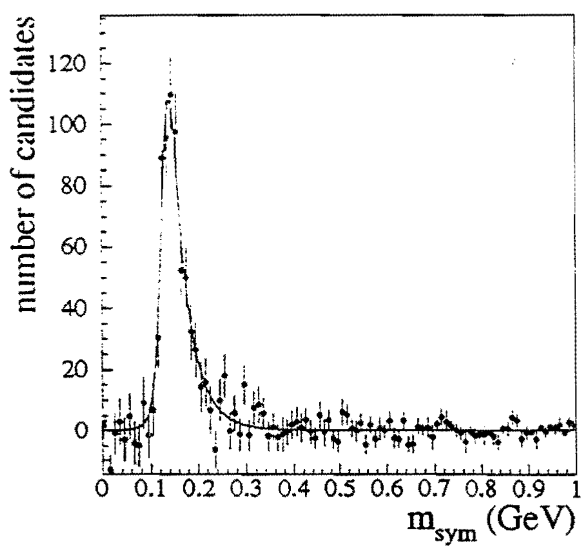

Figure 4.5: The background subtracted m_{sym} distribution. The superimposed curve shows the Monte Carlo simulation.

[1]The symmetric mass is equal to the invariant mass if the decay was symmetric and larger for asymmetric decays.

$J/\psi \to e^+e^-$

A sample of J/ψ events was collected during special runs with low E_T dielectron trigger. Figure 4.6 shows the dielectron invariant mass spectrum for the $J/\psi \to e^+e^-$ sample (-), the background (•) and a gaussian lineshape on top of the background predicted using a sample of EM clusters without CDC tracks. The measured mass is:

$$3.03 \pm 0.04(\text{stat}) \pm 0.19(\text{syst})\text{GeV/c}^2 \tag{4.11}$$

A Monte Carlo simulation of $p\bar{p} \to b\bar{b} = X$, $b \to J/\psi + X$ predicts an observed mean mass

$$\langle m_{\text{obs}} \rangle = \alpha_{EM} m_{J/\psi} + 0.56\delta_{EM} \tag{4.12}$$

which together with the measurement restricts the allowed parameter space for α_{EM} and δ_{EM}.

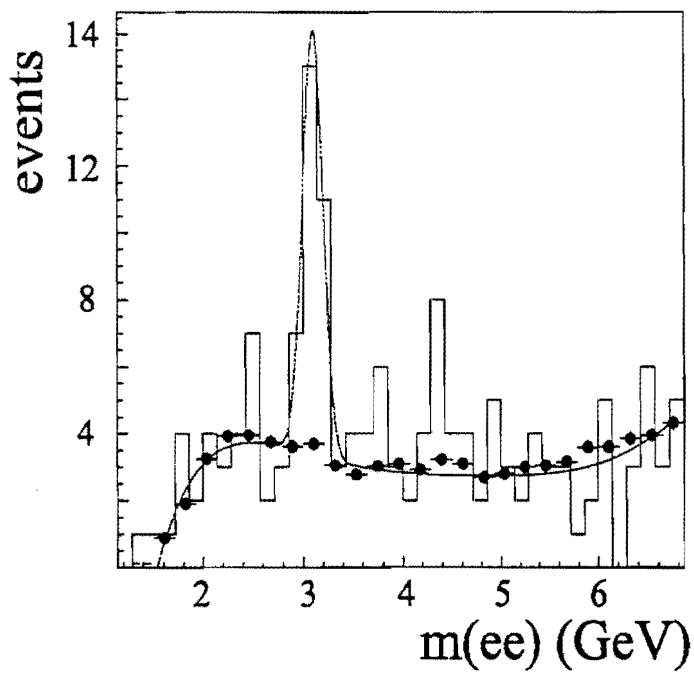

Figure 4.6: The dielectron invariant mass spectrum for the $J/\psi \to ee$ sample (histogram) and background sample (•). The smooth curve is a fit to the data.

$Z \to e^+e^-$

Fixing the observed Z boson mass to the measured value 91.1865 ± 0.0020 GeV/c^2 [36] correlates the values allowed for α_{EM} and δ_{EM}. For a given δ_{EM} the electron energy scale α_{EM} is determined so that the position of the Z peak predicted by the Monte Carlo agrees with the data. A maximum likelihood fit to the $m(ee)$ spectrum between 70 GeV/c^2 and 110 GeV/c^2 is performed to determine the scale factor that best fits the data. Figure 4.7 shows the $m(ee)$ spectrum for the CC-CC Z sample and the Monte Carlo spectrum that best fits the data for $\delta_{EM} = 0.16$ GeV/c^2.

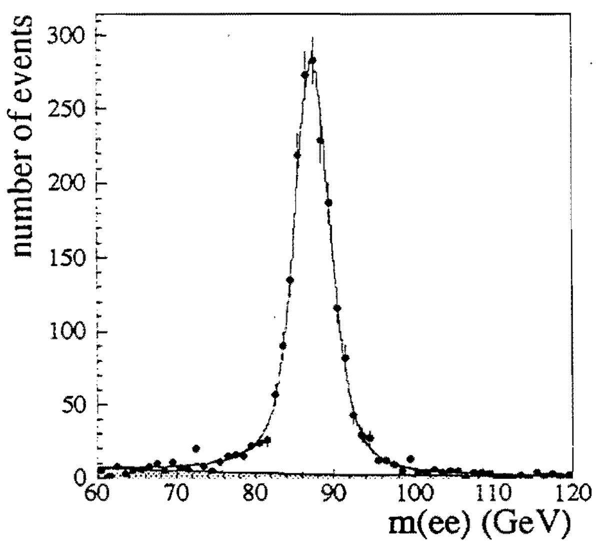

Figure 4.7: The dielectron mass spectrum from the CC-CC Z sample. The superimposed curve shows the maximum likelihood fit and the shaded region corresponds to the fitted background.

The constraints on α_{EM} and δ_{EM} from the three data sets can be combined to extract α_{EM} and δ_{EM} by adding the χ^2 contributions (equation 4.9) from each data set as:

$$\chi^2_{\mathrm{TOT}} = \chi^2_Z + \chi^2_{J/\psi} + \chi^2_{\pi^0} \tag{4.13}$$

Figure 4.8 shows the 68% confidence level contours in the α_{EM}-δ_{EM} parameter space from the three resonances and the combined contour. The π^0 and J/ψ contours essentially fix δ_{EM} independent of δ_{EM}, while the requirement that the Z peak position agree with the LEP measurement of the Z boson mass correlates α_{EM} and δ_{EM}. The measured values for α_{EM} and δ_{EM} are:

$$\alpha_{EM} \quad = \quad 0.9533 \pm 0.0008 \tag{4.14}$$

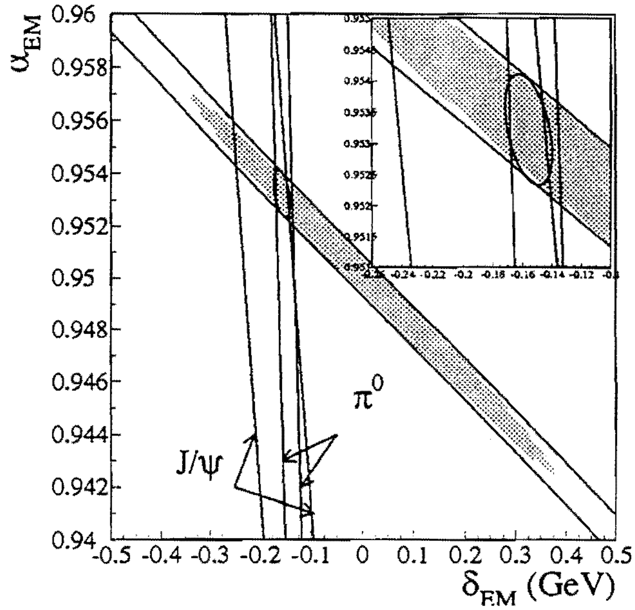

Figure 4.8: The 68% confidence level contours in α_{EM} and δ_{EM} from the J/ψ, π^0, and Z data. The ellipses are explained in the text.

$$\delta_{EM} = -0.16^{+0.03}_{-0.021}\,\mathrm{GeV/c^2} \tag{4.15}$$

For a detailed description of the π^0 analysis see references [37, 38], for the J/ψ analysis [39] and for the Z analysis [40, 31, 32].

Chapter 5

Background in the Z sample

Soy el desordenado hacedor de las más escondidas rutas,
de los más secretos atracaderos.
De su inutilidad y de su ignota ubicación se nutren mis dias.

Álvaro Mutis, La nieve del almirante.

Even though the process $Z \rightarrow e^+e^-$ has a clean signature with two electrons in the final state, there are other physics processes which present the same dielectron final state, as well as instrumental effects which can lead to the same final state constituting sources of background that contaminate the final event sample.

The largest contribution to the background comes from the QCD process of dijet production, where both jets fluctuate electromagnetically, and the direct photon production process where both the photon and the jet are identified as electrons. The Drell-Yan mechanism and the $Z \rightarrow \tau\tau \rightarrow ee\nu\nu$ also contribute to the production of two isolated electrons.

5.1 QCD Background

QCD events in which jets are misidentified as Electromagnetic (EM) objects constitute the largest source of background to the $Z \rightarrow e^+e^-$ process. This QCD events are basically direct photon events and dijet events. The cross section of these two event type with E_T of the jet/photon > 25 GeV differ by a factor of 10^3 [41] so the final contributions are approximately equal since only one jet must fake an electron in the direct photon case whereas the two jets must fake an electron in the dijet case. In principle, these two production mechanisms might result in different x distributions for the background. It also might be taken into account that the resolution for jets is much worse than the resolution for EM objects, so one might expect that only highly electromagnetic jets (objects that were electron candidates, but failed the final quality criteria) would be useful to describe the shape of the background.

5.1.1 Selection of samples to estimate the background

To estimate the QCD background present in the data sample we used the data sample described in section 3.4 as well as MC events generated using NYU MC, (see section 4.2). The MC sample was selected in the same way as the data sample. In order to properly address the issues before mentioned (see section 5.1) several background samples were used to estimate the effects of different detector resolutions and/or different production mechanisms on the background shape. The background samples used for the analysis are the following:

Sample A Bad di-electron, where both electrons fail at least one of the calorimeter quality cuts.

Sample B Di-jets, selected as good jets according to the QCD group's criteria for good jets.

Sample C Direct photon, selected according the direct-photon group criteria.

Besides the standard fiducial and kinematic cuts (the same cuts used for the data and MC samples) applied to each of the following samples, the actual selection criteria for each sample is as follows:

Sample A A bad EM object is defined as an EM object from the QCDWZ group ntuples which fail at least one of the quality cuts, i.e. a bad EM object is selected if it is in the fiducial region and also passes at least one of the following anti-quality cuts:

- Electromagnetic fraction ≤ 0.90
- H matrix $\chi^2 \geq 100$
- Isolation fraction ≥ 0.15

Figure 5.1 shows sample A invariant mass distributions for the three cryostats.

Sample B The dijet sample was selected from the global QCD ntuples using the following cuts:

- *jet_min* triggered
- Both jets with $E_T > 25$ GeV
- $0.5 <$ Electromagnetic fraction < 0.9

- Coarse hadronic fraction < 0.4
- $N_{\text{hot cell}} < 20$
- $\frac{\not{E}_T(\text{event})}{E_T(\text{lead jet})} < 0.7$

Figure 5.2 shows sample B invariant mass distributions for the three cryostats.

Sample C The direct photon sample was selected from the direct photon group's ntuples with the following cuts:

- *em_gis* triggered
- Event $\not{E}_T < 20$ GeV
- $E_T^{\text{iso}}(\gamma) < 2.0$
- Electromagnetic fraction $(\gamma) > 0.95$
- H matrix $\chi^2(\gamma) < 100$

Figure 5.3 shows sample C invariant mass distributions for the three cryostats.

As well as with the data and MC samples, the invariant mass of the pairs e^+e^-, $\gamma - j$ or jj was required to be in the range 50 GeV/c^2 $\leq M(ee) \leq$ 130 GeV/c^2 for the maximum likelihood fit and to extract the actual background fraction the invariant mass of the pair was required to be in the range 75 GeV/c^2 $\leq M(ee) \leq$ 105 GeV/c^2.

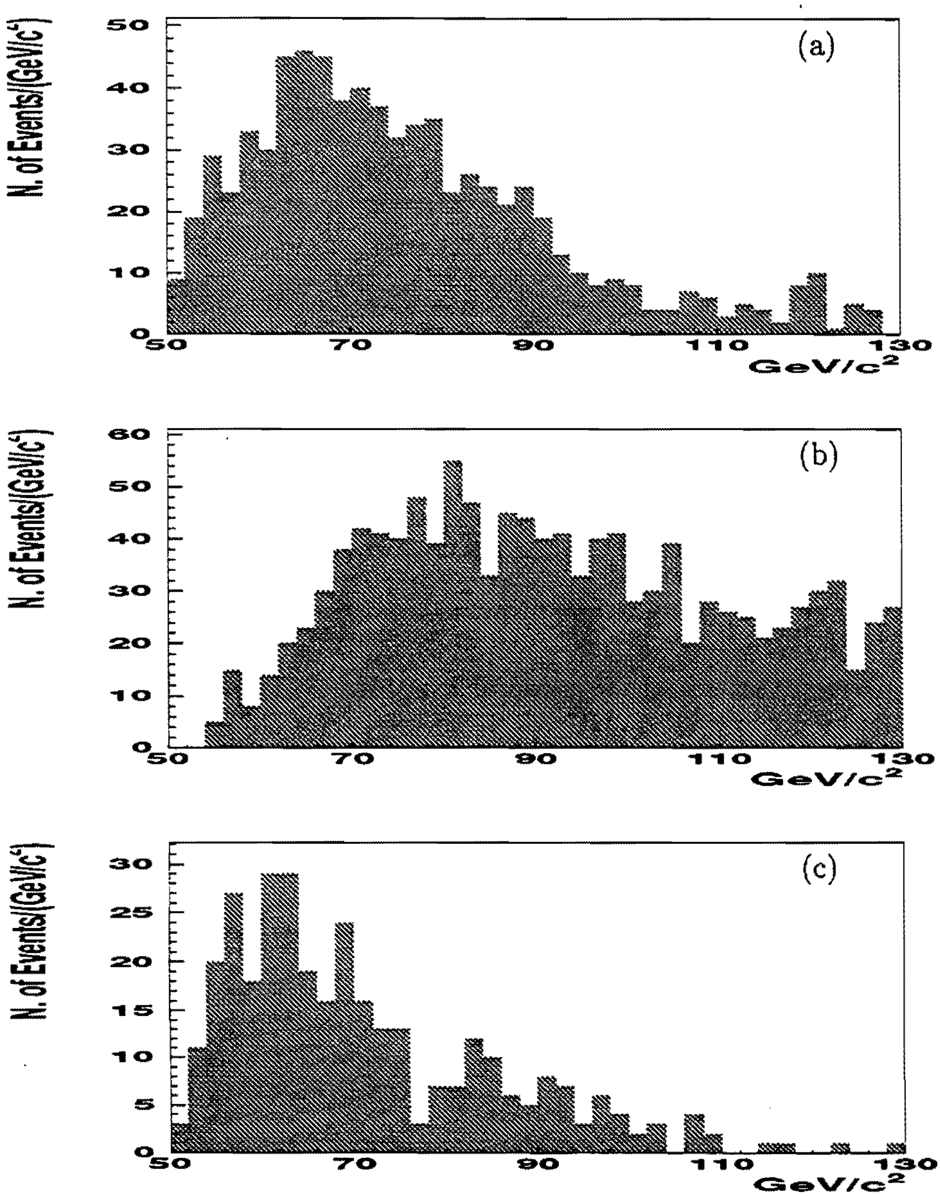

Figure 5.1: Sample A bad di-electron invariant mass distributions for (a) CC-CC events, (b) CC-EC events and (c) EC-EC events.

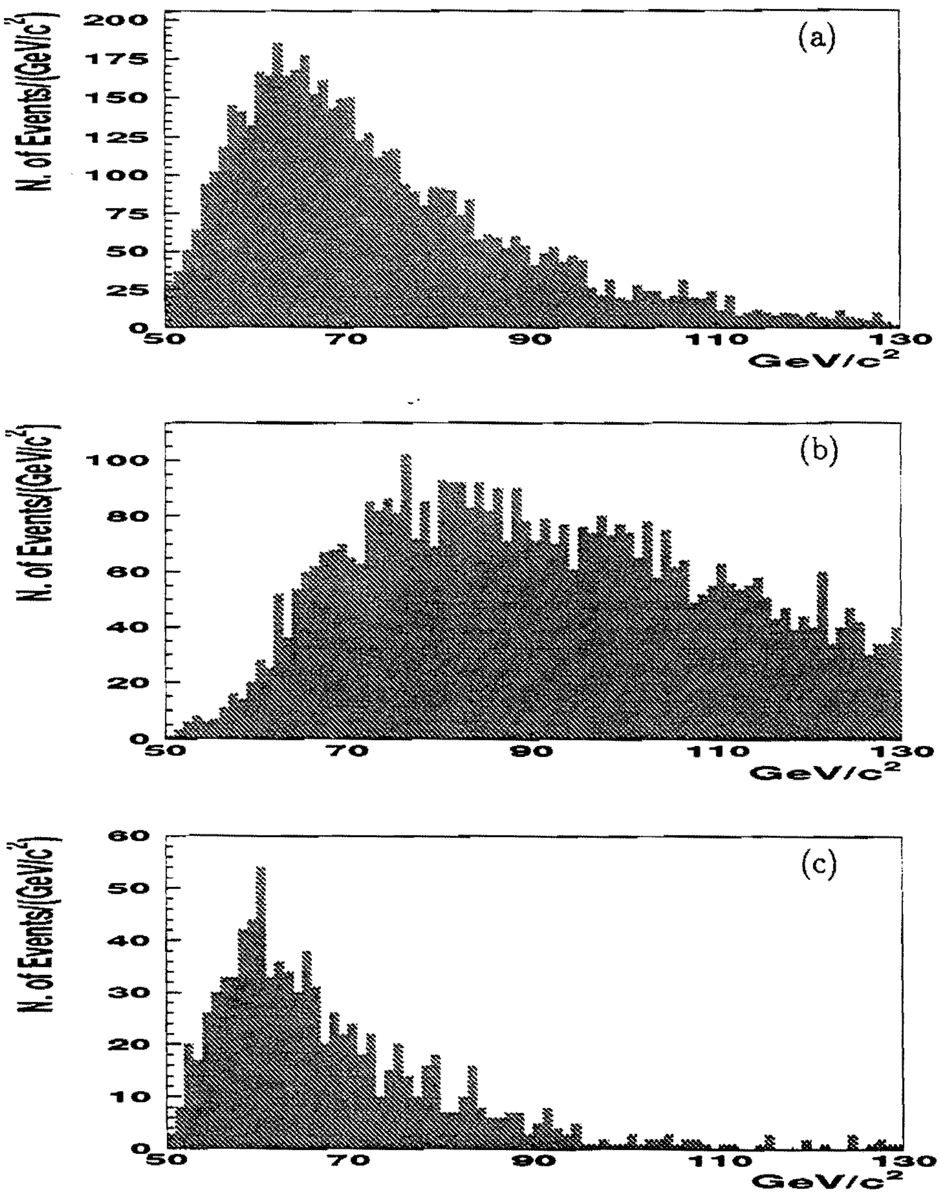

Figure 5.2: Sample B di-jet invariant mass distributions for (a) CC-CC events, (b) CC-EC events and (c) EC-EC events.

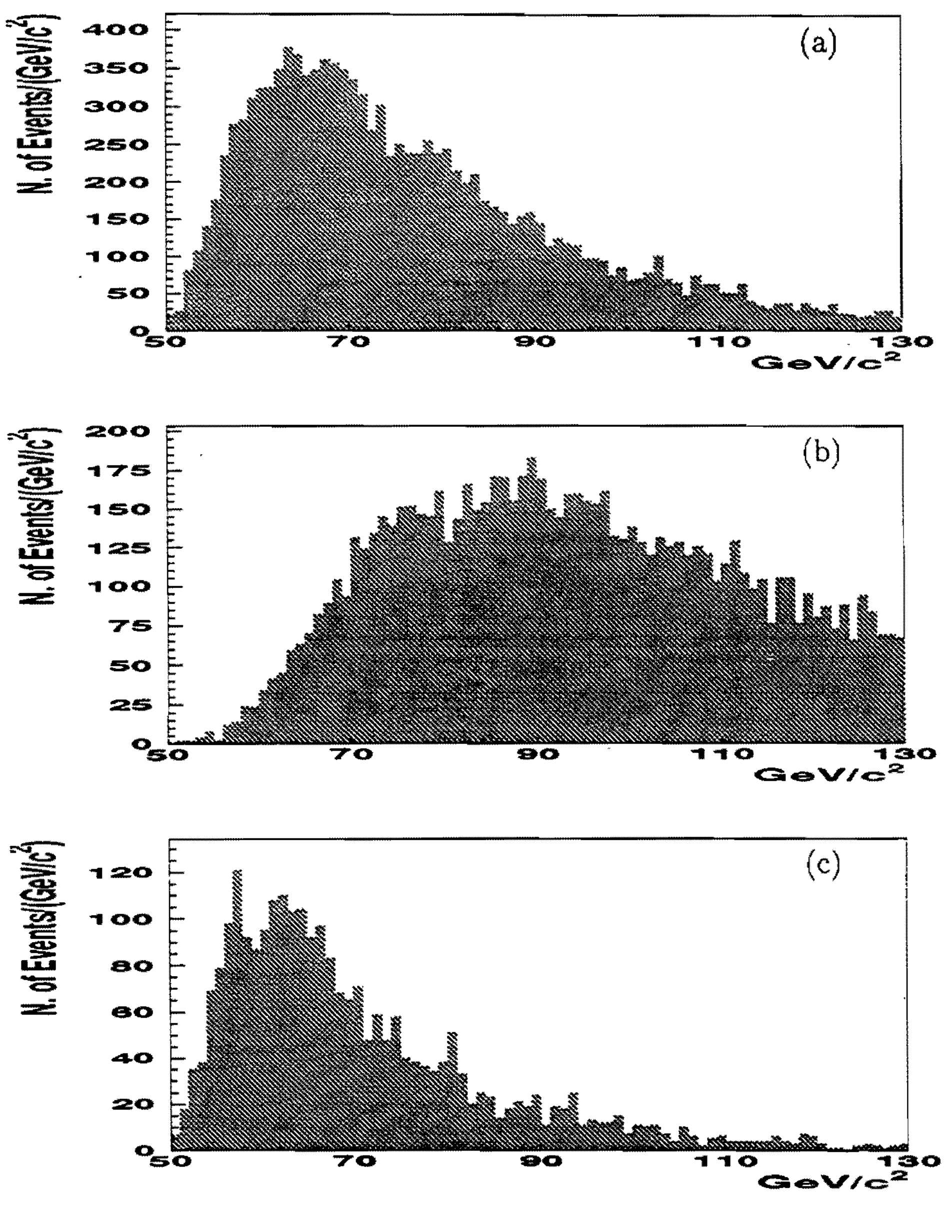

Figure 5.3: Sample C direct photon invariant mass distributions for (a) CC-CC events, (b) CC-EC events and (c) EC-EC events.

5.1.2 Estimation of the background fraction

To extract the amount of QCD background contained in the $Z \to e^+e^-$ sample the invariant mass distribution of the data, $N_{\text{data}}(m)$ is fitted to the sum of the predicted (MC) signal $N_{\text{MC}}(m)$ and the background $N_{\text{bckgnd}}(m)$ distributions.

$$N_{\text{data}}(m) = c_1 \cdot N_{\text{MC}}(m) + c_2 \cdot N_{\text{bckgnd}}(m) \tag{5.1}$$

where c_1, c_2 are the normalization constants for the MC and the background respectively. This fit is done using the function HMCMLL provided by the HBOOK [42] package. The function takes the data, MC and background histograms as input, and returns the values of c_1 and c_2 which are normalized to 1. In order to obtain the correct background fraction it is necessary to renormalize to the total number of events in the data histogram. The final expression to calculate the QCD background fraction is:

$$f_{\text{qcd}} = c_2 \cdot \frac{N^{\text{tot}}_{\text{data}}}{N^{\text{tot}}_{\text{bckgnd}}} \cdot \frac{N^{75\text{-}105}_{\text{bckgnd}}}{N^{75\text{-}105}_{\text{data}}} \tag{5.2}$$

where $N^{\text{tot}}_{\text{data}}$ is the total number of events in the data histogram and $N^{75\text{-}105}_{\text{data}}$ is the number of events with a mass within the range from 75 to 105 GeV/c^2 and equivalently for the background histograms.

The fractions are shown in table 5.1(the error quoted on the tables is statistical only and corresponds to one standard deviation from the maximum likelihood). Figure 5.4 shows the result of the fit for the direct photon sample, the inset corresponds to the likelihood curve. The fits are reasonably good with a χ^2/n.d.f. that goes from 28.0/30 in the best case to 151.0/30 in the worst case.

Sample	CC-CC	CC-EC	EC-EC
A	4.330 ± 0.386	7.162 ± 0.667	7.015 ± 0.880
B	3.244 ± 0.280	7.191 ± 0.659	4.784 ± 0.551
C	4.161 ± 0.341	8.044 ± 0.711	5.612 ± 0.626

Table 5.1: Background fraction obtained using the data, MC and background histograms directly as input for HMCMLL.

We calculated the background fraction performing a weighed average of the background fractions of samples A, B and C. The results from the average are shown in table 5.2

5.1.3 Systematic errors on the background fraction

Since the three background samples used to calculate the background fraction are independent we can estimate the systematic error on the background fraction as the

CC-CC	CC-EC	EC-EC
3.78 ± 0.19 %	7.44 ± 0.39 %	5.47 ± 0.37 %

Table 5.2: Weighed average of the background fractions of samples A, B and C. The error is only statistical.

largest deviation from the average. This systematic error is shown in table 5.3.

CC-CC	CC-EC	EC-EC
0.55 %	0.60 %	1.55 %

Table 5.3: Systematic error in the background fraction estimated as the maximum deviation from the weighed average.

To test the accuracy of the fits using HMCMLL we generated "fake data samples" with an arbitrary amount of background and using the MC and background samples we checked if HMCMLL returned the correct background fraction.

These fake data samples were built by adding up a MC subsample and a "fake background sample" with the adequate number of events in the window of mass such that the final fake data sample contains the desired amount of background. To calculate the number of events in the window of mass of the fake background sample $N_{f-bckgnd}$ we assumed that the MC subsample had N_{MC} events in the same window of mass. The fake data sample will have then: $N_{f-data} = N_{MC} + N_{f-bckgnd}$ events in the window of mass. Since the background fraction f_{bckgnd} is calculated as:

$$f_{bckgnd} = 100 \cdot \frac{N_{f-bckgnd}}{N_{f-data}} = 100 \cdot \frac{N_{f-bckgnd}}{N_{MC} + N_{f-bckgnd}}$$

We can calculate $N_{f-bckgnd}$ for any desired background fraction as follows:

$$N_{f-bckgnd} = \frac{f_{bckgnd}}{(100 - f_{bckgnd})} \cdot N_{MC}$$

The fake background sample was generated using HISRAN[1] from CERN library [43], using the shape of background sample A (see section 5.1.1) as input.

We built four sets of fake data samples containing 1.5, 3.0, 5.0 and 8.0 % of background for each of the combinations CC-CC, CC-EC and EC-EC. Figure 5.5 shows the

[1]HISRAN generates random numbers according to any empirical distribution supplied in the form of a histogram.

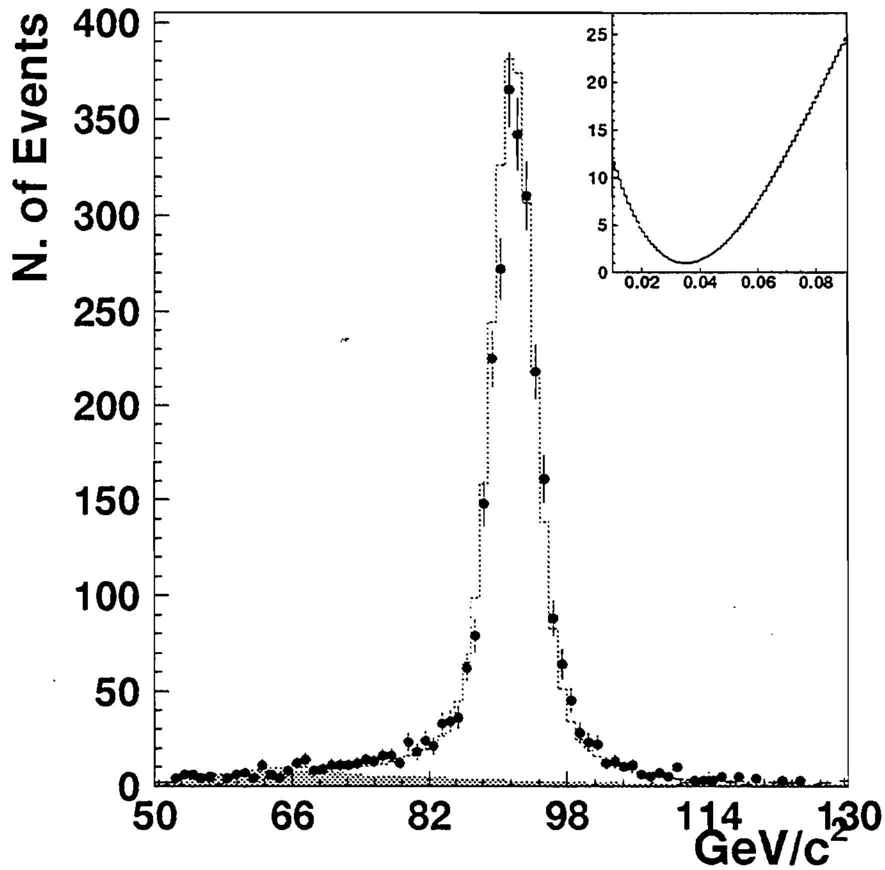

Figure 5.4: Result from the HMCMLL fit for data, MC and direct photon (background) samples. Dots are data, the solid histogram is the normalized histogram after the fit and the shadowed histogram is the normalized background. The inset is the likelihood curve.

plots used in the process of building the fake signal histogram with 1.5 % background and Fig. 5.6 shows the histograms used to build the fake signals with 3 %, 5 % and 8 % of background.

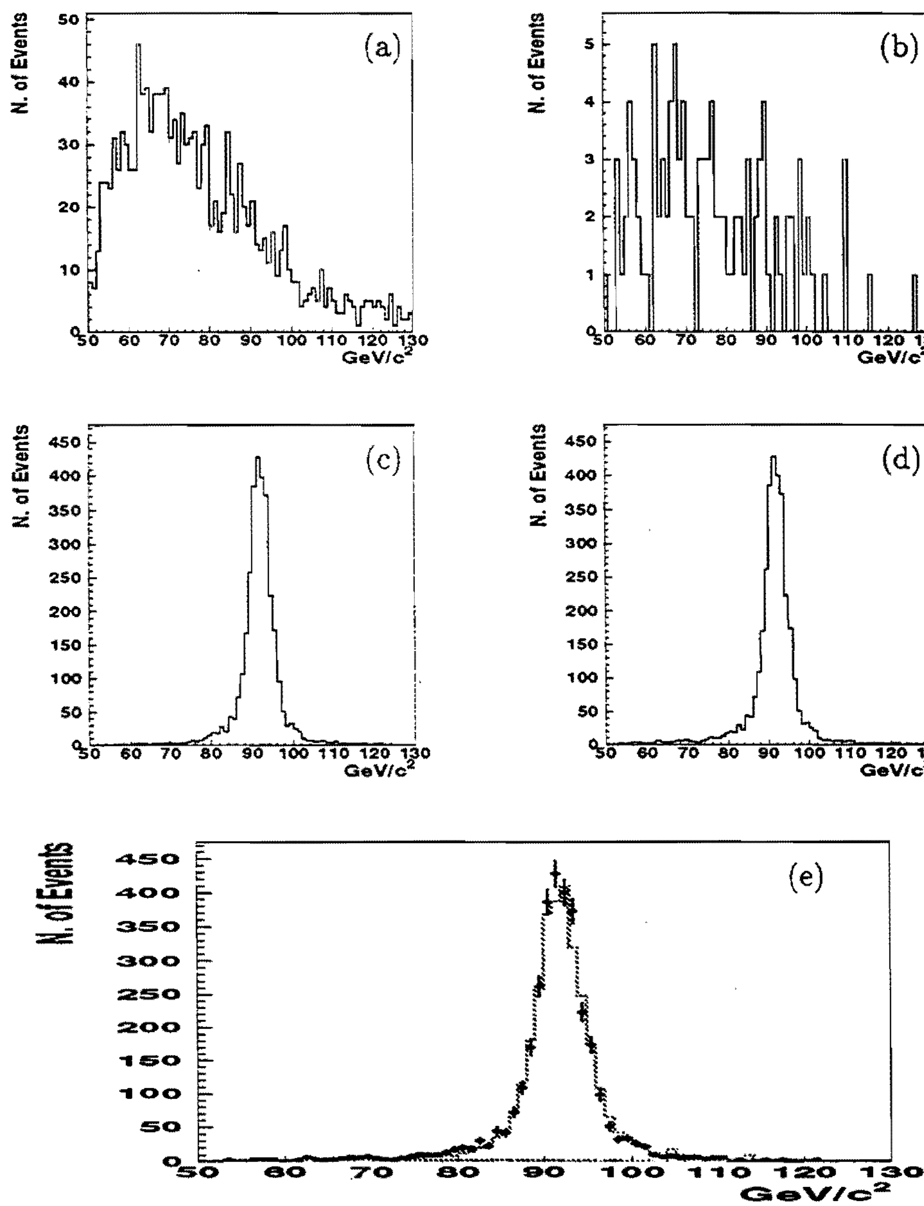

Figure 5.5: Different histograms used to build a fake signal distribution containing 1.5% background. (a) Background shape used to generate the background to be added to the MC. (b) Generated background to be added to the MC. (c) MC shape used to build the fake signal. (d) Generated fake signal with 1.5 % background built by adding histograms (b) and (c). (e) Comparison of the fake signal with the normalized background and MC.

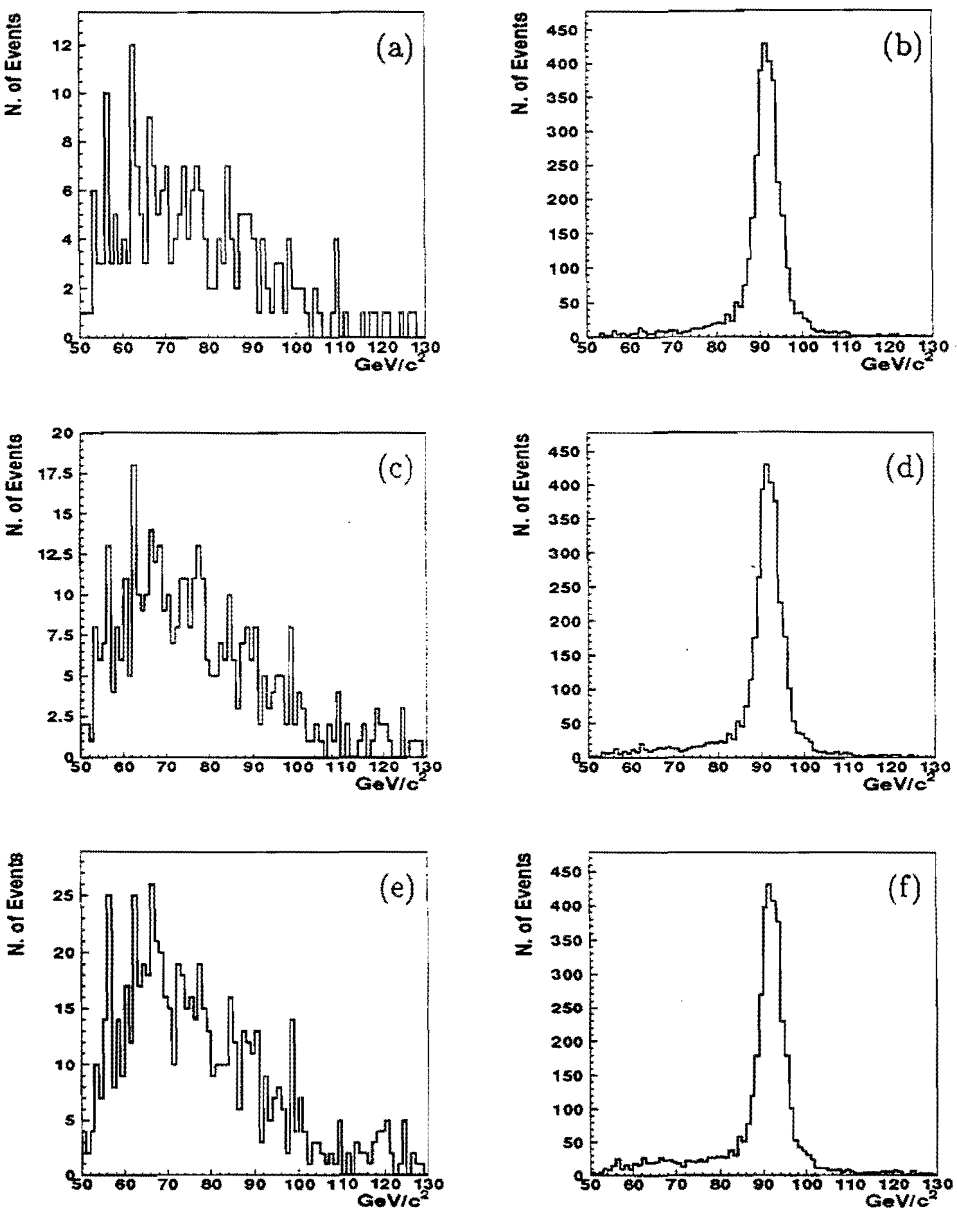

Figure 5.6: Histograms used to build fake signal distributions containing 3 %, 5 % and 8 % background. (a) Generated 3 % background. (b) Generated fake signal containing 3 % background. (c) Generated 5 % background. (d) Generated fake signal containing 5 % background. (e) Generated 8 % background. (f) Generated fake signal containing 8 % background.

Using the fake signal histograms, all the MC subsamples (see section 5.1.1) and background sample A (see section 5.1.1) we calculated the background fraction using one MC sample at a time. As it can be seen in Fig. 5.7 there is a systematic shift in the returned background fraction. Table 5.4 summarizes the mean and r.m.s. obtained for all the contributions varying the MC subsample.

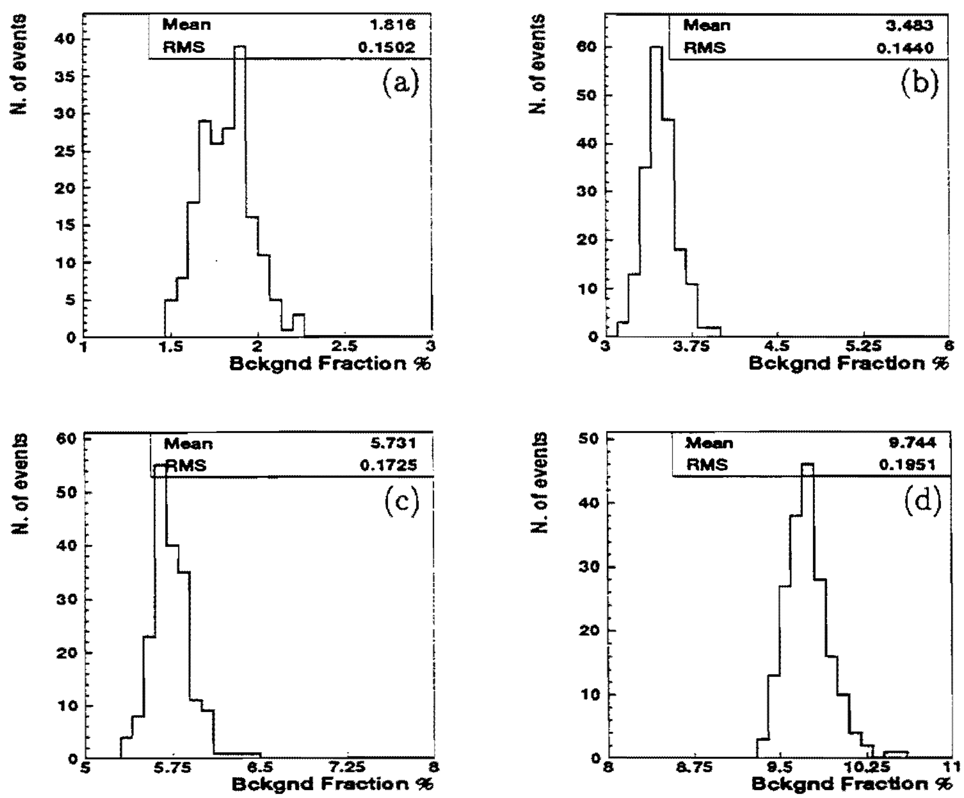

Figure 5.7: Background fraction distributions for CC-CC events varying the MC. (a) 1.5 % background fraction, (b) 3 % background fraction, 5 % background fraction and (c) 8 % background fraction.

We repeated the same experiment but this time generating "fake background samples" using **HISRAN** [43], the input for HISRAN was the shape from background sample A (see section 5.1.1). Then using again **HMCMLL** and doing a loop over the fake background samples, we got as output the mean and r.m.s quoted in Table 5.5.

For completeness we repeated the procedure described above a third time, now keeping the same background and MC histograms and varying the fake signal. The results are summarized in Table 5.6.

From tables 5.4,5.5 and 5.6 we can see that the fitter returns, in general, a larger background fraction. It is noticeable that the largest the input background fraction the

Input background fraction	CC-CC		CC-EC		EC-EC	
	Mean	r.m.s.	Mean	r.m.s.	Mean	r.m.s.
1.5 %	1.816	0.1502	2.272	0.3231	2.447	0.3337
3.0 %	3.483	0.1440	3.825	0.3413	4.130	0.2767
5.0 %	5.731	0.1725	5.832	0.3406	5.391	0.3343
8.0 %	9.744	0.1951	10.38	0.3918	8.091	0.3183

Table 5.4: Summary of means and r.m.s. of the background fraction distributions for the different event contributions and for each of the generated input fake samples when looping over all the MC subsamples.

Input background fraction	CC-CC		CC-EC		EC-EC	
	Mean	r.m.s.	Mean	r.m.s.	Mean	r.m.s.
1.5 %	1.579	0.089	1.807	0.1293	2.033	0.1320
3.0 %	3.215	0.162	3.101	0.2001	3.801	0.2038
5.0 %	5.350	0.490	4.626	0.3820	4.888	0.4831
8.0 %	9.332	0.409	10.70	0.5749	7.636	0.3762

Table 5.5: Summary of means and r.m.s. of the background fraction distributions for the different event contributions and for each of the generated input fake samples when looping over the generated fake background samples.

Input background fraction	CC-CC		CC-EC		EC-EC	
	Mean	r.m.s.	Mean	r.m.s.	Mean	r.m.s.
1.5 %	1.713	0.1341	2.213	0.3352	2.347	0.3650
3.0 %	3.391	0.1454	3.605	0.3438	4.215	0.2674
5.0 %	5.626	0.1608	5.636	0.3156	5.365	0.2985
8.0 %	9.584	0.1748	10.03	0.3544	8.252	0.3224

Table 5.6: Summary of means and r.m.s. of the background fraction distributions for the different event contributions and for each of the generated input fake samples when looping over the generated fake signal samples.

largest the shift. To estimate the systematic shift in the output of the fitter we picked the worst entry from these three tables (see table 5.7), then, we made a linear fit to the returned fraction as a function of the input fraction. From the fit we calculated the corresponding expected shift to the actual background fractions from table 5.2. This shift is taken as a systematic error from the fitter, the systematic error is shown in table 5.8.

Input background fraction	CC-CC		CC-EC		EC-EC	
	Mean	r.m.s.	Mean	r.m.s.	Mean	r.m.s.
1.5 %	1.816	0.1502	2.272	0.3231	2.447	0.3337
3.0 %	3.483	0.1440	3.825	0.3413	4.215	0.2674
5.0 %	5.731	0.1725	5.832	0.3406	5.365	0.2985
8.0 %	9.744	0.1951	10.70	0.5749	7.636	0.3762

Table 5.7: Worst entries from tables 5.4, 5.5 and 5.6.

CC-CC	CC-EC	EC-EC
0.57	1.52	0.42

Table 5.8: Systematic error from the fitter.

5.1.4 QCD Background shape as a function of x_Z, x_1 and x_2

Since the measurement of the longitudinal momentum distributions x_Z, x_1 and x_2 is shape sensitive it is necessary to obtain the shape of the x background distributions. In order to get the best approximation to the real background shape we averaged the shapes of background samples A (see section 5.1.1), D and E, corresponding to the "standard" bad dielectron, dijet and direct photon samples, respectively. We discarded samples C and D because they are overlapped with sample A since the three samples are bad dielectron samples with different degrees of badness. Figure 5.8 shows the shape of the x_Z distribution for CC-CC events for the three samples used to estimate the background shape in terms of the x distributions.

Figure 5.9 shows the average shape compared with the shapes of the three averaged distributions for each of the x distributions and for each of the cryostat contributions. The error in the average shape is taken from the maximum deviation of any of the averaged distributions plus (minus) its error to the average distribution. Figure 5.10 shows the average background for each of the x distributions.

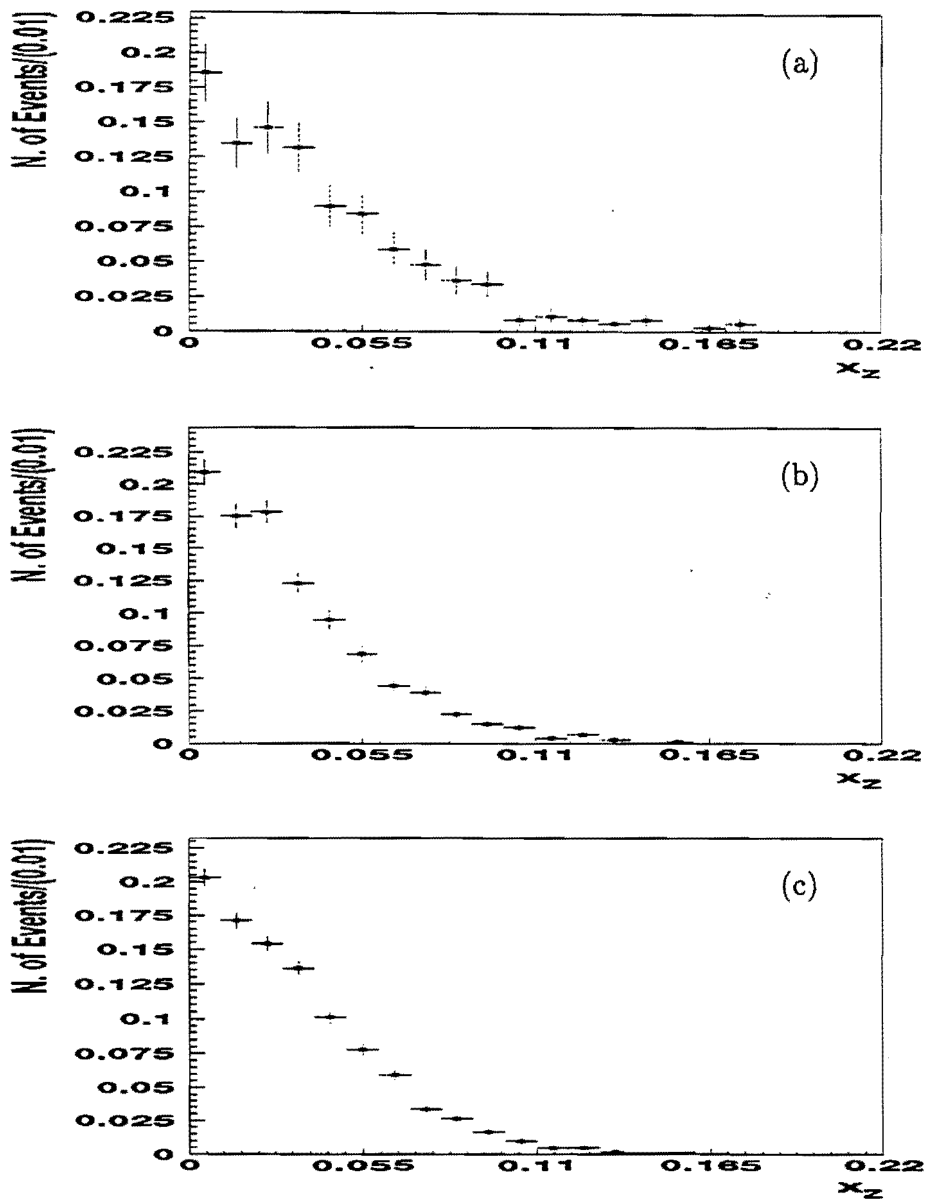

Figure 5.8: x_Z distributions for CC-CC background events: (a) standard bad dielectron, (b) dijets and (c) direct photon samples.

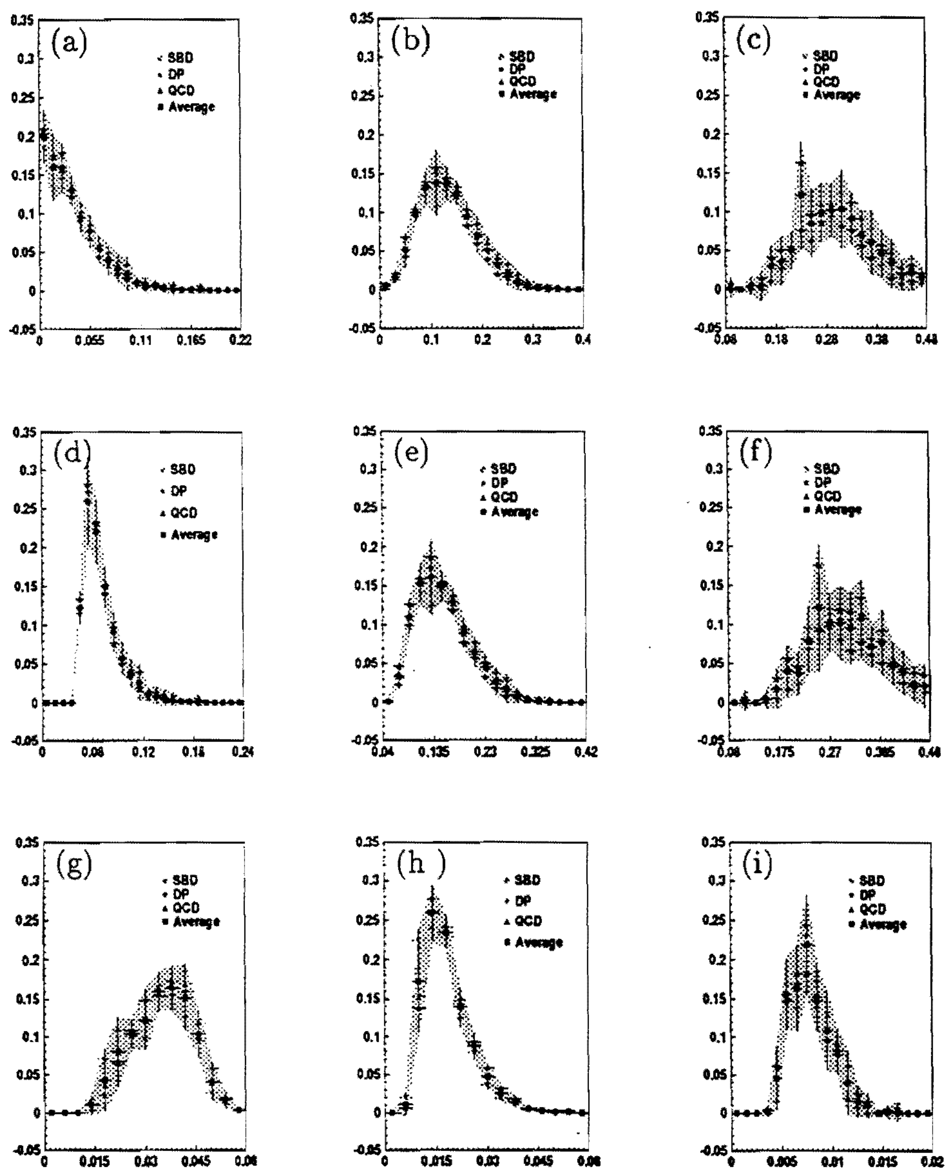

Figure 5.9: Average background for each of the x distributions and for each of the cryostat contributions. The shaded region corresponds to the calculated error in the average as the maximum deviation of any of the averaged distributions plus (minus) its error from the average. Top row corresponds to x_Z distributions, in the middle row are the x_1 distributions and bottom row are x_2 distributions. Going from left to right the columns are for CC-CC, CC-EC and EC-EC distributions respectively.

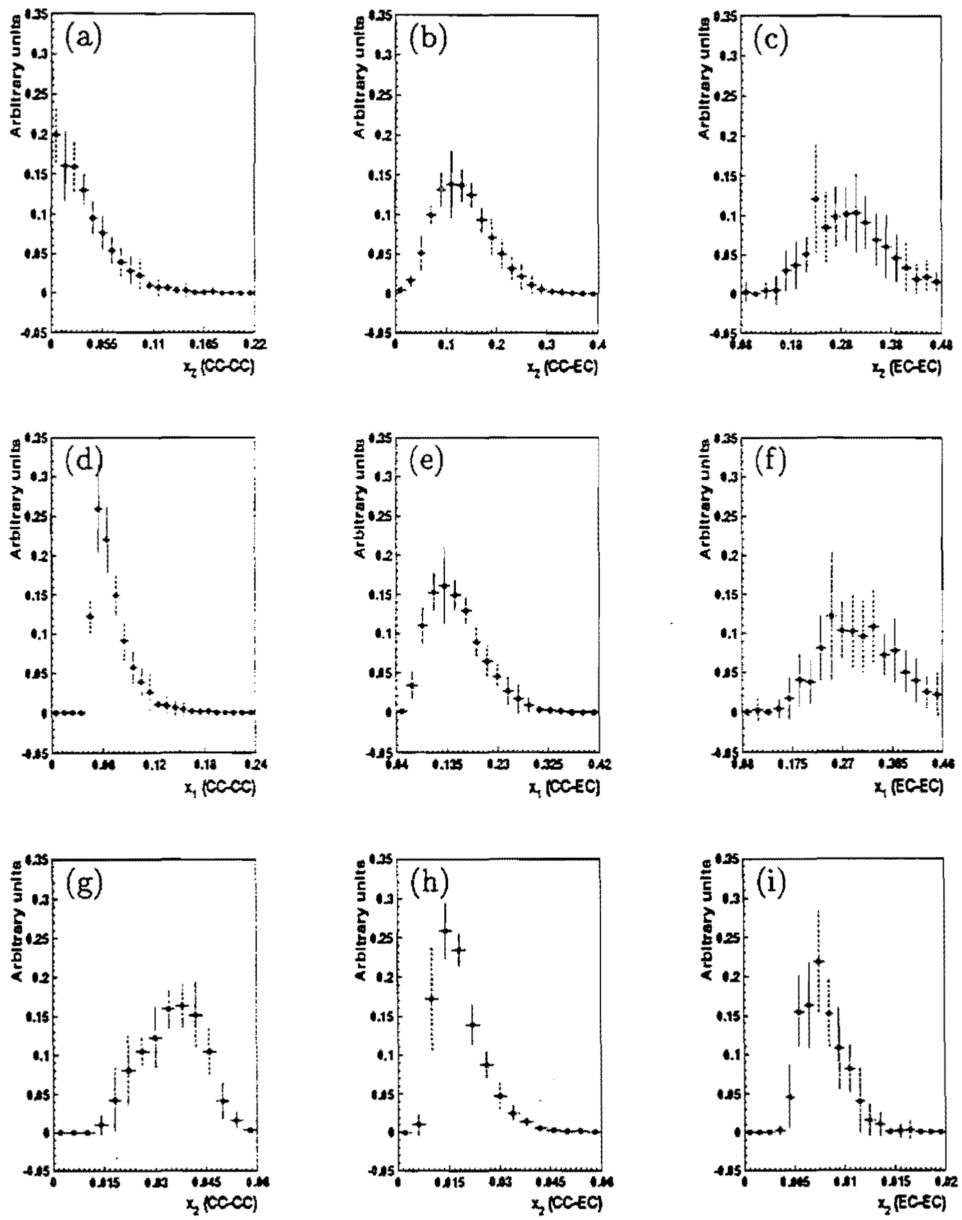

Figure 5.10: Average background for each x distribution. Top row corresponds to x_Z distributions, in the middle row are the x_1 distributions and bottom row are x_2 distributions. Going from left to right the columns are for CC-CC, CC-EC and EC-EC distributions respectively.

5.2 Drell Yan background estimation

We estimated the background contribution coming from Drell Yan events using MC samples generated with PYTHIA [44] and passed through CMS for detector simulation. The fraction of events coming from Drell Yan and the interference terms was calculated by taking the ratio of the cross sections for the processes $p\bar{p} \to Z/\gamma^* \to ee$ and $p\bar{p} \to Z \to ee$ in the window of mass [75,105]. The results are quoted in table 5.9. The statistical error associated with this calculation is negligible due to the high statistics sample used. These results agree reasonably well with the ones in [45], except for the EC-EC, where they quote 1.2 %.

	CC-CC	CC-EC	EC-EC
Background fraction (%)	1.11	1.50	2.97

Table 5.9: Estimated background fraction from Drell Yan events.

Figure 5.11 shows the shape of the x distributions for the Drell Yan background events.

5.3 $Z \to \tau\tau$ background

The process $Z \to \tau\tau$ where both τ decay electronically constitutes another source of physics background. However this background contribution can be safely neglected because it is highly suppressed by the branching ratios: the decay rate of the Z boson to electrons is the same than the one of $Z \to \tau\tau$ (3.36%) [8] but taking into account the branching ratio of the two taus decaying to electrons, an additional $(18.01\%)^2$ make this source of background negligible. This was verified in the Run 1a analysis [46] with 900 MC $Z \to \tau\tau \to ee$ events. After applying the 25 GeV P_T cut to both electrons only 17 events survived, and whit the requirement of an invariant mass greater than 25 GeV/c^2 only one event survived.

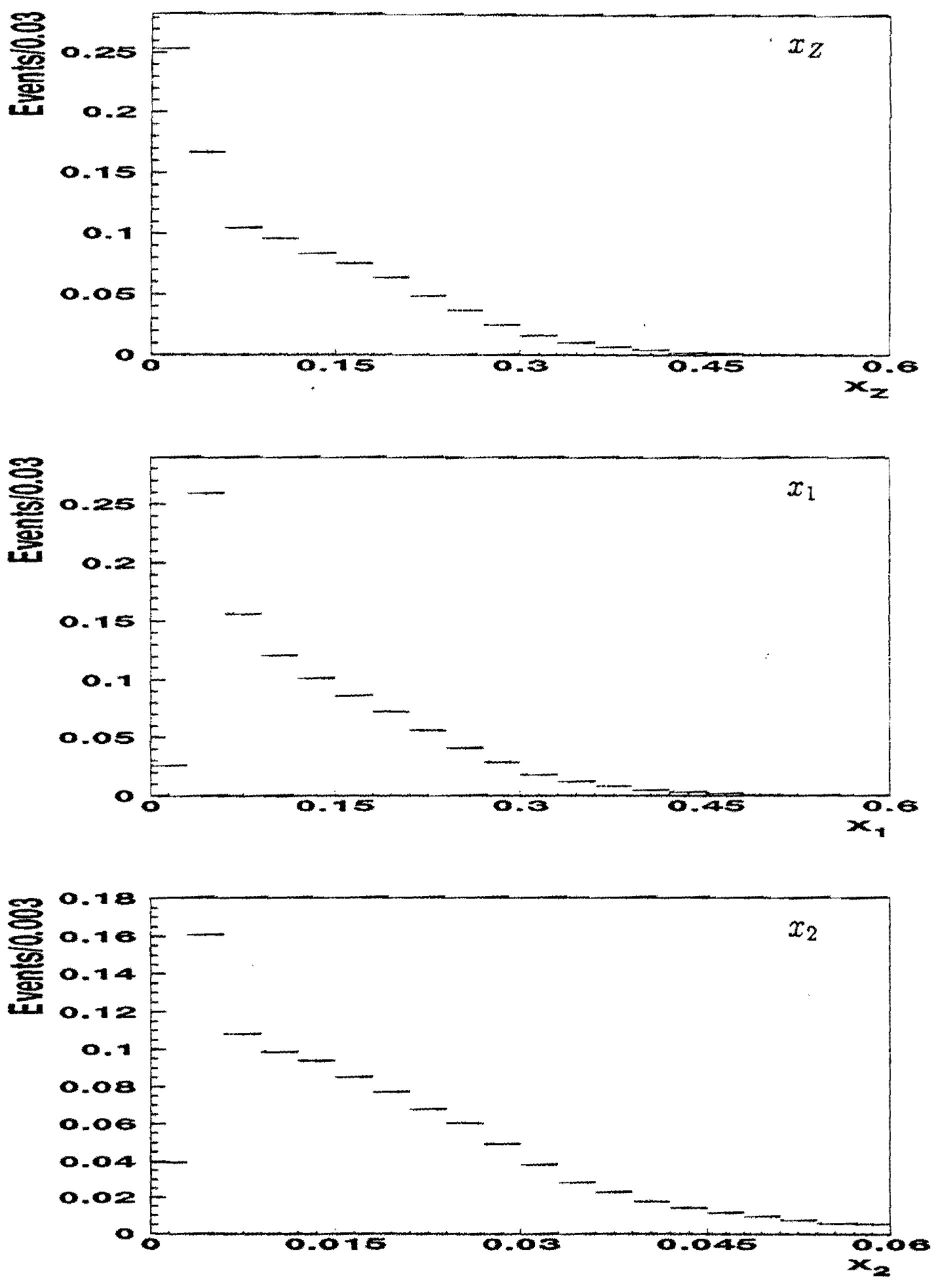

Figure 5.11: x_Z, x_1 and x_2 Drell Yan background distributions.

Chapter 6

Resolution effects

Voici mon secret. Il est très simple:
on ne voit bien qu'avec le coeur.
L'essentiel est invisible pour les yeux.[1]

Antoine de Saint-Exupery (Le Petit Prince).

The following chapter is devoted to the study of the resolution effects on the measurement of the longitudinal momentum distribution of the Z boson.

The resolution for the variables x_Z, x_1 and x_2 is directly derived and compared to the calculated resolutions from MC. The bias due to smearing effects is studied and the systematic error due to model dependance on the MC is estimated by varying the parameters of the resolution function used to simulate the smearing of the detector.

Two methods were used to estimate the resolution effects: *i)* The first method calculates the resolution of x_Z, x_1 and x_2 based on known detector resolution. *ii)* The second method uses Monte Carlo data samples. The Monte Carlo samples used for the resolution effects studies are described in sections 4.1 and 4.2.

6.1 Data sample

The data sample used in this part of the analysis was collected in the 1992-1993 Tevatron collider Run 1a. DST files with generic name: ZEE_RGE_V11_XXXX.DST, preselected by the electroweak group were used. The following cuts were applied:

- Runs earlier than 55217 were discarded.
- Bad runs were removed using the file:
  QCD_15$HROOT:[QCD_WZ.MAKE_NT.V6.RCP]BAD_RUN_1A.RCP

[1]It is only with the heart that one can see rightly; What is essential is invisible to the eye.

- DØ RECO version 11.00 or higher.
- Events must pass ELE_2_HIGH L2 filter. This filter requires the event to have at least two electromagnetic towers with more than 7 GeV/c^2 at Level 1 and two electromagnetic clusters with more than 10 GeV/c^2 and isolation at Level 2.

The electron direction is determined using the calorimeter cluster position and the center of gravity of the CDC track, thus, the event vertex for the electron is different from the RECO event vertex. The determination of the calorimeter cluster position depends on the RECO vertex position so, it is recalculated through an iterative process: Using the calorimeter position and the center of gravity of the CDC track a new vertex is determined. This vertex is used to recalculate de calorimeter position, from which a new electron direction and a new vertex position are obtained. This iterative process is stopped when the difference between successive calorimeter positions is less than 0.1 cm. All the relevant quantities are correctly recalculated for the new vertex position.

After this initial global selection and reconstruction of the vertex, dielectron events were selected by applying the following quality and kinematic cuts on electron candidates. A "loose electron" is defined as an EM cluster (PELC or PPHO bank[2]) satisfying the following cuts (see section 3.2):

- $p_T(e) > 25\ GeV/c$.
- Good fiducial region:

$$\begin{array}{ll} \mathrm{CC}: |\eta| < 1.1 & |\phi_{\mathrm{ele}} - \phi_{\mathrm{crack}}| > 0.01, \\ \mathrm{EC}: 1.5 < |\eta| < 2.5, & \end{array}$$

  where the pseudorapidity η is defined[3] by equation 1.12.
- Electromagnetic fraction larger than 0.95.
- $f_{\mathrm{iso}} < 0.1$.
- H matrix $\chi^2 < 100$.

A "tight electron" is defined as a PELC passing the loose electron requirements and having also a matching central detector track with track match significance: σ_{trk} less than 5 (10) if the PELC is in the CC (EC).

[2]Electromagnetic objects which satisfy certain quality requirements are tagged as photons and stored in the PPHO bank, if the object has in addition a track associated with the calorimeter cluster it is tagged as an electron and stored in the PELC bank.

[3]η is calculated with the routine DET_ETA.FOR, given z of vertex and physics theta the routine returns detector eta.

After these cuts were applied we imposed an additional requirement on the invariant di-electron mass, which must be within the mass window of

$$75 \text{ GeV}/c^2 < \text{M}(ee) < 105 \text{ GeV}/c^2.$$

Table 6.1 shows the summary of the final number of events we accepted in each different combination of cryostats.

	CC-CC	CC-EC	EC-EC	Total
Number of events	439	289	65	793

Table 6.1: Summary of the number of Z events from the different combinations of cryostats from the Run 1a sample.

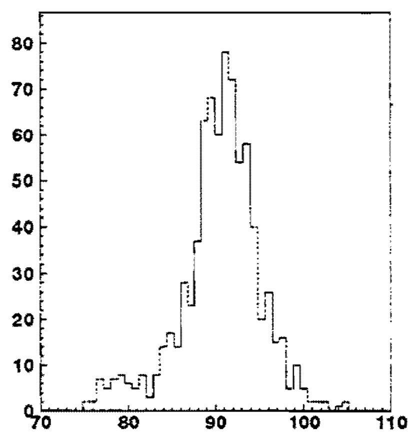

Figure 6.1: Invariant di-electron mass distribution (Run 1a sample).

6.2 Measured resolution

The DØ detector measures the energy and the position of the electrons and positrons using the DØ calorimeters and tracking detectors. x_Z, x_1, x_2 were defined by equations (1.17) and (1.23) as:

$$x_Z = \frac{(E_1 \cos\theta_1 + E_2 \cos\theta_2)}{\frac{1}{2}\sqrt{s}} \tag{6.1}$$

$$x_{1,2} = \frac{1}{2}\left(\sqrt{x_Z^2 + \frac{4M_Z^2}{s}} \pm x_Z\right) \tag{6.2}$$

where:

$$M_Z^2 = 2E_1E_2(1 - (\sin\theta_1 \sin\theta_2 \cos(\varphi_1 - \varphi_2) + \cos\theta_1 \cos\theta_2)) \tag{6.3}$$

and (E_i, θ_i) are the electron energy and polar angle, respectively. Assuming that E_i and θ_i are not correlated, we can use the standard technique for error propagation to calculate the error taking into consideration only the diagonal elements of the error matrix [51, 52]. The error on x_Z is given by:

$$\sigma_{x_Z}^2(E_1, \theta_1, E_2, \theta_2) = \left(\frac{\partial x_Z}{\partial E_1}\right)^2 \sigma_{E_1}^2 + \left(\frac{\partial x_Z}{\partial \theta_1}\right)^2 \sigma_{\theta_1}^2 + \left(\frac{\partial x_Z}{\partial E_2}\right)^2 \sigma_{E_2}^2 + \left(\frac{\partial x_Z}{\partial \theta_2}\right)^2 \sigma_{\theta_2}^2 \tag{6.4}$$

Similar expressions can be obtained for x_1 and x_2, with an extra φ term due to the dependence of x_1 and x_2 on M_Z. Here we list different types of partial derivatives used in the calculation $(i, j = 1, 2)$:

$$\begin{aligned}
\frac{\partial x_Z}{\partial E_i} &= \frac{2}{\sqrt{s}}\cos\theta_i; \qquad \frac{\partial x_Z}{\partial \theta_i} = -\frac{2}{\sqrt{s}}E_i \sin\theta_i \\
\frac{\partial x_j}{\partial \theta_i} &= \left(\frac{\partial x_j}{\partial x_Z}\right)\left(\frac{\partial x_Z}{\partial \theta_i}\right) + \left(\frac{\partial x_j}{\partial M_Z}\right)\left(\frac{\partial M_Z}{\partial \theta_i}\right) \\
\frac{\partial x_{1,2}}{\partial x_Z} &= \frac{1}{2}\left(\frac{x_Z}{\sqrt{x_Z^2 + 4M_Z^2/s}} \pm 1\right) \\
\frac{\partial x_i}{\partial M_Z} &= \frac{2M_Z}{s\sqrt{x_Z^2 + 4M_Z^2/s}} \\
\frac{\partial M_Z}{\partial \theta_1} &= \frac{-E_1E_2\cos\theta_1 \sin\theta_2 \cos(\varphi_1 - \varphi_2) - \sin\theta_1 \cos\theta_2}{M_Z} \\
\frac{\partial x_j}{\partial E_i} &= \left(\frac{\partial x_j}{\partial x_Z}\right)\left(\frac{\partial x_Z}{\partial E_i}\right) + \left(\frac{\partial x_j}{\partial M_Z}\right)\left(\frac{\partial M_Z}{\partial E_i}\right) \\
\frac{\partial M_Z}{\partial E_i} &= \frac{M_Z}{2E_i} \\
\frac{\partial x_j}{\partial \varphi_i} &= \left(\frac{\partial x_j}{\partial M_Z}\right)\left(\frac{\partial M_Z}{\partial \varphi_i}\right) \\
\frac{\partial M_Z}{\partial \varphi_1} &= \frac{E_1E_2}{M_Z}(\sin\theta_1 \sin\theta_2 \sin(\varphi_1 - \varphi_2))
\end{aligned}$$

The calculation of the rest of the derivatives is straightforward, and they only differ from the ones presented here in a minus sign in most of the cases. The following values were used to estimate the error:

$$\begin{aligned} \frac{\sigma(E)}{E} &= \frac{13\%}{\sqrt{E}} + 0.5\% \\ \sigma(\theta) &= \frac{\sin^2\theta}{R_1}\delta z \\ \sigma(\varphi) &= \frac{\delta x}{R_2} \end{aligned} \qquad \text{where} \qquad \begin{aligned} R_1 &= 29.872 \text{ cm} \\ \delta z &= 1.23 \text{ cm} \\ \delta x &= 0.743 \text{ cm} \\ R_2 &= 91.68 \text{ cm} \end{aligned}$$

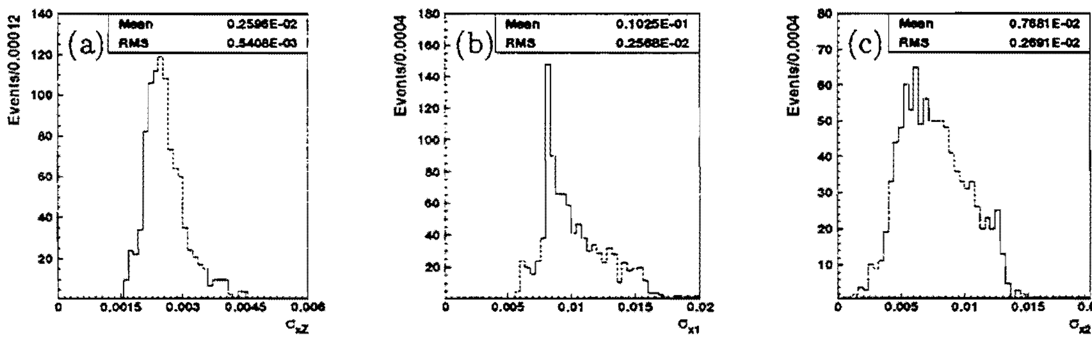

Figure 6.2: Measured error distribution of (a) x_Z, (b) x_1 and (c) x_2 using 1a data.

- R_1 is the distance between the average value of the center of gravity of the CDC tracks and the average value of the center of the EM shower, measured by the electromagnetic calorimeter.
- δz corresponds to the position resolution of the vertex for two electrons, using the CD and CAL information reported in [50].
- δx is the position resolution for CAL hits reported also in [50].
- R_2 is the distance between the average value of the center of the shower in the electromagnetic calorimeter and the beam.

Using the data sample described in section 6.1 we assigned to each data point the error calculated as described above. The resulting distributions are shown in Fig. 6.2.

6.3 MC Smearing

NYU Fast MC and ISAJET events (see sections 4.1 and 4.2) were used to obtain the smearing functions. The difference between the value of x_k smeared and x_k unsmeared ($k = 1, 2, 3$), was calculated for each event in the sample, and then the distribution of these differences was plotted as a function of x_k ($k = 1, 2, 3$), for both ISAJET and Fast MC. Fig. 6.3 shows the Fast MC distributions and Fig. 6.4 shows the ISAJET distributions. The mean values of the error obtained by direct error calculation (see section 6.2) are in good agreement with both ISAJET and Fast MC fitted sigma values. The error is so small that it is questionable whether smearing causes any significant change in the shape of the $Z \to e^+e^-$ cross section as a function of x_1, x_2, or x_Z.

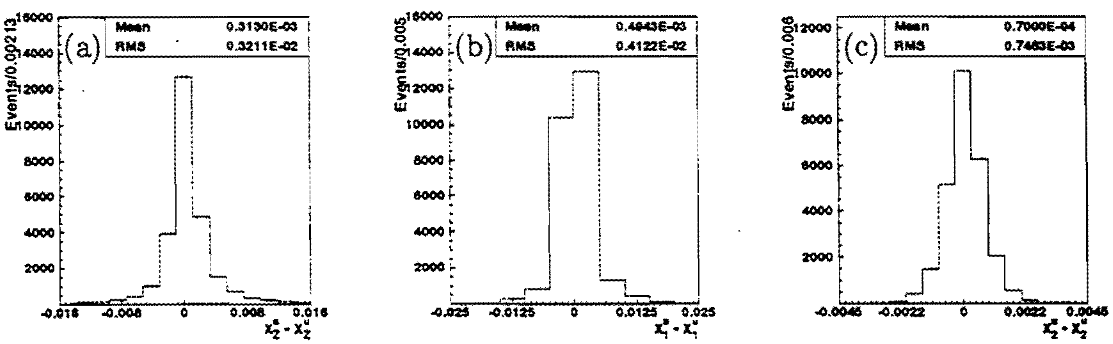

Figure 6.3: Fast MC distribution of the differences between smeared and unsmeared values of (a) x_Z, (b) x_1 and (c) x_2 using Fast MC generated events.

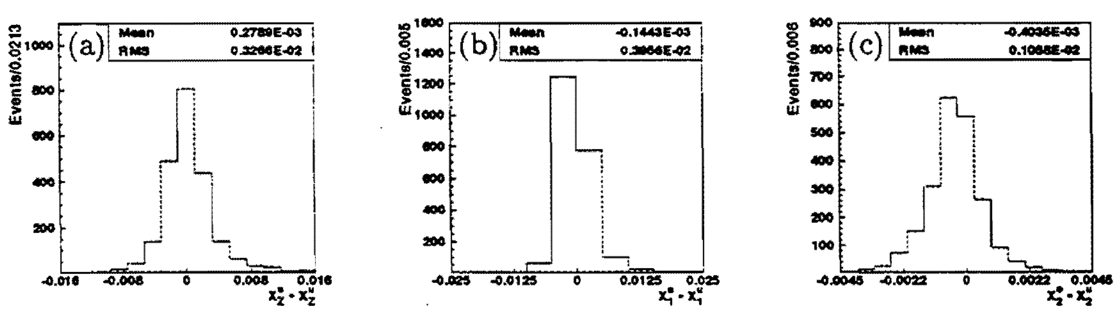

Figure 6.4: Distribution of the differences between the smeared and unsmeared values of (a) x_Z, (b) x_1 and (c) x_2 using ISAJET MC generated events.

6.4 Bias due to smearing effects

Fast MC [29] events were used to estimate the bias due to smearing effects by comparing smeared and unsmeared MC distributions. In order to do so the differences in the bin contents of the histograms of x_k smeared and x_k unsmeared distributions were plotted. In order to avoid a systematic shift due to statistics, the differences were normalized relative to the bin content. The normalization constant for each bin was computed as:

$$\frac{1}{N_{sm}+N_{us}},$$

where N_{sm} is the number of events in the i-th bin of the x_k smeared distribution and N_{us} is the number of events in the i-th bin of the x_k unsmeared distribution (see Fig. 6.5 in the case of $k = z$). The height of the resulting histogram is the difference of the smeared minus unsmeared distributions times the normalization constant, i.e.

$$\frac{N_{sm}-N_{us}}{N_{sm}+N_{us}}.$$

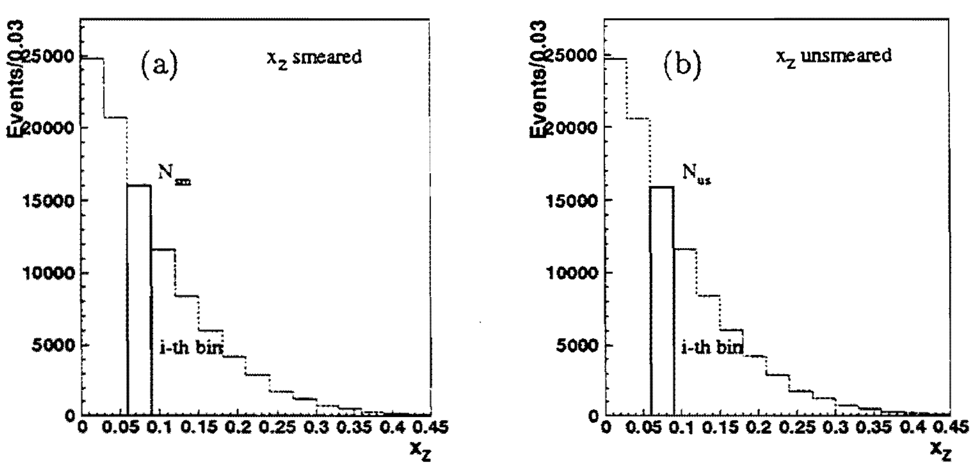

Figure 6.5: Bin content of the (a) x_Z smeared distribution and (b) x_Z unsmeared distribution.

The bin by bin compared histograms for x_Z and x_1 are shown in Fig. 6.6. As a measure of the bias due to smearing effects the histograms were fitted to a straight line. In the case of x_2 two different patterns for the bias were found, in the region $0 < x_2 < 0.045$ the bias is small compared to the bias in the region $0.045 < x_2 < 0.06$, so the histogram was separated into two parts: one corresponding to channels 2 to 11,

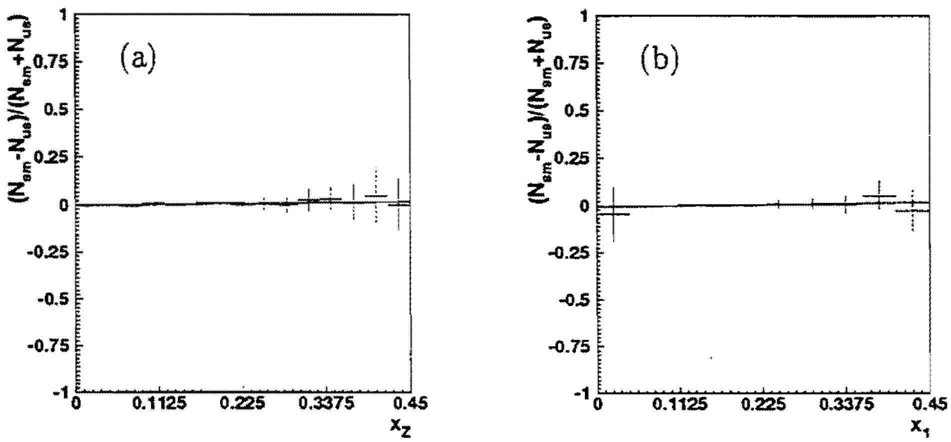

Figure 6.6: Bin content differences normalized relative to the bin content for Fast MC generated events for (a) x_Z smeared and x_Z unsmeared and (b) x_1 smeared and x_1 unsmeared.

and the other to channels 12 to 15. Both fits are shown in Fig. 6.7. The results of the fit are summarized in Table 6.2.

From this result it can be concluded that the bias due to smearing effects is negligible for x_z, x_1 and most of the x_2 distributions. When x_2 falls into the range of $0.045 < x_2 < 0.06$ the bias is quite large so the x_2 cross section in this region should be corrected for smearing effects.

	Constant	Slope
x_Z	-0.00382 ± 0.00680	0.04453 ± 0.06088
x_1	-0.00683 ± 0.00918	0.05984 ± 0.07135
x_2 (Channels (2:11))	-0.00744 ± 0.01204	0.16301 ± 0.45004
x_2 (Channels (12:15))	-1.22498 ± 0.38765	26.94435± 8.26226

Table 6.2: Summary of resolution fitted parameters.

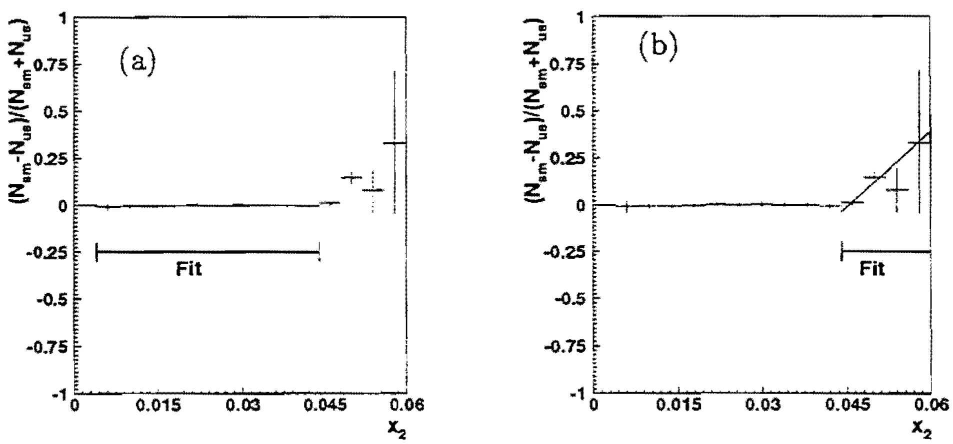

Figure 6.7: Bin content differences normalized relative to the bin content for Fast MC generated events for x_2. (a) Fit using channels 2 to 11. (b) Fit using channels 12 to 15.

6.5 Resolution effects

In section 6.4 a straight line fit to residual distributions of x_Z, x_1 and x_2 (smeared - unsmeared) was used to determine the bias due to smearing effects. This assumption is only valid if the resolution as a function of x_Z, x_1 and x_2 is linear.

In order to plot the resolution as a function of x_k the method described below was used along with the Fast MC sample described in section 4.2.

The $x_k^{\text{small smeared}}$ quantities are plotted, then, for each bin separately, the distributions of $x_k^{\text{small smeared}}$ - $x_k^{\text{small unsmeared}}$ are plotted (see Fig 6.8 when $k = Z$). The bin size was chosen to be small enough to get detailed dependance of the resolution as a function of the x_k quantity and at the same time to be large enough to have sufficient statistics for each bin.

The r.m.s. value of the x_k^{smeared} - $x_k^{\text{unsmeared}}$ distribution is proportional to the x_k resolution of the detector and the mean value of this distribution is proportional to the x_k resolution of the detector and the mean value of this distribution is describing the shift of the x_k cross section due to smearing. Fig. 6.9 shows the mean value and Fig. 6.10 shows the r.m.s. value of x_k^{smeared} - $x_k^{\text{unsmeared}}$ distributions as a function of x_k smeared. The center of each bin of x_k smeared was taken as the mean value of the bin.

From Fig. 6.10 it can be concluded that the x_k resolutions have a more or less linear dependence as a function of x_k, furthermore, from Fig 6.9 it can be seen that the mean values of x_k are also showing a linear dependence of x_k, so it is a reasonable way to quantify the bias due to smearing effects using the method described in section 6.4.

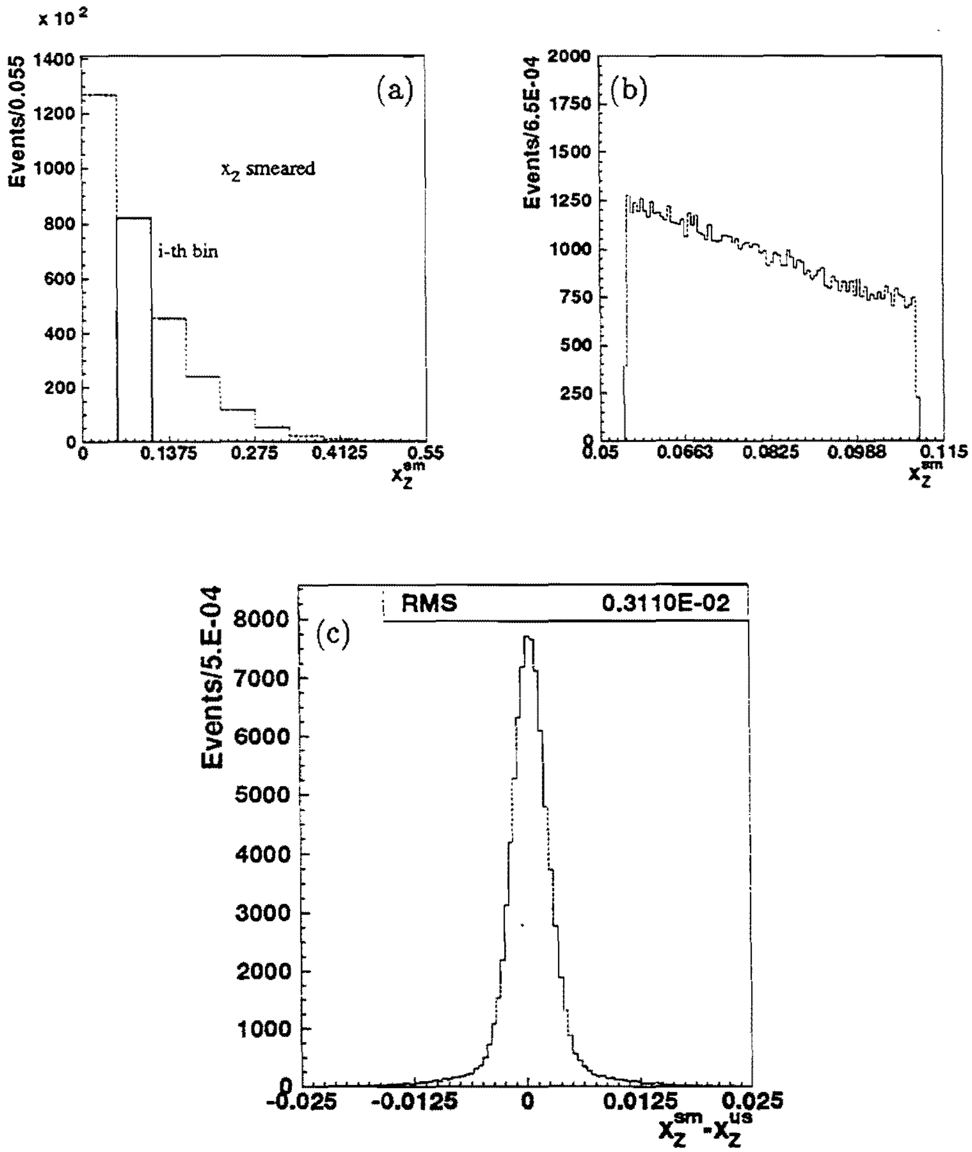

Figure 6.8: (a) Arbitrary binning of x_Z^{smeared} distribution. (b) The i-th bin of the x_Z^{smeared} distribution. (c) Difference between x_Z^{smeared} and $x_Z^{\text{unsmeared}}$ for the i-th bin of the x_Z^{smeared} distribution.

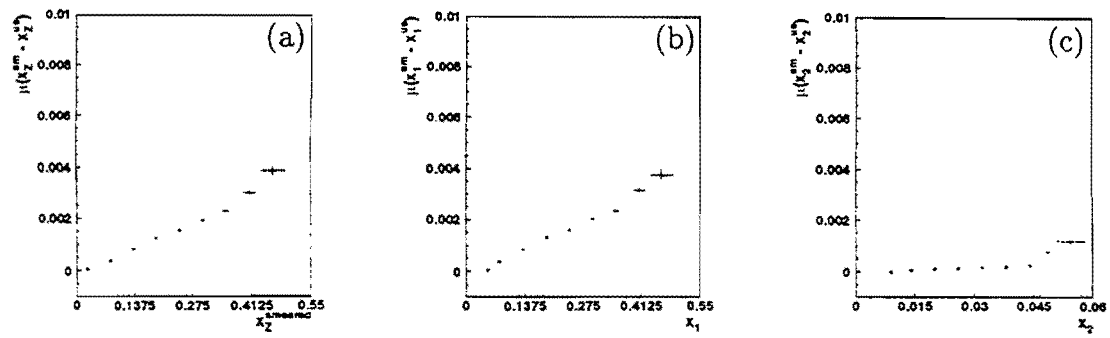

Figure 6.9: Bias versus x^{smeared}. (a) x_Z, (b) x_1 and (c) x_2.

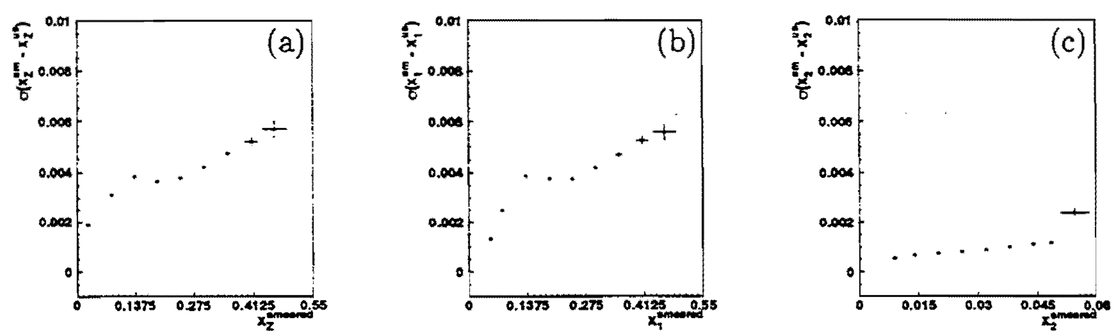

Figure 6.10: Resolution versus x^{smeared} . (a) x_Z, (b) x_1 and (c) x_2.

6.6 Systematic errors

In section 6.4 MC samples were used to estimate the bias due to smearing. If the smearing part of the MC is not a faithful representation of the DØ detector, it might have introduced a systematic error in the estimate.

In order to estimate the systematic error due to model dependence several Fast MC (see section 4.2) samples were generated with different values of the constant and sampling parameters (C and S respectively), of the energy resolution function: $\frac{\sigma(E)}{E} = \frac{S}{\sqrt{E}} + C$. The values of these parameters were varied giving better and worse energy resolutions than the standard one, the values used are shown in table 6.3.

C	S		
0.0015	0.013	1/10 times the standard values	(A)
0.0075	0.065	0.5 times the standard values	(B)
0.015	0.13	Standard values	Standard
0.03	0.26	Twice the standard values	(C)
0.15	1.3	10 times the standard values	(D)

Table 6.3: Summary of constant and sampling parameters used to generate samples with different energy resolutions.

From now on, these samples will be referred to as *standard, A, B, C,* and *D* samples. The method described in section 6.4 was applied to these samples, i.e. subtract in a bin by bin basis the smeared and unsmeared x distributions, normalizing the difference to the sum of the events in the bin for both distributions and fitting the resulting histogram to a straight line. The results of the fits are summarized in Table 6.4.

The key numbers in this Table are the slopes, the larger the slope, the larger the smearing. In Table 6.4 the "Fractional variation" (FV) is introduced. FV was calculated as 100 times the product of the slope times the range in x used in the fit; the "error" in the fractional variation was calculated as 100 times the product of the error in the slope times the range in x used in the fit. The FV is a good measure of the shape change of the x_k distributions along the entire range of x_k. It can be seen from Table 6.4 that the general tendency of the dependence of the FV with the resolution function is as expected. Better resolution gives smaller FV and viceversa. Furthermore, the value of the FV is in the range of a 2% for the A, B and C samples, which means that if our uncertainty determining the resolution is 100% we would be introducing still a 2% systematic error, so the measurement is not sensitive to model dependence.

As it can be seen from Table 6.4, the fractional variation in the range from 0.044 to 0.06 in x_2 for samples C and D is larger than 100%, this is due to the fact that the behaviour of the residual distribution is not linear, as it can be seen in figure 6.11.

x_Z									
Sample	Constant			Slope			Frac. variation		
A	-0.00419	±	0.00675	0.04873	±	0.06020	2.193	±	2.709 %
B	-0.00372	±	0.00682	0.04359	±	0.06127	1.962	±	2.757 %
Standard	-0.00382	±	0.00680	0.04453	±	0.06088	2.004	±	2.740 %
C	-0.00333	±	0.00682	0.03859	±	0.06070	1.737	±	2.731 %
D	-0.01442	±	0.00848	0.15940	±	0.07299	7.173	±	3.285 %
x_1									
Sample	Constant			Slope			Frac. variation		
A	-0.00663	±	0.00911	0.05759	±	0.07055	2.591	±	3.175 %
B	-0.00658	±	0.00924	0.05821	±	0.07194	2.611	±	3.237 %
Standard	-0.00683	±	0.00918	0.05984	±	0.07135	2.693	±	3.211 %
C	-0.00713	±	0.00920	0.06258	±	0.07105	2.816	±	3.197 %
D	-0.01979	±	0.01123	0.19543	±	0.08452	8.794	±	3.803 %
x_2 (Channels (2:11))									
Sample	Constant			Slope			Frac. variation		
A	-0.00692	±	0.01194	0.18629	±	0.44629	0.745	±	1.785 %
B	-0.01041	±	0.01210	0.33686	±	0.45318	1.347	±	1.813 %
Standard	-0.00744	±	0.01204	0.16301	±	0.45004	0.652	±	1.800 %
C	-0.00647	±	0.01207	0.16447	±	0.45176	0.658	±	1.807 %
D	-0.02306	±	0.01434	0.45884	±	0.54922	1.835	±	2.197 %
x_2 (Channels (12:15))									
Sample	Constant			Slope			Frac. variation		
A	-1.07962	±	0.39601	23.62210	±	8.45486	37.795	±	13.534 %
B	-1.29295	±	0.40102	28.09667	±	8.55925	44.955	±	13.695 %
Standard	-1.22498	±	0.38765	26.94435	±	8.26226	43.111	±	13.220 %
C	-2.96921	±	0.36528	63.82445	±	7.76440	102.119	±	12.423 %
D	-4.69190	±	0.21658	101.07860	±	4.40617	161.726	±	7.05 %

Table 6.4: Summary of fitted parameters for the bias due to the smearing for different energy resolutions.

Fitting a straight line is inappropriate, in this range of x_2 the fractional variation was estimated in the following way: instead of using the slope times the x_2 range, the value of x_2^{smeared} - $x_2^{\text{unsmeared}}$ of the last bin in x_2 was directly multiplied by 100 and subtracted the value of the FV calculated for the range of x_2 from 0.004 to 0.044 (bins 2-11). Table 6.5 shows the fractional variation for the range from 0.044 to 0.06 in x_2 for samples C and D.

To have a better understanding of the effect of the energy smearing, another set of Fast MC samples was generated with the same parameters of Table 6.3 but this time the angular resolution in the Fast MC was turned off and the exercise was repeated as explained above. The results of the fits are summarized in Table 6.6.

Again, the fractional variation for the last 3 channels of x_2 for sample D was re-

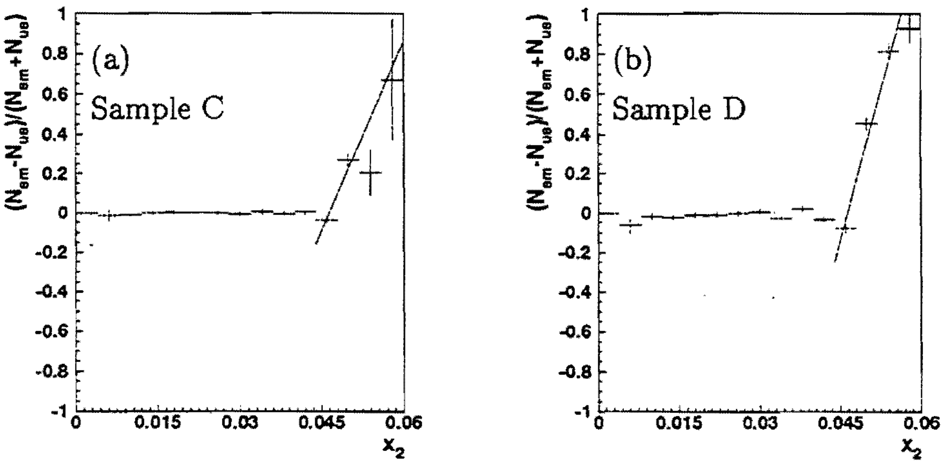

Figure 6.11: Normalized difference of x_2 smeared and x_2 unsmeared from (a) sample C and (b) sample D. Note the non-linear behaviour of the distributions in the upper range of x_2.

x_2 (Channels (12:15))	
Sample	Frac. variation
C	66.56 $\pm$ 30.34 %
D	93.05 $\pm$ 7.59 %

Table 6.5: Recalculated fractional variation for channels 12 to 15 of x_2 for samples C and D.

calculated as explained above. The recalculated fractional variation is shown in table 6.7.

In tables 6.6 and 6.7 it can be seen the same behaviour of the fractional variation as in the previous case. Comparing table 6.4,6.6 it can be seen that there is no considerable effect from turning off the angular resolution, since the values for the fractional variation agree (within the errors) in both tables.

x_Z									
Sample	Constant			Slope			Frac. variation		
A	-0.00391	±	0.00675	0.04506	±	0.06003	2.028	±	2.701 %
B	-0.00454	±	0.00675	0.05255	±	0.06003	2.365	±	2.701 %
Standard	-0.00436	±	0.00692	0.04918	±	0.06009	2.213	±	2.704 %
C	-0.00425	±	0.00683	0.04886	±	0.06094	2.199	±	2.742 %
D	-0.01627	±	0.00844	0.17597	±	0.07100	7.919	±	3.195 %
x_1									
Sample	Constant			Slope			Frac. variation		
A	-0.00737	±	0.00908	0.06461	±	0.07023	2.907	±	3.160 %
B	-0.00834	±	0.00909	0.07283	±	0.07012	3.277	±	3.155 %
Standard	-0.00681	±	0.00922	0.05837	±	0.06993	3.627	±	3.147 %
C	-0.00745	±	0.00922	0.06501	±	0.07139	2.925	±	3.213 %
D	-0.03007	±	0.01112	0.25729	±	0.08214	11.606	±	3.696 %
x_2 (Channels (2:11))									
Sample	Constant			Slope			Frac. variation		
A	-0.00673	±	0.01196	0.15673	±	0.44689	0.627	±	1.788 %
B	-0.00621	±	0.01190	0.13282	±	0.44524	0.531	±	1.781 %
Standard	-0.00625	±	0.01212	0.13865	±	0.45626	0.555	±	1.825 %
C	-0.00675	±	0.01207	0.18639	±	0.45199	0.746	±	1.808 %
D	-0.03213	±	0.01427	0.91474	±	0.54746	3.659	±	2.190 %
x_2 (Channels (12:15))									
Sample	Constant			Slope			Frac. variation		
A	-1.11072	±	0.40380	24.41878	±	8.62031	38.638	±	13.793 %
B	-0.94636	±	0.38226	20.88608	±	8.14291	33.118	±	13.029 %
Standard	-1.53354	±	0.39564	33.39994	±	8.42886	53.139	±	13.486 %
C	-2.23303	±	0.36702	48.08432	±	7.80482	76.935	±	12.488 %
D	-5.86742	±	0.22956	125.56000	±	4.66755	200.896	±	7.468 %

Table 6.6: Summary of resolution fitted parameters (angular resolution turned off).

x_2 (Channels (12:15))			
Sample	Frac. variation		
D	88.63	±	4.2 %

Table 6.7: Recalculated fractional variation for channels 12 to 15 of x_2 for sample D.

6.7 Summary of the resolution studies

Using measured detector resolutions the resolutions for the variables x_Z, x_1 and x_2 were directly derived and compared them to the calculated resolutions from MC. The resolution directly derived agrees within the error with the resolution calculated with MC.

The bias due to smearing effects was studied by using MC and it was found that it is negligible for most of the range of x_Z, x_1 and x_2. Finally, the systematic error due to model dependence on the MC was studied by varying the parameters of the resolution function used to simulate the smearing of the detector. It was found that the effect of the smearing is quite small relative to other errors so there is no need for unsmearing the data in the measurements of the longitudinal momentum of the Z boson.

Chapter 7

Overall efficiencies

Research is what I'm doing when I don't know what I'm doing.

Wernher Von Braun.

The data selection procedure is not 100 % efficient in the sense that a fraction of the real electrons could be rejected by the data selection process: for instance, if a shower fluctuates in the calorimeter, it could be later rejected by the isolation cut. This underestimation of the data sample can lead to variations in the shape of the x distributions.

The data sample used for this analysis is the same as the one used in the measurement of the $Z \rightarrow ee$ cross section, then, the efficiencies calculated in [45] will be used for the present analysis. The measurement of the efficiencies and their effects on the measurement of the x distributions are explained in the following chapter.

7.1 Method

The efficiency of a cut a relative to a (looser) cut b is given by:

$$\epsilon_{AB} = \frac{N_{AB}}{N_B} \tag{7.1}$$

where N_{ab} and N_b are the number of events which pass cuts a and b tohgether and cut b alone, respectively.

In order to accurately measure the efficiencies, it is important to have a sample with the following characteristics:

- clean, i.e. containing the smallest possible amount of background,

- unbiased, i.e. selected with a minimum of cuts, and the cuts should not be correlated with the ones which efficiencies are being measured.

This sample is called a diagnostic sample. The diagnostic sample used to measure the efficiency of the $Z \to e^+e^-$ selection cuts was selected requiring tight electron identification criteria to one of the electrons of each event in the Z sample and by requiring an invariant mass of the pair close to the actual mass of the Z boson (91 GeV). It has been proved [53, 54] that a Z sample selected in this way fulfills the characteristics described above. The measurement of the efficiency is limited by the size of the sample as well as by the uncertainty in the determination of the background, which will produce a systematic uncertainty in the efficiencies.

7.2 Selection of the diagnostic data sample

The diagnostic data sample was selected from the $Z \to e^+e^-$ data sample (see section 3.4), requiring each event passing EM2_EIS_ESC L2-filter; this filter requires two EM clusters, one of which is isolated and has a transverse energy $E_T^{L2} > 20$ GeV, and the other has $E_T^{L2} > 16$ GeV. In addition, the two electrons must be contained within the standard fiducial region of the detector. After this preselection, tagging cuts are applied on one of the electrons:

- EM fraction $f_{\rm EM} > 0.95$.
- Isolation fraction $f_{\rm iso} < 0.15$.
- H-Matrix $\chi^2 < 100$.
- A track with $S_{\rm trk} < 5(10)$ in the CC (EC).

if an electron passes this tagging cuts, the vertex is recalculated (see section 3.3.1), both electrons are required to have transverse eneregy $E_T > 25$ GeV, and the invariant mass is required to be close to the Z boson mass ($M_Z = 91.2$ GeV/c^2). This tagging procedure is applied to both EM clusters, thus, if both electrons are tagged the event is counted twice.

7.3 Background determination

To estimate the uncertainty due to background subtraction, four methods are used to estimate the background:

1.) Side band method. Two sideband regions are defined outside the signal region $86 < M_{ee} < 96$ GeV/c^2, the lower sideband comprises the region $60 < M_{ee} < 70$ GeV/c^2, while the upper sideband region comprises $110 < M_{ee} < 120$ GeV/c^2.

The number of background events is taken to be the average of the two sideband regions.

2.) Same as 1.) but with a signal region defined as $81 < M_{ee} < 101$ GeV/c^2, and in this case, the number of background events is taken as the sum of the two sideband regions.

3.) The invariant mass spectrum is fitted to a Breit-Wigner convoluted with a gaussian (which accounts for the resolution in the measurement) and a linear background in the region $70 < M_{ee} < 110$ GeV/c^2. The linear parameters are used to estimate the number of events that must be subtracted. the signal region is taken from $86 < M_{ee} < 96$ GeV/c^2.

4.) Same as 3.) but with a signal window $86 < M_{ee} < 96$ GeV/c^2.

Figure 7.1 illustrates the sideband and the fit techniques.

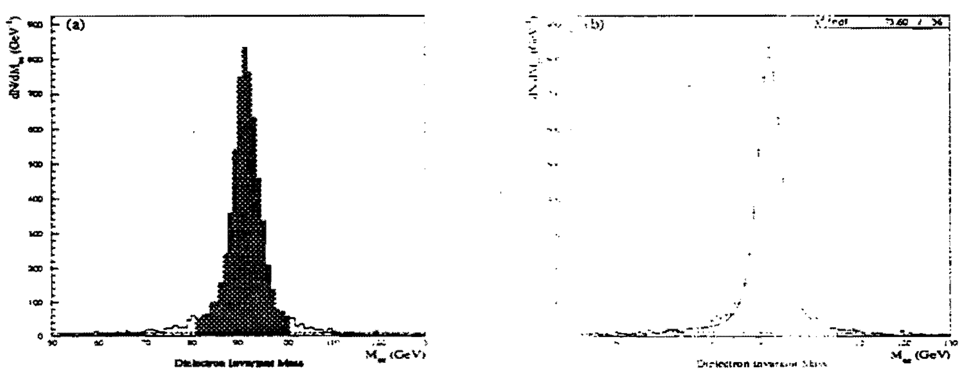

Figure 7.1: Background subtraction methods used to estimate the efficiency. (a) The sideband method and (b) the fit method [26, p. 139].

7.4 Single electron efficiencies

Single electron efficiencies are estimated by imposing different cuts on the probe electrons, each cut defines an electron class:

- Probe electron: an electron which passes L2 *esc16* filter. All other cuts are measured relative to this cut.
- Trigger electron: a probe electron which passes L2 *eis20* filter.

- Track electron: a trigger electron which passes the tracking requirement.
- Loose electron: a trigger electron which passes calorimetric identification criteria.
- Tight electron: a lose electron that is also a track electron.

With the previous definitions three relative efficiencies are measured:

$$\text{Level-2 trigger efficiency} \quad \epsilon_{L2} \equiv \frac{\#\ \text{Trigger electrons}}{\#\ \text{Probe electrons}}$$

$$\text{Calorimeter ID efficiency} \quad \epsilon_{cal} \equiv \frac{\#\ \text{Loose electrons}}{\#\ \text{Trigger electrons}}$$

$$\text{Tracking efficiency} \quad \epsilon_{trk} \equiv \frac{\#\ \text{Tight electrons}}{\#\ \text{Loose electrons}}$$

7.5 Level 0 efficiency

The requirements of the Level 0 trigger, that a hit must be recorded in each of the Level 0 counters, and the result of the calculation of the fast z must be consistent with $|z_{\text{vtx}}| < 96.875$ cm, imposes a minimum bias requirement on all events. During Run 1b the Level 0 trigger logic was modified to allow a measurement of the Level 0 trigger efficiency; $W \to e\nu$ events passing the trigger (EM1_EISTRKCC_MS) were no longer required to fire the Level 0 trigger, althoung the decision was saved with the event.

Using a W sample selected with the standard cuts [26, Section 4.2], but the Level 0 requirement removed it is possible to estimate the Level 0 efficiency since Level 0 efficiency can be expressed as [11, p. 106]:

$$\varepsilon_{\text{L}\emptyset}(W) = \sum_{n=0}^{\infty} \varepsilon_{\text{L}\emptyset}(W+n) \cdot P(n) \tag{7.2}$$

where $\varepsilon_{\text{L}\emptyset}(W)$ is the overall Level 0 efficiency for W events, $\varepsilon_{\text{L}\emptyset}(W+n)$ is the Level 0 efficiency for a W event with n minimum bias events and $P(n)$ is the probability for a W event with n minimum bias event to ocurr. This probability must be taken into account since any additional interaction will increase the probability of firing the Level 0 system. Assuming $\varepsilon_{\text{L}\emptyset}(W+n) = 1$ for $n \geq 2$ and applying $\sum_n P(n) = 1$,

$$\varepsilon_{\text{L}\emptyset}(W) = \varepsilon_{\text{L}\emptyset}(W+0) \cdot P(0) - \varepsilon_{\text{L}\emptyset}(W+1) \cdot P(1)(1 - P(0) - P(1)) \tag{7.3}$$

taking the number of vertices found in the central traking system as the number of interactions it is possible to measure $P(0)$ and $P(1)$, and using the W sample without the Level 0 requirement $\varepsilon_{\text{L}\emptyset}(W+n)$ can be measured. These numbers are then corrected to take into account the presence of halo events: inserting the corrected quantitues in equation 7.3, it is found that[1]:

$$\varepsilon_{\mathrm{L}\emptyset} \equiv \varepsilon_{\mathrm{L}\emptyset}(W) = \varepsilon_{\mathrm{L}\emptyset}(Z) = 0.98 \pm 0.01 \tag{7.4}$$

7.6 Overall Z selection efficiency

Since the selection of a Z boson event requires two electrons which can be in any of the cryostats of the calorimeter, and each cryostat has a different efficiency, there are three Z electron selection efficiencies defined as follows:

$$\begin{aligned}
\epsilon^Z_{ele}\text{CC-CC} &= (\epsilon^c_l)^2 \cdot [2\epsilon^c_t - (\epsilon^c_t)^2] && (7.5)\\
\epsilon^Z_{ele}\text{CC-EC} &= \epsilon^c_l \cdot \epsilon^e_l \cdot (\epsilon^c_t + \epsilon^e_t - \epsilon^c_t \cdot \epsilon^e_t) && (7.6)\\
\epsilon^Z_{ele}\text{EC-EC} &= (\epsilon^e_l)^2 \cdot [2\epsilon^e_t - (\epsilon^e_t)^2] && (7.7)
\end{aligned}$$

where ϵ^c_l and ϵ^c_t are the loose and tight efficiencies for the central electrons and ϵ^e_l and ϵ^e_t are the corresponding efficiencies for the forward electrons. The interpretation of equation 7.5 is as follows: the product of $(\epsilon^c_l)^2$ and $2\epsilon^c_t$ is the probability of having two electrons, one of which has a track; the factor 2 accounts the two possibilities of selecting one loose and one tight electron: the second term corrects for the double counting of the probability of having two tight electrons. Equation 7.7 can be interpreted in the same manner as 7.5, since again, both electrons are in the same cryostat. In the case of equation 7.6, it is necessary to take into account the different possibilities of selecting one tight electron and one loose electron, while each of them can be in the central or forward part of the detector.

The Z electron efficiencies are [23]:

$$\begin{aligned}
\epsilon^Z_{ele}(\mathrm{CC-CC}) &= 79.294 \pm 0.620 \pm 1.019\ (1.193)\% && (7.8)\\
\epsilon^Z_{ele}(\mathrm{CC-EC}) &= 74.723 \pm 0.600 \pm 0.713\ (0.931)\% && (7.9)\\
\epsilon^Z_{ele}(\mathrm{EC-EC}) &= 69.442 \pm 1.083 \pm 0.521\ (1.202)\% && (7.10)
\end{aligned}$$

The first error quoted is statystical, the second is systematic and the number in parenthesis is the sum in quadrature of the two errors. The overall Z selection efficiency used to correct the x distributions is taken as the product of Level 0 efficiency and the Z electron efficiencies (using the combined error):

$$\begin{aligned}
\epsilon^Z(\text{CC-CC}) &= 77.71 \pm 1.41\% && (7.11)\\
\epsilon^Z(\text{CC-EC}) &= 73.23 \pm 1.18\% && (7.12)\\
\epsilon^Z(\text{EC-EC}) &= 68.05 \pm 1.37\% && (7.13)
\end{aligned}$$

[1]Given the smaller Z sample, and the similarity in the underlying events in the W and Z boson production, the Level 0 efficiency measured using the W sample is used also as the Level 0 efficiency for the Z events.

Chapter 8

Further studies on systematic errors

Not everything that can be counted counts.
and not everything that counts can be counted.

Albert Einstein.

The estimation of the systematic errors involves varying the detector parameteres in the Monte Carlo, one at a time, within its limits and estimating the change in the shape of the x distributions, since there is not an established method to measure the "ammount " of change in the shape of a distribution, the systematic error atributed to each parameter will be estimated as the maximum deviation of the distribution from the central value.

8.1 Vertex position

Although the primary vertex position for each event can be measured with a resolution of 2 cm (see section 3.3.1), the data sample has a broad distribution of the primary vertex (r.m.s. of 27 cm) as shown in figure 8.1.

Varying the mean position of the z vertex in CMS Monte Carlo simulations (see section 4.3), several x distributions were generated and compared to estimate the magnitude of variations in the shape of the distributions. The position of the vertex was varied up to one sigma from the nominal value of the vertex $z = 0$. The chosen values for the vertex were $z =$ -30,-20,-10,-5,0,5,10,20 and 30 cm, and the normalized difference (see section 6.4) of each distribution was calculated with respect to the distribution for the nominal value of the vertex $z = 0$.

As it can be seen from figures 8.2, 8.3 and 8.4 the shape of the x distributions does not present a noticeable change when varying the position of the vertex. In order to have a quantitative estimation of the systematic error due to changes in the position

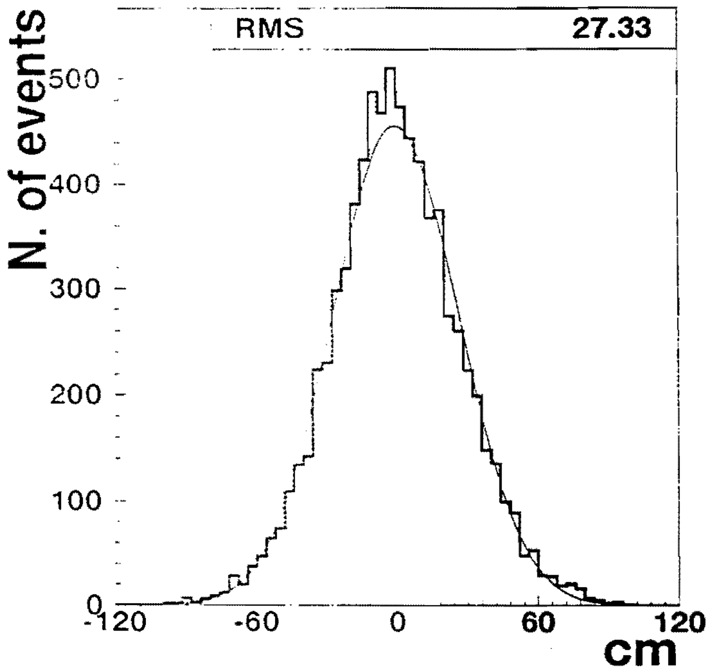

Figure 8.1: Primary vertex distribution.

of the primary vertex a straight line y = constant is fit to each difference, and the absolute value of the largest deviation from $y = 0$ is taken as the systematic error. Table 8.1 contains a summary of the fits.

x_Z	
vtx position	y
vtx = -30	-0.01243
vtx = -20	-0.00599
vtx = -10	-0.00119
vtx = -5	-0.00045
vtx = 5	0.00099
vtx = 10	-0.00149
vtx = 20	-0.00605
vtx = 30	-0.01118

x_1	
vtx position	y
vtx = -30	-0.01246
vtx = -20	-0.00600
vtx = -10	-0.00119
vtx = -5	-0.00046
vtx = 5	0.00098
vtx = 10	-0.00148
vtx = 20	-0.00605
vtx = 30	-0.01120

x_2	
vtx position	y
vtx = -30	-0.01229
vtx = -20	-0.00590
vtx = -10	-0.00116
vtx = -5	-0.00043
vtx = 5	0.00103
vtx = 10	-0.00151
vtx = 20	-0.00600
vtx = 30	-0.01108

Table 8.1: Fit parameter y = constant for the differences between x_Z, X_1 and x_2 distributions generated with several vertex positions relative to the nominal position.

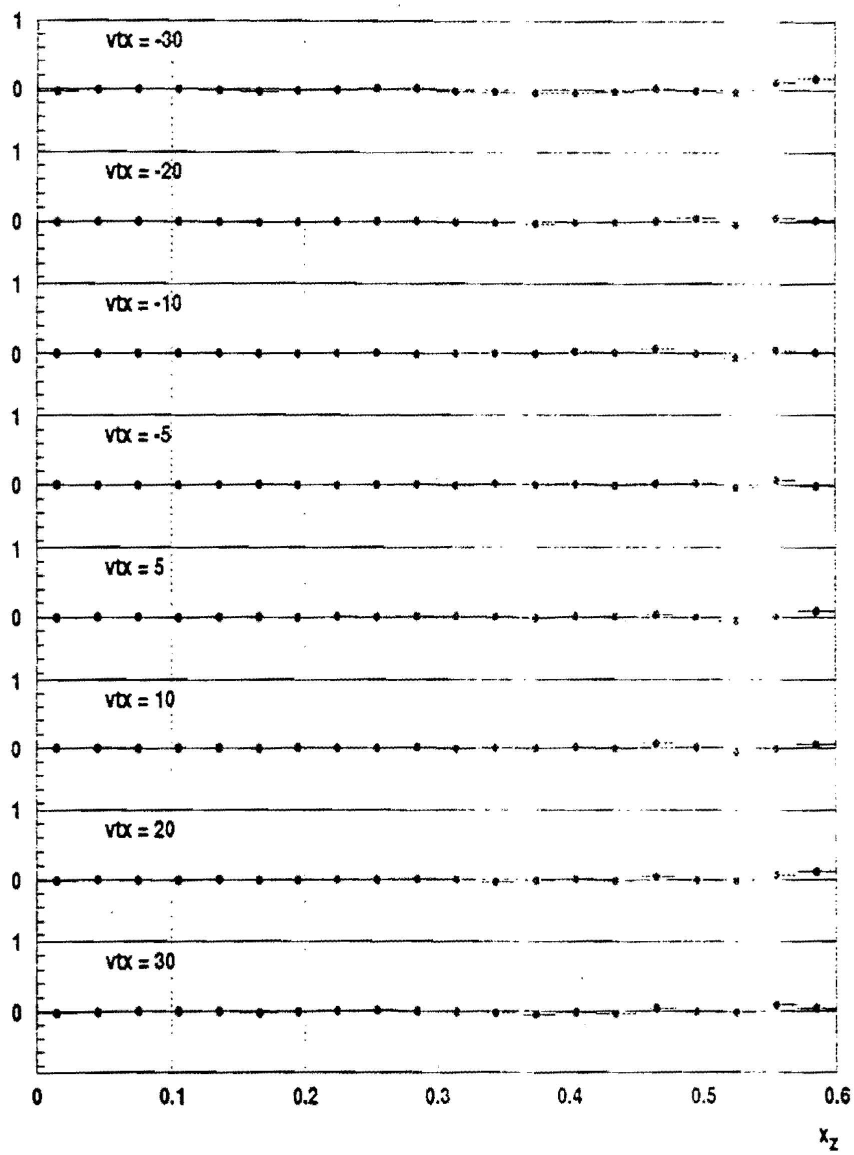

Figure 8.2: Diference between x_Z distributions generated with several vertex positions with respect to the nominal vertex position.

From table 8.1 it also can be seen that the linear fit is a good estimator of the systematic error since the absolute value of y increases as the distance of the vertex is moved away from its nominal value. The systematic error due to changes in the vertex position is taken as 1.2 % for all cases.

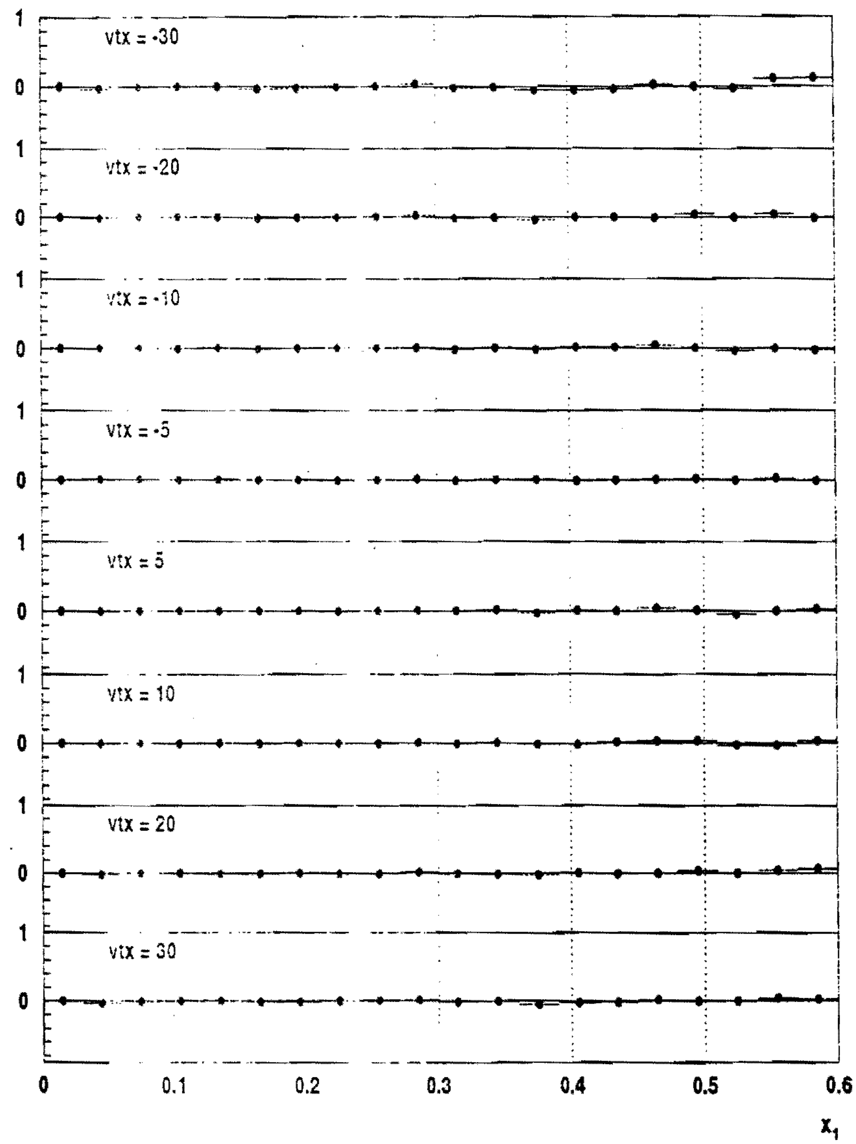

Figure 8.3: Diference between x_1 distributions generated with several vertex positions with respect to the nominal vertex position.

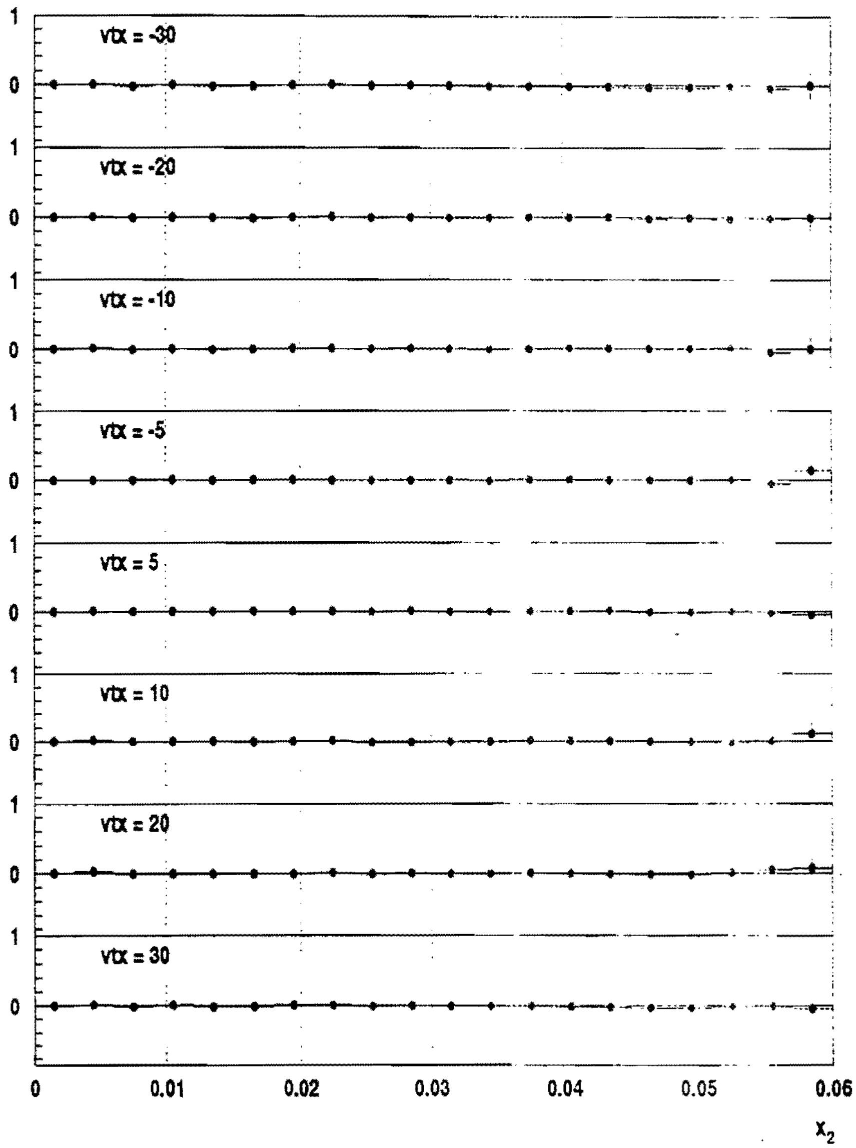

Figure 8.4: Diference between x_2 distributions generated with several vertex positions with respect to the nominal vertex position.

8.2 Tracking efficiency

The single electron traking efficiency was measured [55] and it was found to have the distribution shown in figure 8.5. This distribution has been parametrized using linear fits for the regions $1.5 < |\eta| < 2.5$, and a fifth order polynomial in the central region $|\eta| < 1.1$, and it has been implemented in the CMS Monte Carlo simulation.

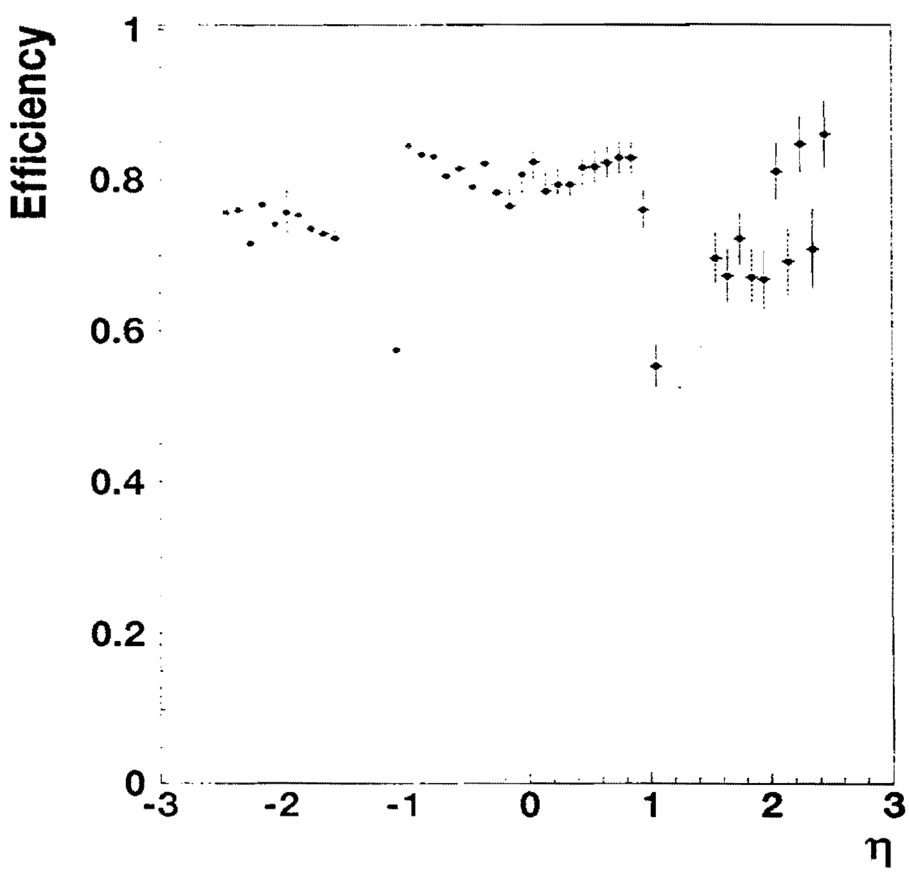

Figure 8.5: Single electron tracking efficency measured from data.

Due to the fact that the data sample is selected by requiring (at least) one track, the tracking efficiency is translated to the distribution shown in figure 8.6. As it can be seen, the distribution flattens due to the fact that if the first electron in the pair does not have a track the second electron could have a track and the event is kept. This distribution can be interpreted as the tracking efficiency for the Z event given that (at least) one track is required.

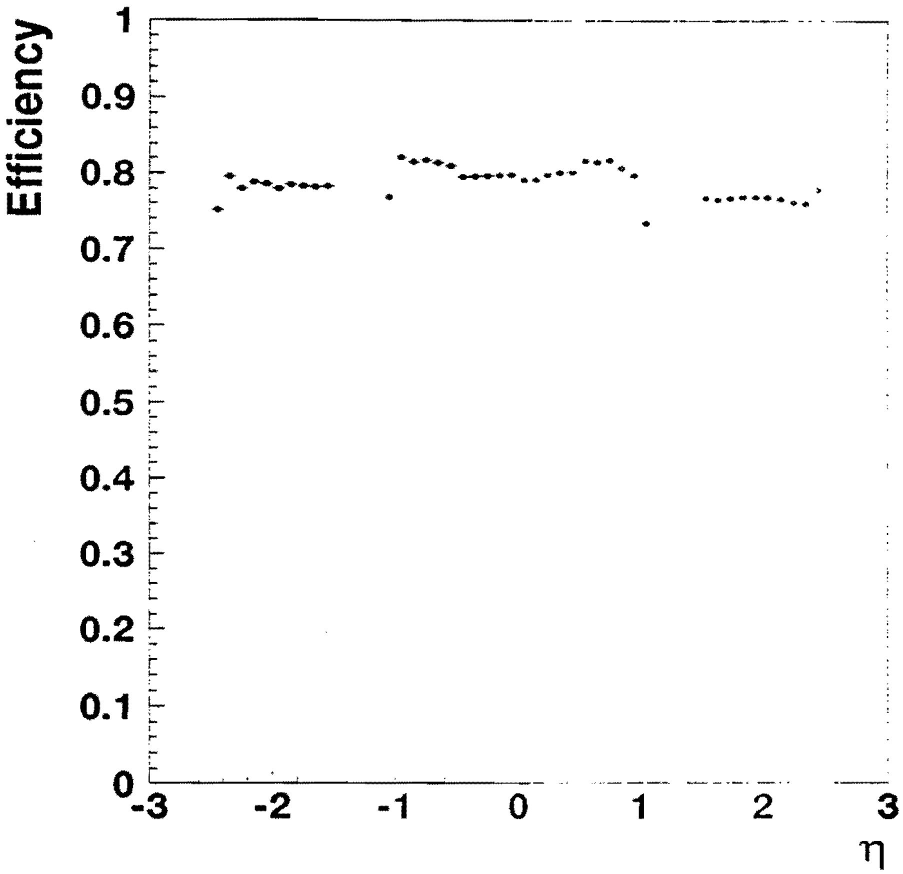

Figure 8.6: Tracking efficency for dielectrons calculated with MC.

To estimate the systematic error introduced by mismeasurement of the tracking efficiency and its implementation in the Monte Carlo, the x distributions with and without tracking efficiency simulation are compared, via its normalized difference (see section 6.4). The differences are shown in figure 8.7. The systematic error is estimated by fitting a straight line y = constant to each of the histograms in figure 8.7. Table 8.2 shows the fit parameters for each x distribution. In the three cases the systematic error is taken as 0.5 %.

x_Z	$y = 0.00046$
x_1	$y = 0.00046$
x_2	$y = 0.00046$

Table 8.2: Fitted constant to the normalized difference of the x distributions with and without the tracking efficienacy simulation.

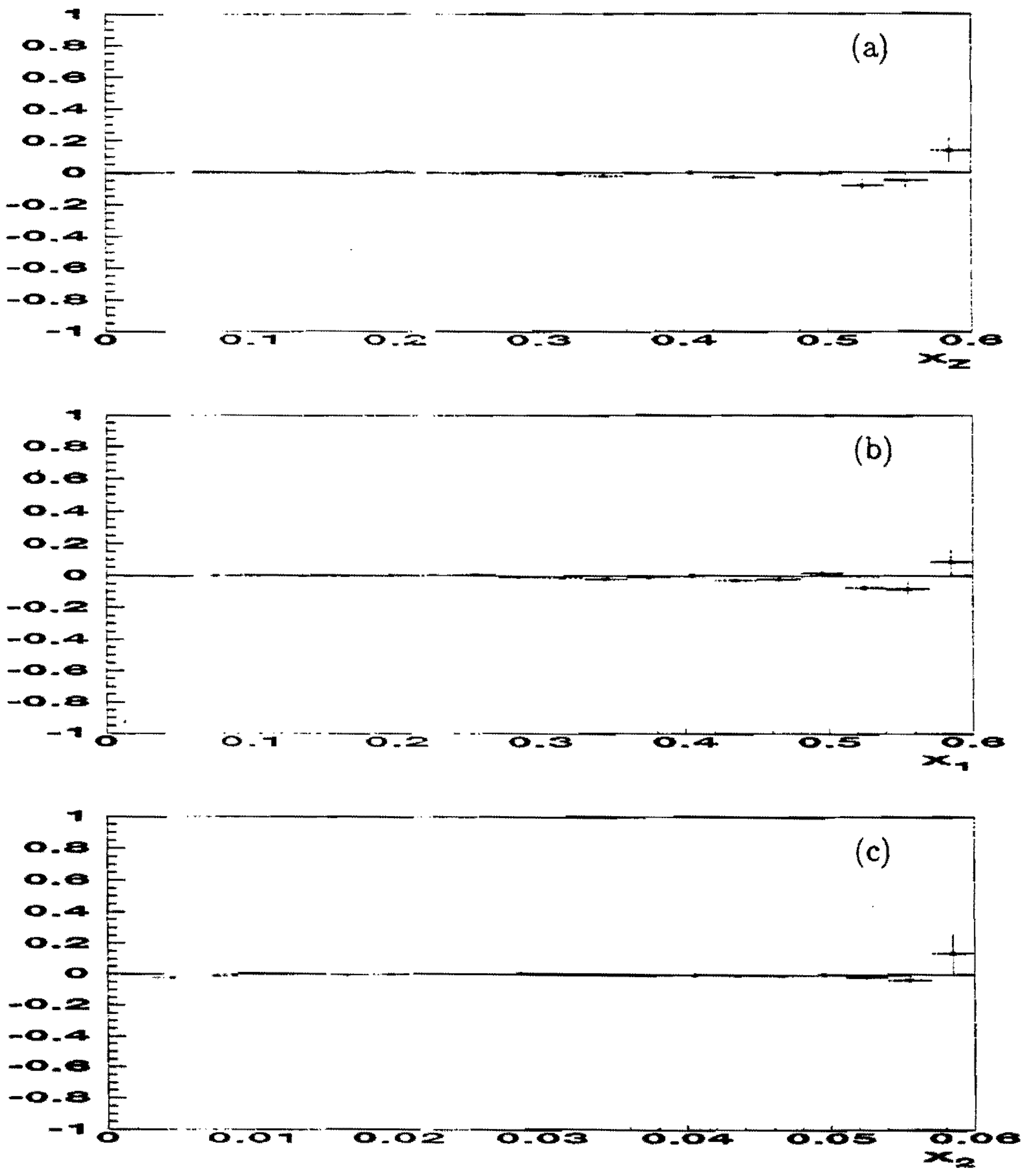

Figure 8.7: Normalized diferences of (a) x_Z, (b) x_1 and (c) x_2 with and without tracking efficiency simulation.

Chapter 9

Results

What most experimenters take for granted
before they begin their experiments
is infinitely more interesting than
any results to which their experiments lead.

Norbert Wiener (1894-1964)

Along the previous chapters there have been described how the data sample was selected from a candidate sample and the effects for which the data sample must be corrected. In this chapter, it will be explained how the overall corrections to the x distributions are applied. Finally, comparison with theoretical prediction will be shown.

9.1 Corrected x distributions

The raw data sample obtained as explained in chapter 3 needs to be corrected in order to be compared with theoretical predictions (Monte Carlo samples). The corrections applied to the raw data sample are as follows: first, the background shapes estimated in section 5.1.4 (figure 5.10) are subtracted from the x distribution shapes shown in figure 3.11, as the fractions indicated in table 5.2. The Drell Yan background shape (figure 5.11) is also subtracted in the proportion indicated in table 5.9. The systematic errors are added in quadrature to the statistical errors before subtracting the background, since the goal of the analysis is to measure the shape of the x distributions the error bars will define a strip which is widened with the systematic errors. The background subtraction process is performed separately for each contribution from the cryostats (CC-CC, CC-EC and EC-EC).

After background subtraction, the three contributions are added up, weighed by the efficiencies measured for each of them (see table 7.1). Finally, the systematic errors calculated in sections 6.6, 8.1 and 8.2 are added in quadrature. The resulting distributions with all errors combined are shown in figure 9.1.

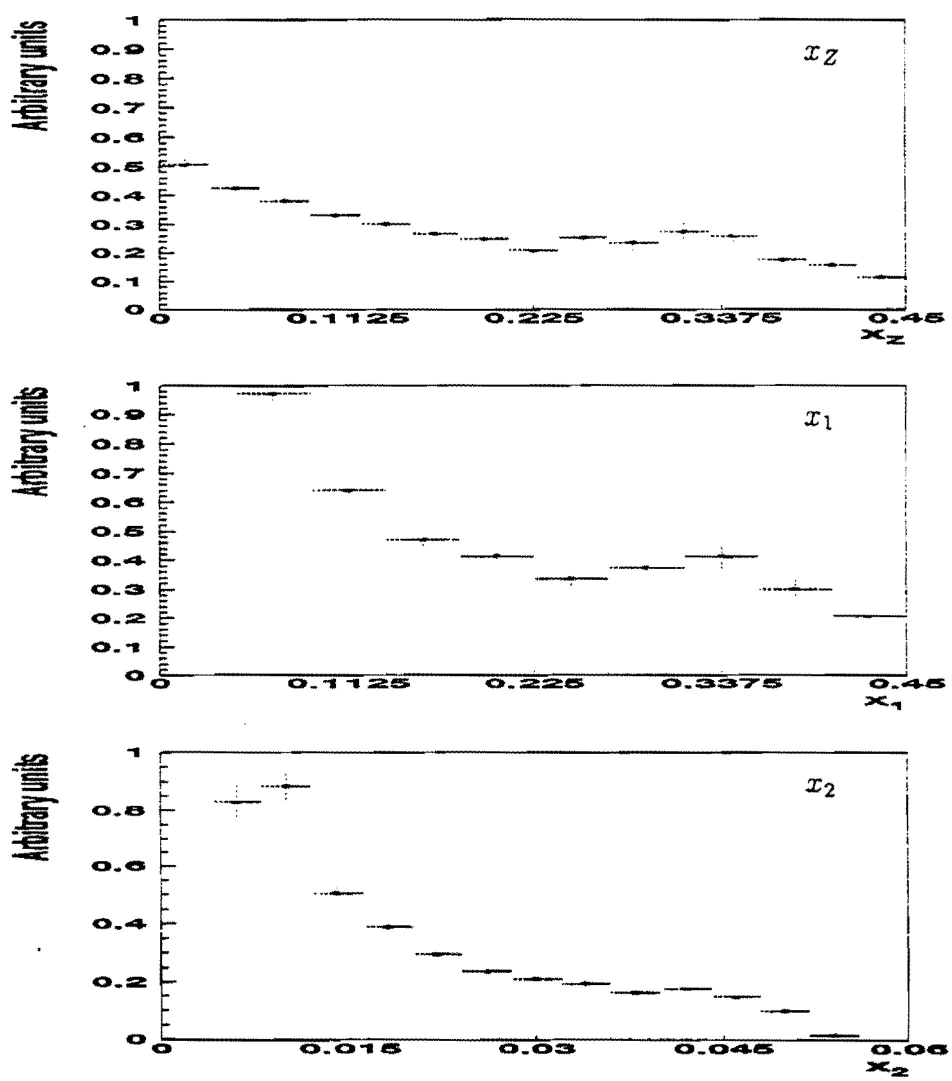

Figure 9.1: x_Z, x_1 and x_2 corrected distributions.

9.2 Comparison with theoretical predictions

Once the x distributions are corrected they can be compared with the theoretical predictions. The comparison is made with Monte Carlo samples generated using different parton distribution functions.

Figure 9.2 shows the x_Z data distribution compared to Monte Carlo x_Z distributions generated using CTEQ2M and HMRSB pdfs. Figure 9.3 shows data compared with CTEQ3M and MRSD-.

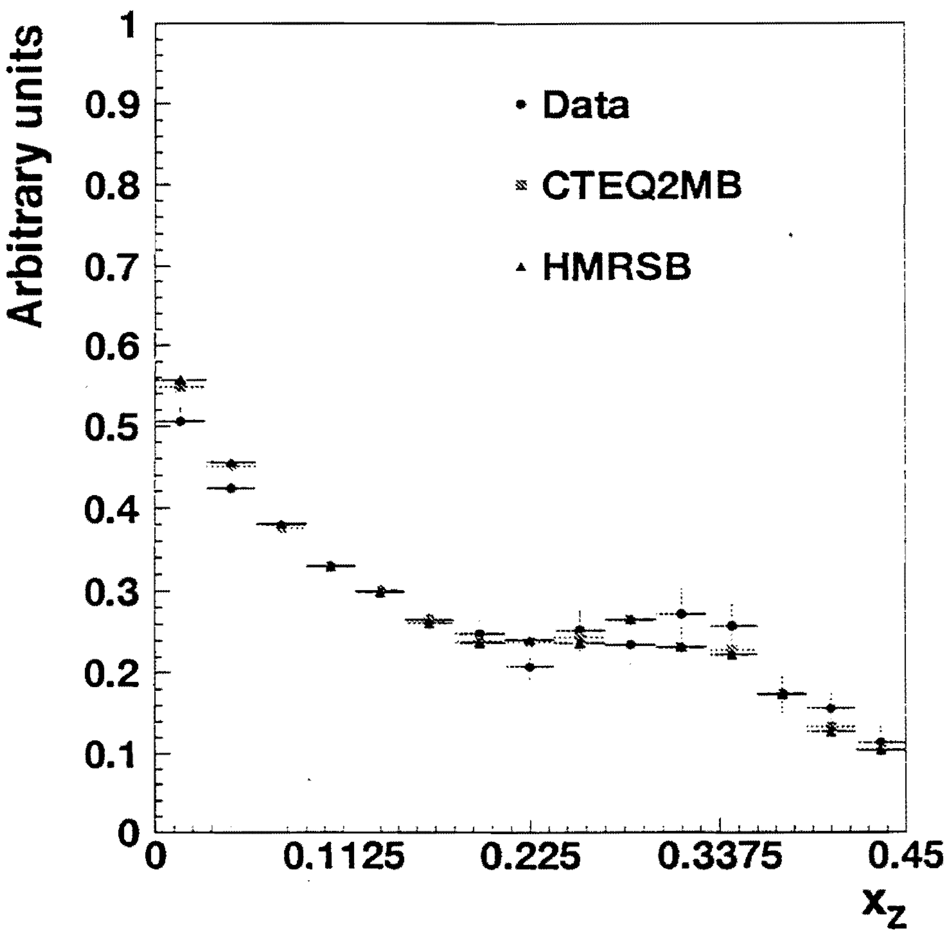

Figure 9.2: x_Z data distribution compared to CTEQ2M and HMRSB pdfs.

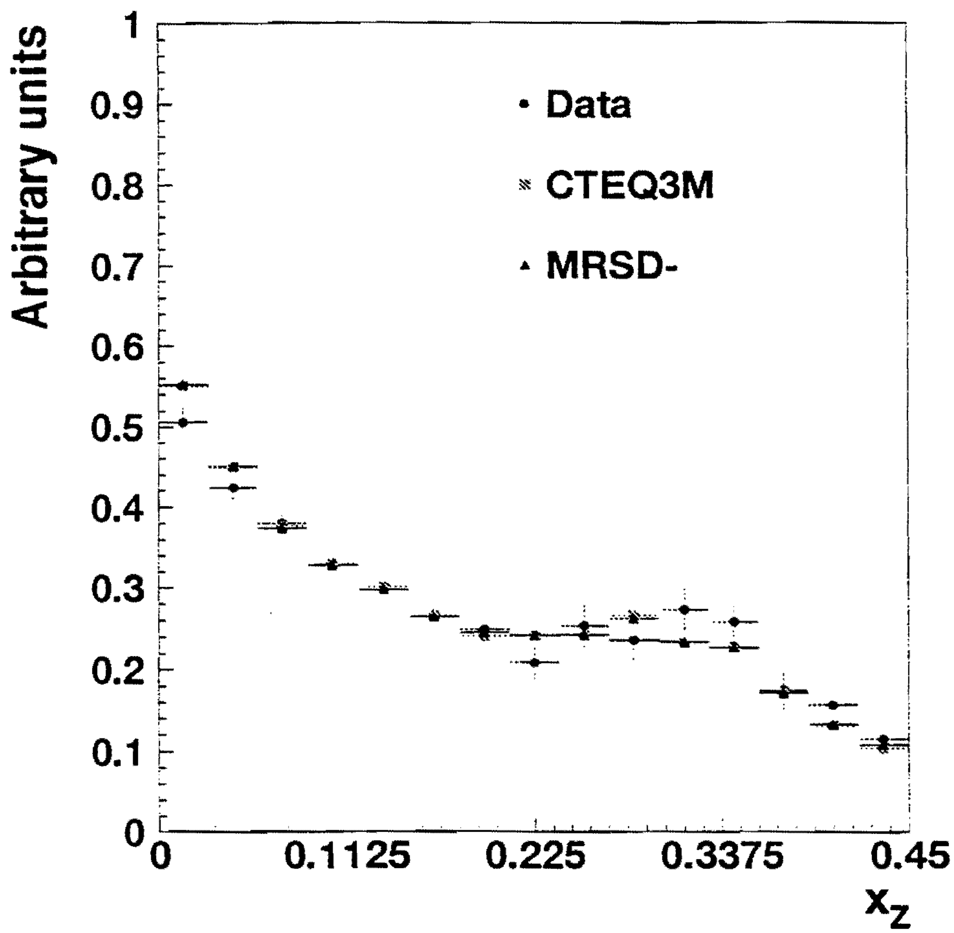

Figure 9.3: x_Z data distribution compared to CTEQ3M and MRSD- pdfs.

Figure 9.4 shows the x_1 data distribution compared to Monte Carlo x_1 distributions generated using CTEQ2M and HMRSB pdfs. Figure 9.5 shows data compared with CTEQ3M and MRSD-.

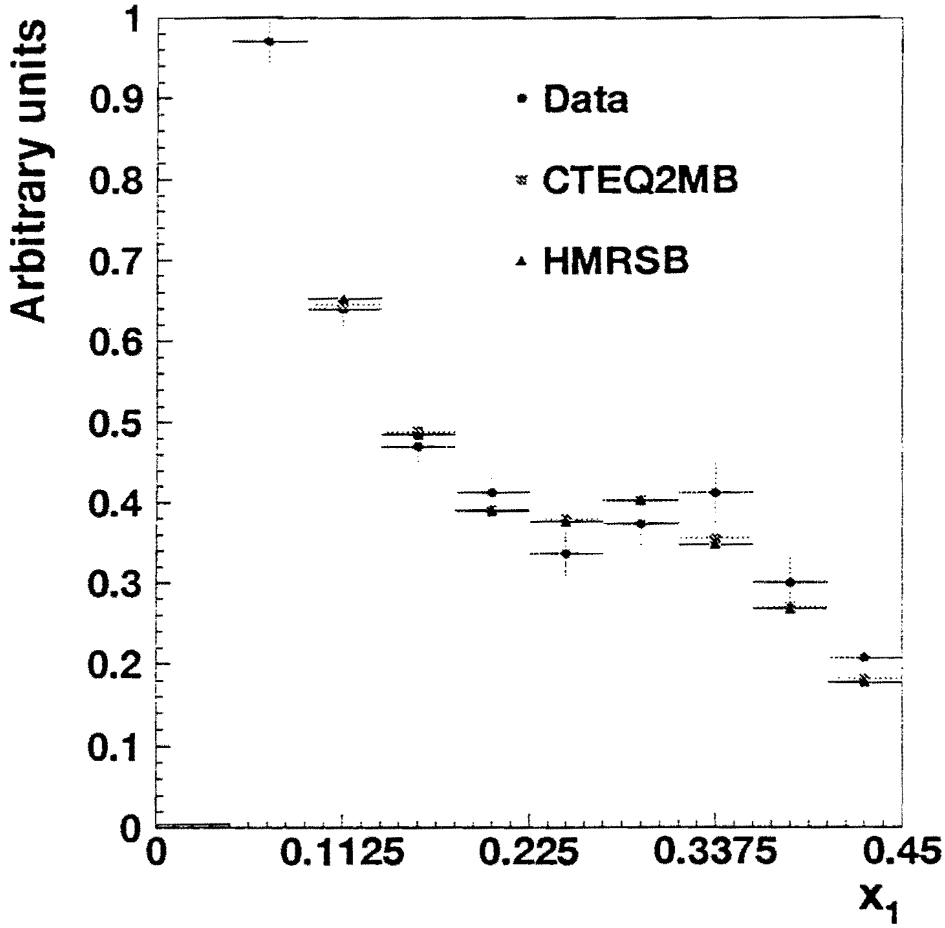

Figure 9.4: x_1 data distribution compared to CTEQ2M and HMRSB pdfs.

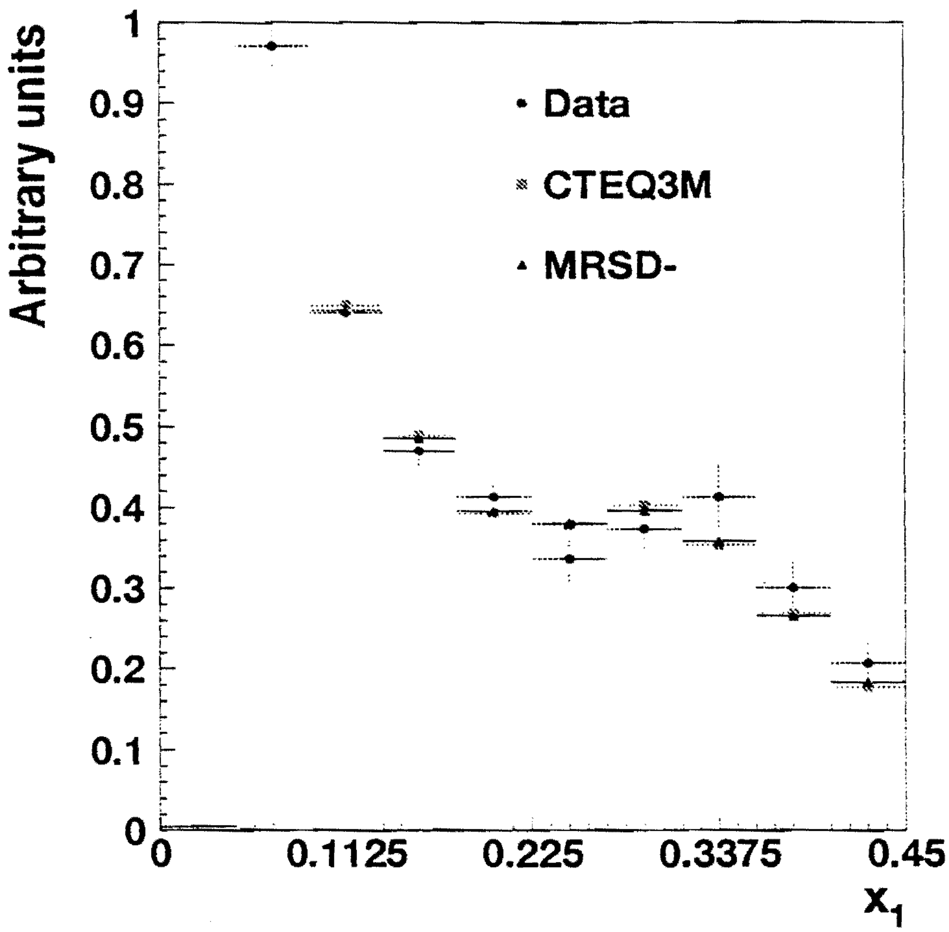

Figure 9.5: x_1 data distribution compared to CTEQ3M and MRSD- pdfs.

Figure 9.6 shows the x_2 data distribution compared to Monte Carlo x_2 distributions generated using CTEQ2M and HMRSB pdfs. Figure 9.7 shows data compared with CTEQ3M and MRSD-.

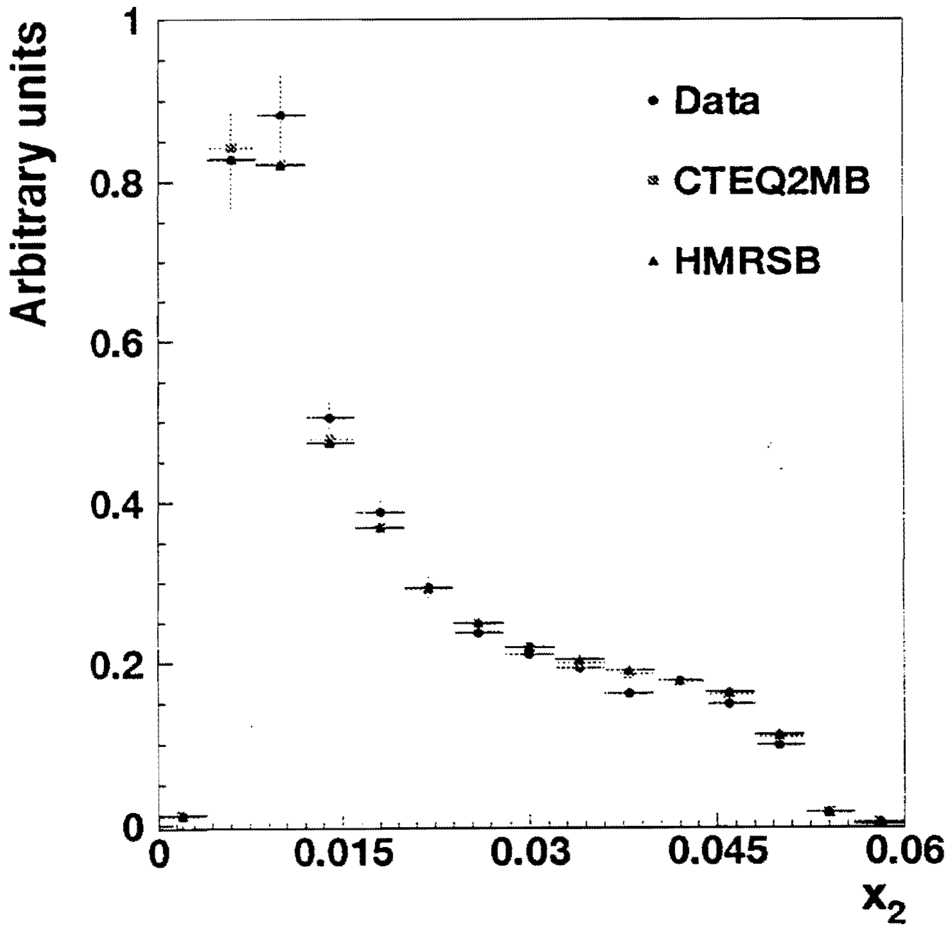

Figure 9.6: x_2 data distribution compared to CTEQ2M and HMRSB pdfs.

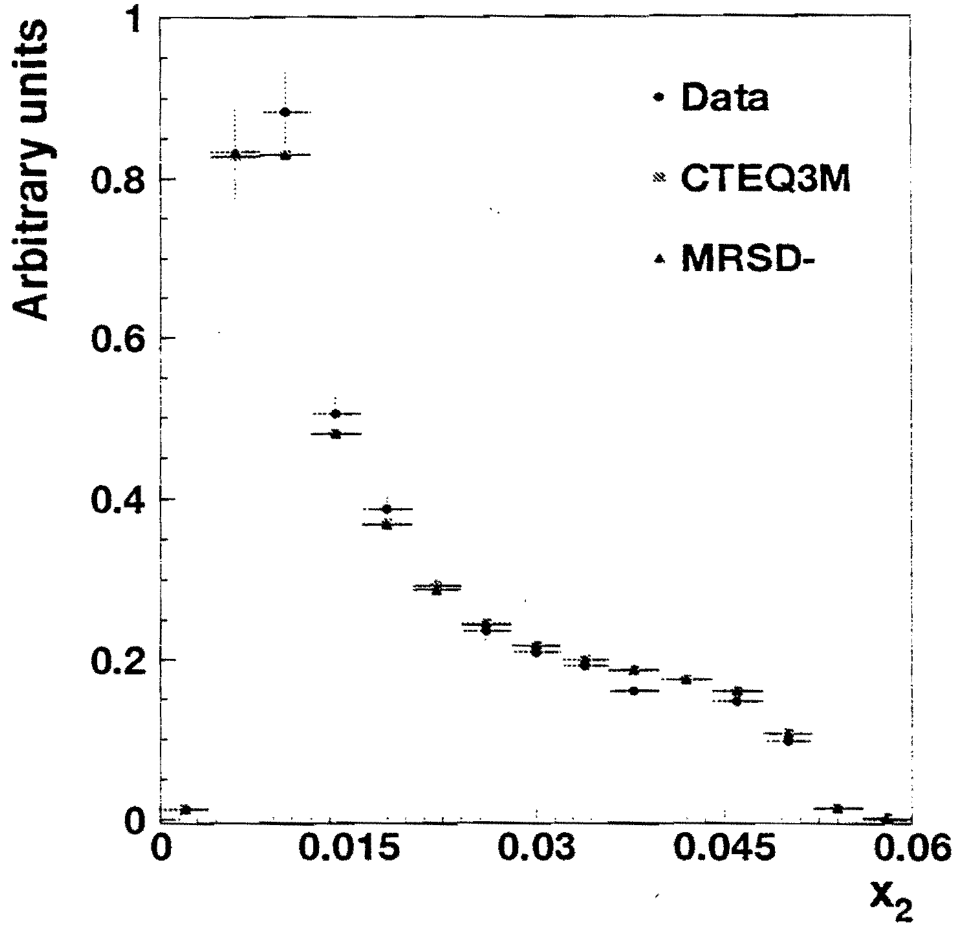

Figure 9.7: x_2 data distribution compared to CTEQ3M and MRSD- pdfs.

Bibliography

[1] C. Albajar, *et al.* Z. Phys **C44**:15-61, (1989).

[2] P. de Barbaro, "Tests of proton structure functions using leptons at CDF and DØ: *W* charge asymmetry and Drell Yan production" in *Proceedings of the 10th Topical Workshop on Proton-Antiproton Collider Physics*, Batavia, Illinois May 1995.

[3] S. Glashow, Nucl. Phys. **22**:579. (1961).

[4] A. Salam, *Elementary Particle Physics*, N. Svartholm ed., 367-375 (1968).

[5] S. Weinberg, Phys. Rev. Lett. **19**:1264-1266. (1967).

[6] F. Halzen and A. D. Martin *Quarks & Leptons: An introductory course in modern particle physics* John Wiley & sons. 1984.

[7] V. Barger and R. Phillips *Collider Physics, updated edition* Addison-Wesley. 1996.

[8] L. Montanet, Phys. Rev. **D50**:1173-1823. (1994).

[9] S. Abachi *et al.* Phys.Rev.Lett. **79**:1197-1202. (1997).

[10] M. Demarteau, J. Sculli and K. Streets DØ Note #2929. April 23, 1996. (Unpublished).

[11] P. M. Grudberg. *Measurement of the W and Z boson production cross sections in $p\bar{p}$ collisions at $\sqrt{s}$ = 1.8 TeV*, Ph. D. Thesis, University of California at Berkeley, Berkeley California, (1997). Unpublished.

[12] G. Arnison, *et al. Phys. Lett.* **B126**:398-410. (1983).

[13] H.L. Lai, *et al. Phys. Rev.* **D51**: 4763-4782. (1995).

[14] D. E. Soper, *Parton distribution functions* Talk at Lattice 96 Conference, St. Louis, June 1996.

[15] This plot was made in mid september 1997 using the utility by D. Soper and P. Anandam *A potpourri of partons* `http://zebu.uoregon.edu/~parton/`

[16] A. D. Martin, R. G. Roberts and W. J. Stirling, *Phys. Lett.* **B354**:155. (1995)

[17] M. Glück, E. Reya and A. Vogt, *Z. Phys.* **C67**:444. (1995).

[18] S. Feher, DØ Note #2563, 1995. (Unpublished).

[19] Joey Thompson "Introduction to colliding beams at Fermilab" FERMILAB-TM-1909. October 1994.

[20] Leon M. Lederman "The Tevatron" *Scientific American.* March 1991. pp 48.

[21] S. Abachi, *et al. Nucl. Instr. and Meth. in Phys. Res.* **A338**:185-253. (1994).

[22] A. R. Clark *et al. Nucl. Instr. and Meth. in Phys. Res.* **A279**:243-248. (1989).

[23] Joey Thompson. Private communication.

[24] DØ software documentation. DØ collaboration (edited by Geoff Manning). July 10, 1995. (Unpublished)
Taken from:
`http://www-d0.fnal.gov/newd0/d0atwork/computing/offline_document.ps`

[25] Steven Glenn, *A Search for Self-Interactions of Neutral Electroweak Gauge Bosons*, Ph. D. Thesis, University of California, Davis California, (1996). Unpublished.

[26] Jamal Tarazi, *A Measurement of the Cross Section Ratio of the W and Z Electronic Decays and the Total Width of the W Gauge Boson in Proton-Antiproton Collisions at $\sqrt{s}$ = 1.8 TeV*, Ph. D. Thesis, University of California, Irvine California, (1997). Unpublished.

[27] Details on the actual process can be found in the `WZ` folder of DØNEWS. Messages #389 and #521 on `FNALDO`.

[28] Casey D., Joffe-Minor T., Tarazi J. *QCD/WZ Ntuples*. DØ note 3124. November 1996.

[29] NYU Monte Carlo developed by Q. Zhu, J. Sculli and M. Demarteau.

[30] F. Paige and Serban D. Protopopescu, BNL Report No. BNL38034, 1986 (unpublished), release v 6.49.

[31] E. M. Flattum *A measurement of the W boson mass in $p\bar{p}$ collisions at $\sqrt{s}$ = 1.8 TeV.* Ph. D. Thesis, Michigan State University. East Lansing Michigan. (1996). Unpublished.

[32] I. M. Adam. *A measurement of the W boson mass with the DØ detector using the electron E_T spectrum.* Ph. D. Thesis. Columbia University, New York N. Y. (1997) Unpublished

[33] G. Marchesini *et al.* *Comput. Phys. Commun.* **67**,465 (1992), release 5.7.

[34] H. Plotow-Besch, CERN-PPE W5051 (1995).

[35] W. G. D. Dharmaratna. *Reconstruction of the calorimeter response-test beam load 2.* DØ note 1731. May 10, 1993. (Unpublished).

[36] LEP Electroweak Working Group, CERN-PPE/96-193.

[37] U. Heintz, *Reconstruction of π^0 decays in the DØ detector.* DØ note 2209. July 23, 1994. (Unpublished).

[38] U. Heintz, *A measurement of the calorimeter response using π^0 decays.* DØ note 2268. August 27, 1994. (Unpublished).

[39] I. Adam, *et al.* *Observation of $J/\psi \rightarrow ee$ decays at DØ and calibration of the central calorimeter electromagnetic scale.* DØ note 2298. October 3, 1994. (Unpublished).

[40] U. Heintz and I. M. Adam. *Calibration of the CC-EM energy scale.* DØ note 2739. February 6, 1995. (Unpublished).

[41] D. P. Casey *Measurement of the $d\sigma/dp_T$ for the Z boson in Run 1B* Note for the APS presentation. April 1997 (unpublished).

[42] HBOOK Reference Manual V 4.22. Application Software Group. CERN Geneva, Switzerland. 1995.

[43] CERNLIB CERN program library. Short writeups. May 1995.

[44] T. Sjöstrand, *Computer Phys. Comm.* **39**:347 (1986); T. Sjöstrand, CERN-TH.7112/93. December 1993, version 5.7.

[45] J. Tarazi and J. Thompson. Measurement of the $W \rightarrow e\nu$ and $Z \rightarrow ee$ inclusive cross sections using Run Ib/Ic Data. DØ note xxxx.

[46] Jie Yang *Measurement of the Width of the W Boson in Proton-Antiproton Collisions at $\sqrt{s} = 1.8$ TeV* Ph. D. Thesis, New York University, New York. (1995) (unpublished).

[47] F. Carminati *et al.* "*GEANT Users guide*", CERN Program Library, (1991) (Unpublished).

[48] G. A. Ladinsky and C.P. Yuan, *Phys. Rev.* **D50** 4239 (1994).

[49] F. A. Berends and R. Kleiss, *Z. Phys.* **C27** 365 (1985).

[50] M. Demarteau, J. Sculli and K. Streets DØ Note #2921. April 19, 1996. (Unpublished).

[51] L. Lyons, *Statistics for nuclear and particle physicists*. Cambridge University Press, New York (1986).

[52] B. P. Roe, *Probability and statistics in experimental physics*. Springer Verlag, New York (1992).

[53] M. Narain and U. Heintz, "A Study of Electron ID Efficiencies Using $Z \to e^+e^-$ Decays," DØ Note 1814. (1993). Unpublished.

[54] P. Grudberg, "Cross Section Measurements of W and W Bosons to Electrons at DØ: Event Selection and Efficiency Studies," DØ Note 2316. (1994). Unpublished.

[55] J. Tarazi. Private communication.